

# **Interstellar Pickup Ions at 1 AU with STEREO/PLASTIC**

Dissertation zur Erlangung des Doktorgrades  
der Mathematisch-Naturwissenschaftlichen-Fakultät  
der Christian-Albrechts-Universität zu Kiel

vorgelegt von  
Christian Drews

May 24, 2013



Referent/in: Prof. Dr. Robert F. Wimmer-Schweingruber

Korreferent/in: Prof. Dr. Sebastian Wolf

Tag der mündlichen Prüfung: 15.5.2013

Zum Druck genehmigt: 15.5.2013

## Abstract

In this thesis, interstellar pickup ions at 1 astronomical unit are analysed with the PLASMA and SupraThermal Ion Composition instrument (PLASTIC) on board the Solar Terrestrial Relations Observatory (STEREO). Interstellar pickup ions originate from the neutral component of the Local InterStellar Medium (LISM), which enters the heliosphere with a velocity of  $\sim 25$  km/s as a result of its relative motion with respect to our Sun. This neutral wind is gradually ionized by charge exchange with the solar wind, by solar ultraviolet radiation, or more rarely, by electron impact and thus acts as the seed population for interstellar pickup ions. The freshly created ions are 'picked up' by the interplanetary magnetic field that is frozen into the solar wind and rapidly acquire speeds equaling the solar wind speed in a solar wind frame of reference. More importantly, these pickup ions carry information on the LISM and provide an excellent opportunity to study the LISM in-situ.

In this work three aspects of interstellar pickup ions are explored. The first aspect covers the longitudinal distribution of interstellar pickup ions at 1 astronomical unit for which we have developed an analysis that counteracts the prevalent modulation of pickup ion fluxes by the solar wind. This allowed us to derive unbiased time series of pickup ions at 1 astronomical unit and to reveal for the first time the formation of the neon focusing cone, a region of enhanced  $\text{Ne}^+$  density on the downwind side of the Sun.

In our second study, we have investigated the source of interstellar pickup ions - the local interstellar medium. We have used results from our first study, i.e. our findings of the neon focusing cone, and combined them with a statistical approach to derive the inflow direction of interstellar matter  $\lambda_{\text{LISM}}$  as seen from an observer inside the heliosphere. Our value for  $\lambda_{\text{LISM}} = 78.4^\circ \pm 1.3^\circ$ , which was deduced from  $\text{He}^+$ ,  $\text{O}^+$ , and  $\text{Ne}^+$  measurements with PLASTIC, is barely consistent with the previous value of  $\lambda_{\text{LISM}} = 74.99^\circ \pm 0.55^\circ$  that was obtained from neutral as well as pickup helium measurements with various instruments in 2004. We further demonstrate the importance of the prevalent modulation of pickup ion fluxes with the solar wind speed and density for any parameter study of the LISM and argue that the observed deviation between the two values of  $\lambda_{\text{LISM}}$  is likely due to the capability of our analysis to properly consider the aforementioned modulation. As a by-product of our study, we also observed the interstellar crescent, a region of enhanced pickup ion density on the upwind side of the Sun, for the first time.

Finally, our last study addresses the kinetic properties of interstellar pickup ions directly after their ionization. We found that velocity distribution functions of interstellar pickup ions show distinct anisotropies that follow the orientation of the Interplanetary Magnetic Field (IMF). It is commonly believed that interstellar pickup ion velocity distribution functions are very rapidly isotropized and thus assumed to be isotropic: This means that they should be unaffected by the prevalent magnetic field orientation. However, we find clear anisotropies, which question many of the existing pickup ion models. These models misleadingly attribute independent observations from several instruments of a reduced flux and change in spectral slope of interstellar pickup ion spectra during quasi-radial IMF orientations to ineffective scattering across  $90^\circ$  pitch-angle. Here we show, that these observations are instead likely to be caused by the anisotropic pickup ion component that escapes detection during frequent configurations of the IMF.

## Zusammenfassung

In dieser Arbeit werden Pickup-Ionen bei einer astronomischen Einheit mit dem Plasma and Suprathermal Ion Composition Instrument (PLASTIC) an Bord des Solar Terrestrial Relations Observatory (STEREO) untersucht. Interstellare Pickup-Ionen entstammen der neutralen Komponente des interstellaren Mediums, welches auf Grund seiner Relativbewegung zu unserer Sonne die Heliosphäre mit einer Geschwindigkeit von 25 km/s durchfließt. Dieser neutrale Wind wird dabei sukzessive durch Ladungsaustausch mit dem Sonnenwind, ultra-violetter Strahlung der Sonne oder aber Elektronenstossionisation ionisiert und stellt somit die Ursprungspopulation der interstellaren Pickup-Ionen dar. Die dabei entstandenen Ionen werden vom dem im Sonnenwind eingefrorenen Magnetfeld mitgetragen und erreichen dabei Geschwindigkeiten von bis zu einer Sonnenwindgeschwindigkeit im Bezugssystem des Sonnenwindes. Entscheidend für diese Arbeit ist zudem, dass trotz des Ionisationsprozesses der Pickup-Ionen einige der Charakteristiken des LISMs erhalten bleiben und somit eine hervorragende Möglichkeit bieten das LISM eingehender zu studieren.

Im Verlauf dieser Arbeit werden drei Aspekte interstellarer Pickup-Ionen untersucht. Der erste Aspekt behandelt ihre longitudinale Verteilung bei einer astronomischen Einheit entfernt von der Sonne. Hierfür wurde eine Analyse entwickelt, welche der vorherrschenden Modulation der Pickup-Ionen-Flüsse durch den Sonnenwind entgegenwirkt und es somit erlaubt unverfälschte Zeitreihen von interstellaren Pickup-Ionen bei einer astronomischen Einheit zu untersuchen. Im Zuge dieser Untersuchung wurde anhand eines Dichte-Anstieges von  $\text{Ne}^+$  auf der dem interstellaren Wind abgewandten Seite der Sonne erstmals die Fokussierung von interstellaren Neon-Ionen beobachtet - der sogenannte Neon focusing cone.

Unsere zweite Studie befasst sich mit der Quelle der interstellaren Pickup-Ionen: dem interstellaren Medium. Hierfür wurde unter Hinzunahme der Resultate unserer ersten Studie und eines speziell entwickelten statistischen Ansatzes die Einflussrichtung des interstellaren Medium  $\lambda_{\text{LISM}}$  aus Sicht eines Beobachters innerhalb der Heliosphäre bestimmt. Unser Wert für  $\lambda_{\text{LISM}} = 78.4^\circ \pm 1.3^\circ$ , welcher durch Messungen von  $\text{He}^+$ ,  $\text{O}^+$  und  $\text{Ne}^+$  mit PLASTIC bestimmt wurde, steht dabei in Kontrast zu Resultaten anderer Studien aus dem Jahr 2004 unter Verwendung verschiedener Instrumente, die den Wert im Mittel mit  $\lambda_{\text{LISM}} = 74.99^\circ \pm 0.55^\circ$  angeben. Wir zeigen, dass die Diskrepanz beider Ergebnisse in der vorherrschenden Modulation der Pickup-Ionen-Flüsse durch die Sonnenwind-Geschwindigkeit und -Dichte begründet ist und mit unserer Analyse entsprechend berücksichtigt werden kann. Unsere Studie ermöglichte darüber hinaus erstmals die Beobachtung des interstellaren "Crescent", welcher in Analogie zum focusing cone einer Dichteanreicherung von interstellaren Pickup-Ionen auf der dem interstellaren Wind zugewandten Seite der Sonne entspricht.

Im Verlauf unserer dritten Studie untersuchen wir die kinetischen Eigenschaften interstellarer Pickup-Ionen direkt nach ihrer Ionisation. Dabei haben unsere Beobachtungen gezeigt, dass die Geschwindigkeitsverteilung interstellarer Pickup-Ionen entgegen den allgemeinen Erwartungen ausgeprägte Anisotropien aufweist, die der Ausrichtung des Interplanetaren Magnetfeldes (IMF) folgen. Unsere Beobachtung stellen damit viele der gängigen Pickup-Ionen-Modelle in Frage. Diese Modelle schreiben eine Reihe von Phänomenen, wie z.B. der Beobachtung eines reduzierter Fluss und Änderung der spektralen Form während radialer IMF-Konfigurationen, der ineffiziente Streuung interstellarer Pickup-Ionen über

einen Pitch-Winkel von  $90^\circ$  zu. Im Zuge unserer Studie zeigen wir, dass die eben genannten Beobachtungen vielmehr in der anisotropen Komponente der Geschwindigkeitsverteilung interstellarer Pickup-Ionen begründet sind, welche bei radialer Ausrichtung des IMF mit den meisten Instrumenten nicht gemessen werden kann.

# Contents

<b>1. Introduction</b>	<b>3</b>
1.1. The Interstellar Medium . . . . .	4
1.2. Interstellar Pickup Ions . . . . .	4
1.3. Inner-Source Pickup Ions . . . . .	11
1.4. Structure of this Work . . . . .	13
<b>2. Instrumentation</b>	<b>15</b>
2.1. STEREO . . . . .	15
2.2. PLASTIC . . . . .	18
2.2.1. Entrance System / Energy Analyzer . . . . .	18
2.2.2. Time-of-Flight / Energy Chamber . . . . .	21
2.2.3. Principle of Work . . . . .	22
2.3. Data Acquisition . . . . .	26
2.3.1. Pulse Height Analysis Data . . . . .	26
<b>3. Observations of the Neon Focusing Cone</b>	<b>35</b>
3.1. Introduction . . . . .	35
3.2. Publication . . . . .	36
3.3. Supplementary Remarks . . . . .	46
3.3.1. Performance of the Poisson Analysis . . . . .	46
<b>4. Inflow Direction of the Interstellar Medium</b>	<b>49</b>
4.1. Introduction . . . . .	49
4.2. Publication . . . . .	50
4.3. Supplementary Remarks . . . . .	63
4.3.1. Performance of the Proposed Analysis . . . . .	63
4.3.2. Systematic Influences . . . . .	66
<b>5. Pitch-Angle Distributions of Pickup Ions</b>	<b>73</b>
5.1. Introduction . . . . .	73
5.2. Publication . . . . .	74
5.3. Supplementary Remarks . . . . .	81
5.3.1. Virtual Detector . . . . .	81
<b>6. Conclusions &amp; Outlook</b>	<b>85</b>
<b>A. Systematic Influences by Efficiency Decay</b>	<b>89</b>





# 1. Introduction

The Solar System is surrounded by a thin, warm, and partially ionized gas called the Local InterStellar Medium (LISM), which is believed to originate from the star forming region "Scorpius Centaurus" that lies at a distance of  $\sim 400$  light years from our Sun. The interstellar wind moves with a velocity of  $\sim 25$  km/s with respect to the Solar System and by that interacts with the solar wind to form the outer boundary of the heliosphere, the so-called heliopause. Comparing parameters of the very local interstellar matter such as its isotope ratios and composition to solar values, which likely reflect the ISM properties 4.6 Billion years ago, helps us to understand how our universe has evolved and addresses the important question how our Solar System was formed.

With almost all of the gaseous material inside our heliosphere coming from the neutral component of the LISM, it not only defines the boundaries of the heliosphere, but also acts as the main driver for several important extraterrestrial phenomena, such as anomalous cosmic rays, pickup ions, and energetic neutral atoms. Studying the LISM is therefore not only a matter of "looking into the past", but is also important to understand the dynamic behaviour of the heliosphere. Aside from a direct measurement of interstellar neutral atoms (that tend to easily escape detection), interstellar pickup ions provide the most direct approach to measure in-situ parameters of the LISM. However, the prevalent modulation of interstellar pickup ions by the solar wind, the regularly changing conditions inside the heliosphere with the solar cycle, and the ionization process that is accompanied by a change of the kinetic behaviour of the former interstellar neutrals, requires a broad understanding of pickup ions in general in order to approach the complex task of studying the LISM with in-situ measurements in the inner heliosphere.

Therefore three important aspects of interstellar pickup ions are explored in this work. One aspect highlights the ionization process of interstellar neutrals and thus describes the kinetic properties of interstellar pickup ions on their way through the heliosphere. This study is especially important to properly model interstellar pickup ions inside the heliosphere and thus is crucial for any model based parameter study of the interstellar medium. Another aspect covers the global distribution of pickup ions inside the heliosphere at 1 Astronomical Unit (AU). Here we present the first observations of the neon focusing cone and interstellar crescent, two characteristic signatures that can be used to infer the temperature of interstellar neutral helium, oxygen, and neon. The last aspect examines the source of interstellar pickup ions itself, the LISM. Using a sophisticated statistical approach, we directly infer the inflow direction of the interstellar medium with respect to our Solar System and discuss the prevalent modulation of pickup ions by the solar wind.

The following subchapters on the interstellar medium (1.1), interstellar pickup ions (1.2), and inner-source pickup ions (1.3) provide the necessary theoretical background for this work. The thesis' structure is described at the end of this chapter.

## 1.1. The Interstellar Medium

The Local InterStellar Medium (LISM) that surrounds the Solar System is a warm ( $T = 7000$  K), thin ( $n = 0.3 \text{ cm}^{-3}$ ) and partially ionized gas cloud often referred to as the Local Interstellar Cloud (LIC) [Frisch *et al.*, 2011]. It lies at the edge of the so-called Local Bubble (LoB), which is a vast cavity in space with a diameter of almost 300 light years. Compared to the LIC it is extremely hot ( $T_{\text{LoB}} = 10^6$  K) and thin ( $n_{\text{LoB}} = 10^{-3} \text{ cm}^{-3}$ ), which is  $\sim 10^7$  times less dense than the best vacuum achieved on earth [Frisch, 2000]. Its origin is still an open question but is likely related to either a supernova explosion or a star forming region that has pushed aside the material inside the LoB. The LIC, which is only one of many interstellar clouds in our galactic neighbourhood, is believed to be produced by the outflow of the star forming region called Scorpius-Centaurus association that lies 400 light years away from the Sun. The material that emerges from this region shows a very similar composition to the solar wind. It consists of 90% hydrogen, 9.9% helium, and 0.1% heavier elements of which oxygen is the most abundant one. However, the interstellar medium shows a very different charge state distribution compared to the solar wind. While hydrogen, helium, nitrogen, and oxygen occur mainly as neutral atoms (78%, 61%, 72%, and 81% respectively), only a small fraction of carbon, neon, magnesium, silicon, and iron are in their neutral state inside the LISM ( $3 \cdot 10^{-2}\%$ , 20%, 0.2%,  $4 \cdot 10^{-3}\%$ , and  $7 \cdot 10^{-3}\%$  respectively) [Frisch *et al.*, 2011]. An illustration of our galactic environment can be found in Fig. 1.1.

The combined motion of the LISM and the Sun with respect to its neighbouring stars leads to what we call the interstellar wind, a persistent flow of interstellar material with a velocity of  $\sim 25$  km/s with respect to our Solar System [Fahr, 1968]. Despite being thin and relatively cool, the motion of the LISM combined with the supersonic solar wind flow defines the boundaries of the heliosphere. As the solar wind streams radially away from the Sun it must work against the surrounding interstellar plasma and is gradually decelerated to a point, where it reaches subsonic velocity. At this location a shock front forms, which is called the Termination Shock. In analogy, a shock front forms also where the LISM is decelerated to subsonic speed, which results in the formation of the so-called Bow Shock. The location at which the solar wind as well as the interstellar plasma comes to a complete stop, i.e. the location at which the solar wind ram pressure is equal to the interstellar plasma ram pressure, is called the Heliopause. The Heliopause lies at around 130 to 150 AU away from the Sun and defines the outermost edge of the heliosphere, e.g. [Prölss, 2004].

## 1.2. Interstellar Pickup Ions

While the ionized component of the LISM is deflected by the heliospheric magnetic field at the Heliopause, interstellar neutral atoms can pervade the heliosphere unimpeded as they are not affected by the interplanetary magnetic field. They can travel deep into the heliosphere before they are finally ionized by charge exchange with solar wind protons, or more likely, photoionization by solar ultraviolet radiation. Close to the Sun however, their abundance ratio not necessarily reflects the prevalent composition of the LISM. The different interstellar species have different First Ionization Potentials (FIP) (e.g. H: 13.6 eV, He: 24.6 eV, N: 14.5 eV, O: 13.6 eV) and are depleted on varying scales. Furthermore,

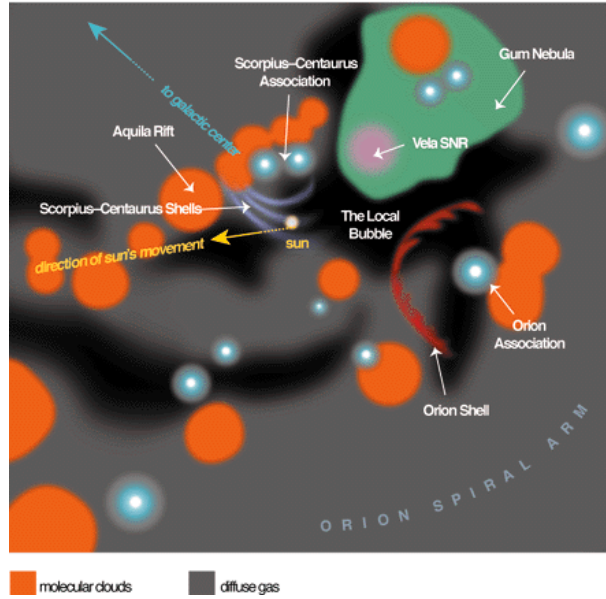


Figure 1.1.: Illustration of the galactic environment within 1500 light-years around the Sun. Our Solar System lies at the edge of the so-called local bubble, a cavity in space with a density of  $\sim 10^{-3} \text{ cm}^3$  and a temperature of  $\sim 10^6 \text{ K}$ . It is surrounded by the local interstellar cloud, which is believed to be part of the outflowing material from the Scorpius-Centaurus association, a star forming region that is roughly 400 light years away. The combined motion of the outflowing material from the Scorpius-Centaurus association and the motion of our Solar System with respect the nearby stars results in, what we call, the interstellar wind. The interstellar wind is a partially ionized gas that persistently streams towards the Solar System with a velocity of  $\sim 25 \text{ km/s}$ . Figure taken from <http://www.americanscientist.org/issues/pub/the-galactic-environment-of-the-un>

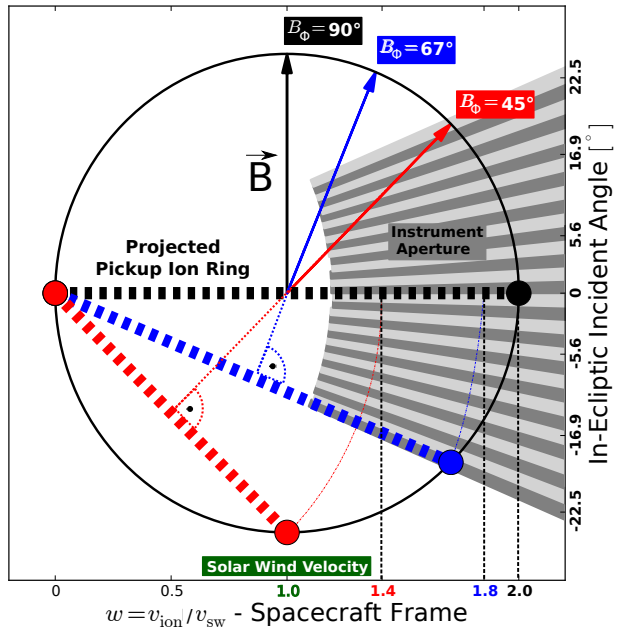
interstellar neutral H, O, and N are depleted in the so-called filtration region beyond the heliopause where they suffer loss from charge exchange with slowly moving interstellar and solar  $\text{H}^+$  [Kallenbach *et al.*, 2000]. As a result helium is the dominant interstellar species at 1 AU, although hydrogen is  $\sim 10$  times more abundant than helium in the LISM [Frisch *et al.*, 2011].

An in-situ measurement of the interstellar neutral component at 1 AU proves to be difficult as the slowly moving neutral particles tend to easily escape detection. A breakthrough in this department has recently been made with the Interstellar Boundary Explorer (IBEX) launched in 2010 [McComas *et al.*, 2009], which is an Earth-bound spacecraft specifically designed to sample the ENA as well as the interstellar neutral population inside the heliosphere. The interested reader may refer to e.g. Möbius *et al.* [2012] and Bochsler *et al.* [2012] for an overview on interstellar neutral studies with IBEX. Here we will focus on interstellar particles that have already been ionized by charge exchange with solar wind protons or solar ultraviolet radiation, so-called interstellar pickup ions.

As seen from an observer inside the Solar System, interstellar neutrals move along a defined axis, the so-called inflow axis of the LISM, through the heliosphere with an initial velocity of  $v_{\text{ISM}} \approx 25 \text{ km/s}$ . During their flight they can be ionized by charge exchange

Figure 1.2.

Illustration of pickup ions ring-beam distributions in phase space (the x-axis points in the direction of the moving solar wind at  $v_z = 0$  km/s, i.e. in the ecliptic plane). Using the simplification that  $v_{\text{ISM}} = 0$  km/s, freshly ionized interstellar pickup ions start to gyrate perpendicular to  $\vec{B}$  with a maximum velocity of twice the solar wind velocity. The resulting velocity distribution function is often referred to as ring-beam distribution (thick dashed lines) and can be described to be a result of a two dimensional cut at  $v_P = 0$  km/s perpendicular to  $\vec{B}$  through a spherical shell (black outer circle) with a radius of  $r = v_{\text{SW}}$  (from *Drews et al.* [2013]).



and photo ionization - the probability for both processes scale with  $r_S^{-2}$ , whereas  $r_S$  is the distance from the Sun. Once an interstellar neutral atom is ionized, it is susceptible to the electro-magnetic forces of the solar wind. The former neutral starts to gyrate perpendicular to the embedded magnetic field line and quickly reaches a guiding center velocity of  $v_{\text{sw}}$  from whereon it is bound to the fast moving solar wind package that streams radially away from the Sun. The initial velocity of the pickup ion directly after the pickup process is determined by the relative velocity of the former interstellar neutral atom with respect to the solar wind and the orientation of the prevalent magnetic field [*Möbius et al.*, 1998]. During a radial IMF configuration the gyro motion velocity is zero and the velocity of the pickup ion is also zero. During a perpendicular IMF orientation the pickup ions starts to gyrate with a velocity of  $v_{\text{sw}}$  around the magnetic field line. If one neglects the velocity of the interstellar neutral  $v_{\text{ISM}}$  during the pickup process, the guiding center velocity of the pickup ion during the initial part of the pickup process can be described as

$$v_P = \cos(B_\phi) \cos(B_\theta) v_{\text{sw}}. \quad (1.1)$$

Here  $B_\phi$  and  $B_\theta$  are the in-ecliptic and out-of-ecliptic magnetic field angles with respect to  $\vec{v}_{\text{sw}}$ . An illustration of the pickup ion injection can be found in Fig. 1.2. The velocity  $v_P$  of the pickup ion in a resting frame of reference can be as high as twice the solar wind speed due to the perpendicular motion with respect to  $\vec{B}$ . The strictly perpendicular gyro motion with respect to  $\vec{B}$  implies that pickup ion velocity distributions are, so-called, ring-beam distributions (thick dashed lines in Fig. 1.2), which causes the incident angle of pickup ions to be a function of  $B_\phi$  and  $B_\theta$  [*Saul and Isenberg*, 2007]. However, it is commonly believed that the originally anisotropic pickup ion velocity distribution function is transformed into an isotropic velocity distribution by wave-particle interaction with magnetic fluctuations inside the solar wind. The pitch-angle diffusion is believed to happen on timescales of  $\sim 10$  to  $\sim 100$  hours [*Saul*, 2004b].

Theoretical work by *Vasyliunas and Siscoe* [1976], who originally proposed the idea of isotropic pickup ion velocity distributions, led to the, so-called, "cold" model of interstellar pickup ions, which is an analytic expression for the expected pickup ion flux anywhere inside the heliosphere. The model is called "cold" because it assumes that the velocity of the LISM is not broadened by the temperature of the LISM, which for many application can be a justified simplification (as discussed in chapter 4.2). The work by *Vasyliunas and Siscoe* [1976] is based on an expression for the density  $n(r, \phi)$  of interstellar neutrals inside the heliosphere that was originally described by *Fahr* [1969], Finding the density of interstellar neutrals  $n(r, \phi)$  is due to the symmetry of the inflowing interstellar material with respect to the LISM axis a two dimensional problem and can be expressed with two impact parameter  $b_1$  and  $b_2$  [*Vasyliunas and Siscoe*, 1976].

$$n(r, \phi) = n_\infty \frac{1}{\sin(\phi)} \left[ \frac{\delta b_1}{\delta r} \exp\left(-\frac{\lambda\phi}{b_1}\right) + \frac{\delta b_2}{\delta r} \exp\left(-\frac{\lambda(2\pi - \phi)}{b_2}\right) \right]. \quad (1.2)$$

Here  $n_\infty$  is the interstellar neutral density of a given species in the LISM.  $\lambda = r_0^2/v_\infty\tau$  is a factor that accounts for the gradual ionization of interstellar neutrals during their flight through the heliosphere, whereas  $\tau$  is the ionization time at a characteristic distance from the Sun,  $r_0$ , and  $v_\infty$  is the speed of interstellar neutrals at infinity. Furthermore,  $b_1$  and  $b_2$  define the two possible trajectories of an interstellar neutral atom through a point P at a distance  $r$  from the Sun and ecliptic longitude  $\phi$ . The two impact parameters are defined as

$$b_{1,2} = \left[ \left( \frac{1}{2} r \sin(\phi) \right)^2 + (1 - \mu) \frac{GM}{v_\infty^2} r (1 - \cos(\phi)) \right]^{\frac{1}{2}} \pm \frac{1}{2} r \sin(\phi), \quad (1.3)$$

where  $G$  is the gravitational constant and  $M$  is the mass of the Sun.  $\mu$  is a factor that accounts for the reduction of the gravitational force due to photon pressure (which is only relevant for interstellar hydrogen, where  $\mu \approx 1$ ). Because pickup ions stream radially away from the Sun, integrating the number of ionized interstellar neutrals from the Sun to a point  $r$  yields the flux of interstellar pickup ions as a function of the distance from the Sun  $r$  and ecliptic longitude  $\phi$  [*Vasyliunas and Siscoe*, 1976]

$$F(r, \phi) = n_\infty v_\infty \frac{\lambda^2}{r^2 \sin(\phi)} \left[ \phi \Psi\left(\frac{b_1}{\lambda\phi}\right) + (2\pi - \phi) \Psi\left(\frac{b_2}{\lambda(2\pi - \phi)}\right) \right], \quad (1.4)$$

where  $\Psi(x)$  is given by

$$\Psi(x) = x e^{-1/x} - \int_{1/x}^{\infty} t/e^{-t} dt. \quad (1.5)$$

As an example we show the flux of interstellar oxygen derived from Eq. 1.4 in Fig. 1.3 in arbitrary units. Necessary parameters for Eq. 1.4, such as the ionization rate at 1 AU, were taken from *Cummings and Stone* [2002]. The Sun's gravitational attraction causes interstellar neutrals to move along unbound Kepler orbits, which intersect on the downwind side of the Sun at an ecliptic longitude of  $\lambda_{\text{ISM}} + \pi$ , the inflow direction of the interstellar medium. In this region the density of interstellar neutrals is increased, which in turn results in a region of enhanced pickup ion density. This region is called

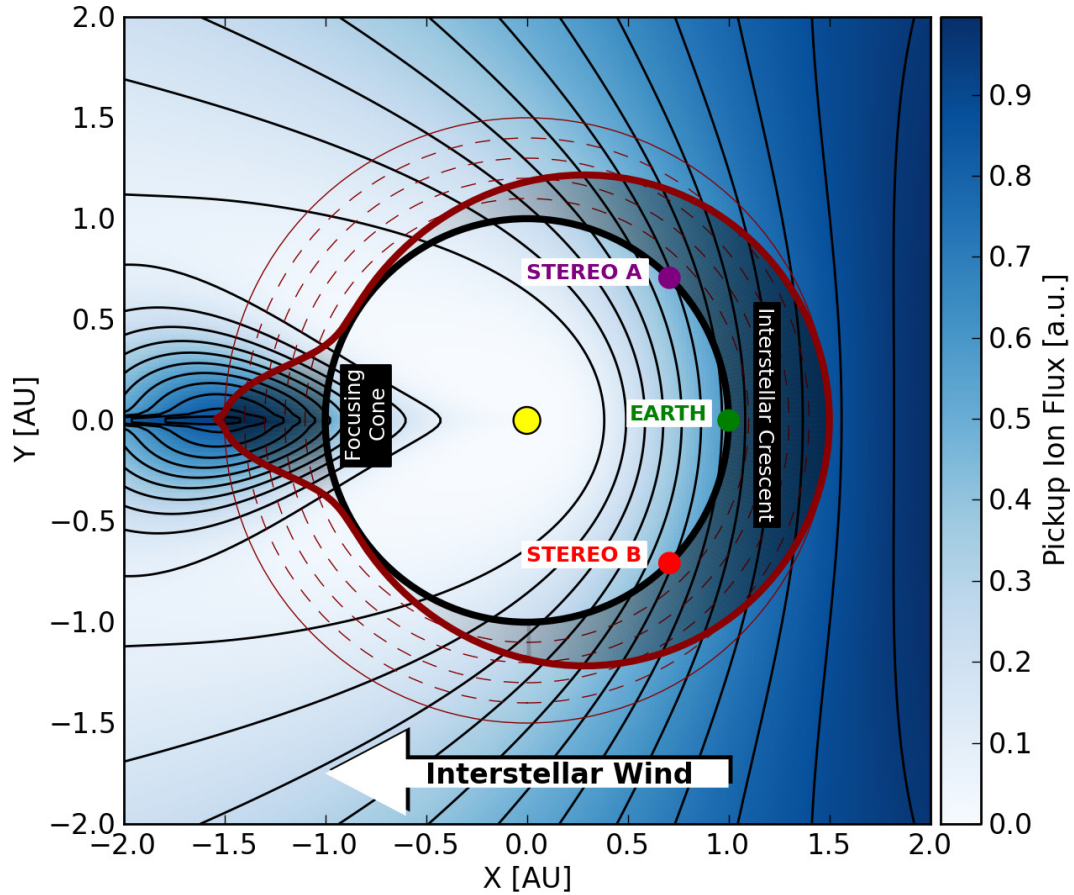
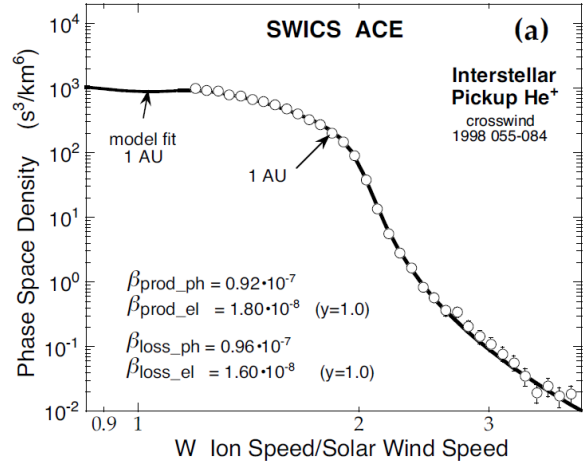


Figure 1.3.: An illustration of the pickup ion flux (color coded contour) born from interstellar neutrals in the vicinity of the Sun. In this view the interstellar neutrals enter the heliosphere from the right. Due to the influence of the Sun's gravitation the trajectories of the inflowing interstellar material are bent in a way that a region of enhanced interstellar neutral density forms on the downwind side of the Sun. This region, which also acts as a source for an increased pickup ion production, spans  $\sim 20^\circ$  and is called the focusing cone. It is most prominent for species that have a low probability for ionization by solar ultraviolet radiation or charge exchange with solar wind protons such as helium or neon. A second characteristic feature for interstellar neutrals is the formation of the so-called interstellar crescent - a region of enhanced density of interstellar material on the upwind side of the Sun that spans almost  $180^\circ$ . Its formation is a result of the enduring depletion of interstellar neutrals during their flight through heliosphere combined with a simple geometric effect. Neutrals at an ecliptic longitude  $\lambda \neq \lambda_{ISM}$  have been longer exposed to solar radiation and the solar wind if they are observed at a fixed distance from the Sun. As a result the observed neutral and pickup ion intensity shows a clear longitudinal dependency that resembles the form of a crescent if viewed in polar coordinates (thick red line). Both the focusing cone and interstellar crescent are believed to be aligned along the inflow axis of the interstellar medium.

the pickup ion focusing cone. The angular width of the focusing cone (with respect to the Sun) is determined by the temperature of the LISM, the location of the focusing cone is determined by the inflow direction of interstellar matter, and the intensity of the

Figure 1.4.

The phase space density of interstellar  $\text{He}^+$  is shown (white dots). The x-axis shows  $w = v_P/v_{\text{sw}}$ , i.e. the  $\text{He}^+$  velocity divided by the prevalent solar wind velocity. The data was collected with ACE/SWICS over a period of  $\sim 30$  days. The  $\text{He}^+$  velocity distribution function occupies a much wider range than  $w \approx 2$  due to adiabatic cooling ( $w < 2$ ) and acceleration processes in the heliosphere ( $w > 2$ ). The figure is taken from *Gloeckler et al.* [2004] and reproduced with permission (© ESO).



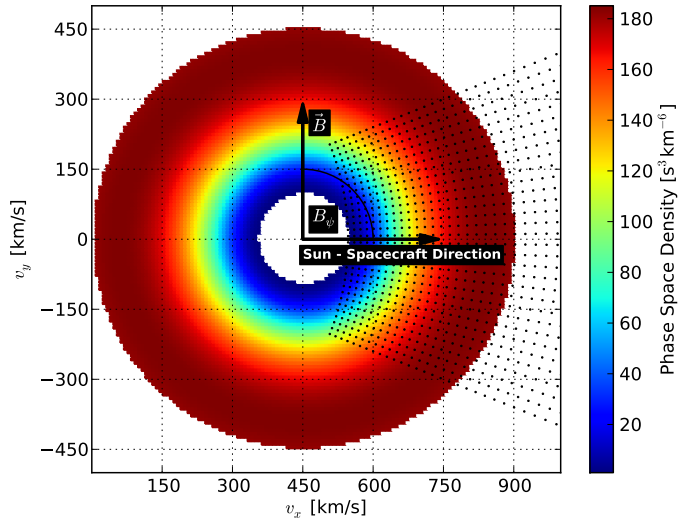
focusing cone is determined by the density and ionization rate of the interstellar neutral gas. On the upwind side of the Sun, the competing processes of ionization and pickup ion flux reduction that scales with  $r_S^{-2}$  due to the expanding solar wind and the line of sight integration of the ionized interstellar neutrals from the Sun to a point,  $P(r_S, \lambda)$ , results in a second characteristic feature of interstellar pickup ions, the so called interstellar crescent [*Drews et al.*, 2012]. The crescent spans a much wider angular range compared to the focusing cone, but can be similarly used to derive parameters of the LISM. We note, that the focusing cone can not be properly modeled by an interstellar "cold" model, which would instead produce a discontinuity with  $F \rightarrow \infty$  on the downwind side of the Sun. To illustrate the effect of gravitational focusing we used a normal distribution to create a focusing cone signature with a width as observed in chapter 4.2. However, due to oxygen's high ionization probability compared to helium, it is not expected to show such a strong focusing effect as illustrated in Fig. 1.3 [*Drews et al.*, 2012].

The pickup ion velocity distribution is highly non-thermal and considerably different from the velocity distribution function of solar wind ions. Although pickup ions can almost exclusively be distinguished from solar wind ions by their single charge state (apart from hydrogen, which is exclusively singly charged), their characteristic velocity distribution is a second important classification criteria. However, it is not as simple as to assume that  $v_P$  only depends on the IMF configuration ( $B_\phi, B_\theta$ ) and the prevalent solar wind speed  $v_{\text{sw}}$  as described by Eq. 1.1. As mentioned before, the pickup ion velocity distribution function is believed to quickly isotropize on time scales of 10 to 100 hours [*Saul*, 2004a], i.e. the initial pitch-angle of the pickup ion quickly turns into a random value between  $0 < \alpha < \pi$ . Consequently the initial pickup ion velocity  $v_P$  can also quickly reach a maximum speed of  $2 \cdot v_{\text{sw}}$  independent from the IMF orientation. In this picture, the pickup ions would also strictly move with a speed of  $v_P = 2 \cdot v_{\text{sw}}$  (if one neglects influences of the thermal speed of the solar wind and interstellar neutrals). However, measurements of the  $\text{He}^+$  distribution function as observed by, e.g., *Gloeckler et al.* [2004] (Fig. 1.4) show that this is definitely not the case. Instead the velocity distribution function is a highly non-thermal one with pickup ion velocities ranging between 0 and  $2 \cdot v_{\text{sw}}$  and beyond.

The reason for the broad range of observed pickup ions velocities lies in the fact that

Figure 1.5.

A two dimensional cut of the  $\text{He}^+$  phase space density in the  $(v_x, v_y)$  plane at  $v_z = 0$  km/s derived from *Vasyliunas and Siscoe* [1976]. Due to strong pitch angle scattering the  $\text{He}^+$  velocity distribution function was originally believed to be fully isotropic and independent of the prevalent IMF orientation (as is shown here). Because *Vasyliunas and Siscoe* [1976] did not consider particle acceleration processes or thermal speeds, the  $\text{He}^+$  velocity distribution has a sharp cut-off at  $w = 2$ . The grey dots represent the location of phase space covered by the Solar Wind Section of STEREO / PLASTIC.



pickup ions are bound to the expanding solar wind and undergo adiabatic cooling. As a result, their velocity in the solar wind frame decreases with increasing distance from the location of their ionization. Using the adiabatic law for a monoatomic gas

$$kT = V^{-\frac{2}{3}} \quad (1.6)$$

one can easily infer for pickup ions that

$$(E_P)^{\frac{3}{4}} r = \text{const.} \quad (1.7)$$

Here  $E_P$  is the kinetic energy of the pickup ion and  $r$  the radial distance from the Sun. This means the velocity of a pickup ion measured at a distance  $r_{\text{obs}}$  is determined by where it was ionized. A pickup ion with an energy of  $E_P = 0.5 \cdot E_{\text{sw}}$  at a distance of  $r_{\text{obs}}$  for instance has been created at a distance of  $r_{\text{sw}} = (1/2)^{\frac{3}{4}} r_{\text{obs}}$  from the Sun. Consequently, the flux of pickup ions with energies between  $E_P$  and  $E_{\text{sw}}$  through a shell with radius  $r$  must be the same as the line of sight integral of the ionization rate between  $(E_P/E_{\text{sw}})^{\frac{3}{4}}$  and  $r$

$$v_{\text{sw}} \int_E^{E_{\text{sw}}} dE' n(E') = \left(\frac{r_0}{r}\right)^2 \beta \int_{(E_P/E_{\text{sw}})^{\frac{3}{4}} r}^r dr' N(r', \phi). \quad (1.8)$$

Here  $n(E)$  is the number density of pickup ions,  $\beta$  is the ionization rate of interstellar neutrals (that scales with  $r^{-2}$ ), and  $N(r)$  is the neutral density given in Eq. 1.2. By transforming Eq. 1.8 into velocity space one obtains the expression for the velocity distribution function of interstellar pickup ions originally described by *Vasyliunas and Siscoe* [1976]

$$f(v) = \frac{3}{8\pi} \frac{r_0^2}{r v_{\text{sw}}^4} \beta \left(\frac{v}{v_{\text{sw}}}\right)^{-\frac{3}{2}} N\left(\left(\frac{v}{v_{\text{sw}}}\right)^{-\frac{3}{2}}, r, \phi\right). \quad (1.9)$$

In Fig. 1.5 a two dimensional cut through the  $v_z = 0$  km/s plane of the velocity distribution function derived from Eq. 1.9 is shown for interstellar  $\text{He}^+$  at 1 AU in the



upwind region of the Sun. In a frame of reference co-moving with the solar wind, it shows a sharp decrease, a so-called cut-off, at  $v_P = v_{\text{sw}}$  with a relatively smooth decay towards  $v_P = 0$  due to adiabatic cooling. The form of  $f(v)$  and especially the transition between  $v_P = 0$  and  $v_P = v_{\text{sw}}$  is also determined by the distance  $r_{\text{obs}}$  where the observation is made. Closer to the sun ( $r_{\text{obs}} \lesssim 5$  AU), the ratio of locally produced interstellar pickup with a velocity of  $v_P = v_{\text{sw}}$  to pickup ions that have already been cooled to  $v_P < v_{\text{sw}}$  is generally higher than further away from the Sun. For observation made at  $r_{\text{obs}} \gtrsim 5$  AU the ionization rate has already decreased significantly due to the reduced solar wind and photon flux, which means that the observed pickup ions flux primarily stems from already cooled particles that have been ionized further inside the heliosphere. As a result, the observed pickup ion  $w$ -spectra show a smoother decay towards  $v_P = 0$  (in a frame of reference co-moving with the solar wind). As will be discussed in chapter 4.2, the relation between the shape of  $f(v)$  and  $r_{\text{obs}}$  is further altered by the FIP of the respective pickup ion species.

In Fig. 1.6 one dimensional pickup ion  $w$ -spectra ( $w = v_P/v_{\text{sw}}$  with  $v_P$  being measured in a resting frame of reference) for  $\text{C}^+$ ,  $\text{O}^+$ ,  $\text{Ne}^+$ , and  $\text{Fe}^+$  are presented. These spectra were collected with the Solar Wind Section of STEREO/PLASTIC over a period of 4 consecutive years (refer to chapter 2.2 for details on STEREO/PLASTIC). To maintain comparability between different pickup ion species, different species have been collected during different solar wind conditions, as described in the caption of Fig. 1.6. Although this may affect the overall collected flux of pickup ions, i.e. the intensities of the presented spectra do not reflect the real abundance ratios of interstellar pickup ions, it assures that the form of the  $w$ -spectra for each species is comparable. One exception is the spectrum of  $\text{Fe}^+$ , which is so rare that it was not possible to reconstruct the  $\text{Fe}^+$  phase space density up to  $w = 2.5$ . Therefore, we will omit any discussion of the  $\text{Fe}^+$  spectrum in the following.

In Fig. 1.6 two important observations can be made:

- The  $\text{C}^+$ ,  $\text{O}^+$ , and  $\text{Ne}^+$  velocity distribution functions show a clear increase with decreasing  $w$ . This observation can not be explained by the interstellar pickup ion model proposed by *Vasyliunas and Siscoe [1976]*.
- $\text{C}^+$  shows a significantly different velocity spectrum than  $\text{O}^+$  and  $\text{Ne}^+$ , although the FIP of carbon (C: 11.3 eV) is only slightly lower than that of oxygen (O: 13.6 eV).

Both observations can be explained by introducing a second population of pickup ions, so-called inner-source pickup ions, which are believed to originate from a source close to the Sun. Inner-source pickup ions will be briefly explained in the following section of this chapter.

### 1.3. Inner-Source Pickup Ions

Inner-source pickup ions were originally discovered by *Geiss et al. [1995]* who measured  $\text{C}^+$  pickup ions at varying distances from the Sun with the SWICS instrument aboard Ulysses. Inside the LISM less than 0.1% of all carbon atoms exist in their neutral state [*Frisch et al., 2011*], so it was not expected to find a clear pickup  $\text{C}^+$  signature that was on the same order of magnitude as pickup  $\text{O}^+$  (of which  $\sim 81\%$  is in its neutral state inside the LISM). *Geiss et al. [1995]* therefore concluded that a second population of pickup

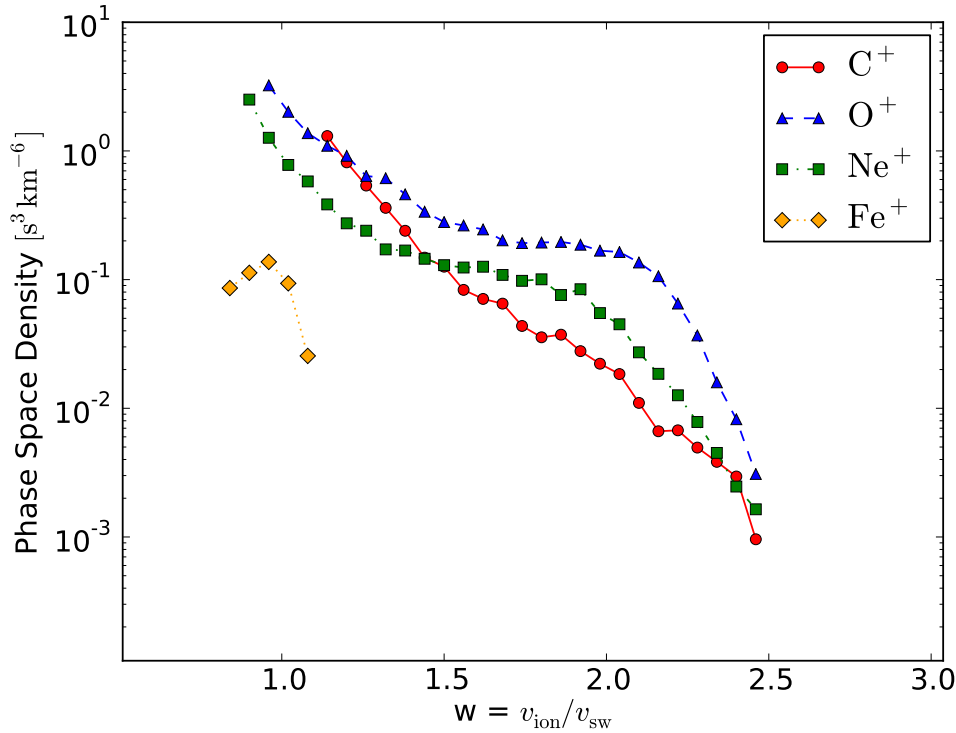


Figure 1.6.: Phase space density of  $C^+$  ( $290 \text{ km/s} < v_{sw} < 450 \text{ km/s}$ ),  $O^+$  ( $250 \text{ km/s} < v_{sw} < 390 \text{ km/s}$ ),  $Ne^+$  ( $220 \text{ km/s} < v_{sw} < 350 \text{ km/s}$ ), and  $Fe^+$  ( $393 \text{ km/s} < v_{sw} < 473 \text{ km/s}$ ) measured with the Solar Wind Section of PLASTIC between 2007 and 2011. Because  $Fe^+$  is extremely rare compared to  $C^+$ , PLASTIC did not observe any  $Fe^+$  events for  $w > 1.1$  and  $393 \text{ km/s} < v_{sw} < 473 \text{ km/s}$ .

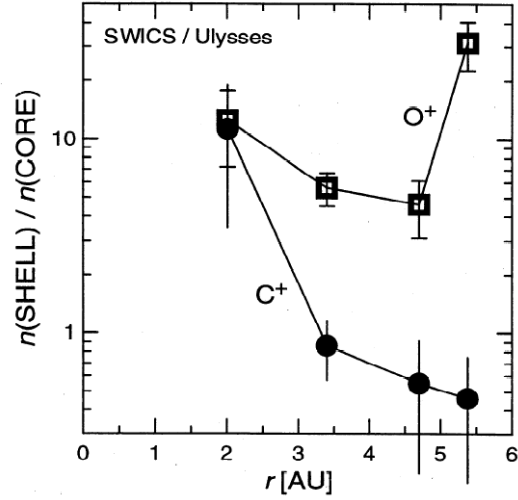
ions must exist. They found that the observed  $C^+$  signature most likely stems from a source close to the Sun (Fig. 1.7), hence the name inner-source pickup ions. They also found traces of inner-source  $O^+$  and  $N^+$  and thus were able to explain the aforementioned overabundance of the pickup ion  $w$ -spectra at small  $w$ 's.

Following studies by *Gloeckler et al.* [2000], *Schwadron et al.* [2000], and *Geiss et al.* [1996] have further shown that inner-source pickup ions have a composition similar to the solar wind, they show strong adiabatic cooling and they have a source  $\sim 30$  solar radii away from the Sun that is randomly distributed. The nature of the source, however, is still under debate. Four possible scenarios for the creation of inner-source pickup ions are summarized in *Allegrini et al.* [2005]. These scenarios involve

- Implantation of solar wind ions into small dust grains close to the Sun. Sputtering of the grain material then releases the implanted neutral solar wind atoms, which then undergo photo-ionisation by solar ultra violet radiation to form an inner-source of pickup ions [*Gloeckler et al.*, 2000], [*Schwadron et al.*, 2000].
- Solar wind neutralization or charge exchange at small dust grains close to the Sun, which act as thin carbon foils. Once the neutralized solar wind is ionized again, it can be measured as a pickup ion [*Wimmer-Schweingruber and Bochsler*, 2003].

Figure 1.7.

Ratio of the partial densities in two regions of the velocity distribution function (SHELL:  $w > 1.3$ , CORE:  $w < 1.2$ ). The data was collected with the SWICS instrument aboard Ulysses during times, where the spacecraft was near the ecliptic. The strong decrease of  $C_{\text{SHELL}}^+ / C_{\text{CORE}}^+$  suggests that there is not much  $C^+$  production beyond 3 AU, which is not compatible with an interstellar carbon source. The figure is taken from *Geiss et al.* [1995] with permissions from the Wiley Online Library under licence number 3101891110976.



- Neutral material released by sungrazing comets due to vaporization of cometary material [Bzowski and Królikowska, 2004]. This scenario, however, requires that inner-source pickup ions are produced locally.
- A reservoir of neutral grain material filled by dust-dust collisions close to the Sun [Mann and Czechowski, 2005] that produces an isotropic inner-source pickup ion signature.

The first two scenarios proposed by [Gloeckler et al., 2000] and [Wimmer-Schweingruber and Bochsler, 2003] are currently the most promising ones, as they are compatible with almost all inner-source pickup ion observations that were made between 1 AU and 5 AU. However, the poor knowledge of the dust distribution and missing in-situ measurements of inner-source pickup ions close to the Sun prevents a definite answer to the question how these particles are formed and from which reservoir they come. Throughout this work inner-source pickup ions are only of secondary interest, so that the interested reader should instead refer to *Kallenbach et al.* [2000] or *Allegrini et al.* [2005] for an overview of inner-source pickup ion studies.

## 1.4. Structure of this Work

In this chapter the theoretical background on the interstellar medium and interstellar- as well as inner-source pickup ions has been given (see sections 1.1, 1.2, and 1.3 respectively). In chapter 2 an overview of the STEREO mission and the PLASTIC sensor is presented. The two STEREO spacecraft carry the PLASTIC instruments, so-called time-of-flight mass spectrometer (see section 2.2), which we use for all pickup ion related studies in this thesis. The necessary steps to acquire and process pickup ion data are explained in section 2.3.

The research presented in this thesis covers three aspects of interstellar pickup ions as illustrated in Fig. 1.8.

- Chapter 3: The Distribution of Pickup Ions Inside the Heliosphere at 1 AU

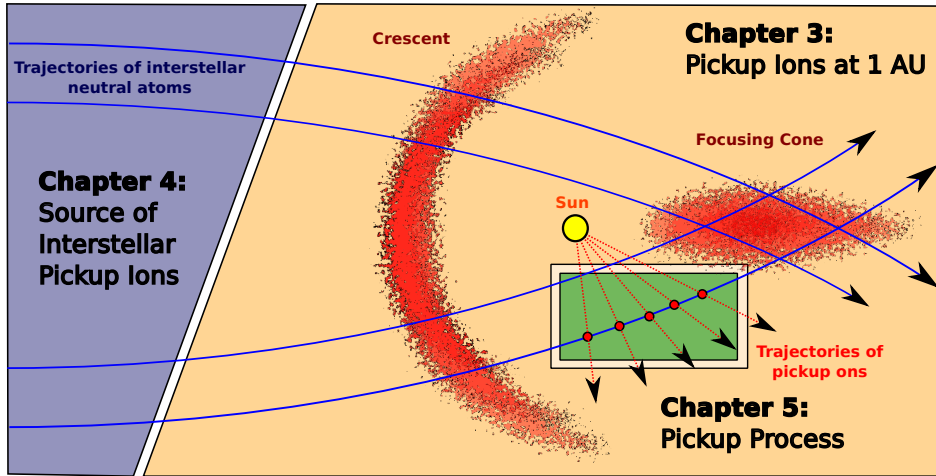


Figure 1.8.: Illustration of the three different aspects of pickup ion related research presented in this work. The spatial distribution of pickup ions in a distance of 1 astronomical unit from the Sun (yellow shaded area) is investigated in chapter 3.2. The source of interstellar pickup ions, the interstellar medium (blue shaded area), will be discussed in chapter 4.2. Finally, in chapter 5.2 the pickup process, i.e. the kinetic behaviour of interstellar  $\text{He}^+$  after its ionization, is explained (green shaded area).

- Chapter 4: The Source of Interstellar Pickup Ions: The Interstellar Medium
- Chapter 5: The Pickup Process and its Implications for the Velocity Distribution Function of Interstellar Pickup Ions.

Chapter 3 addresses the first important aspect of our pickup ion study - the distribution of pickup ions inside the heliosphere at 1 AU. Here we will describe our observation of the  $\text{Ne}^+$  focusing cone with STEREO/PLASTIC at 1 AU and its implications [Drews *et al.*, 2010]. This chapter also provides the necessary background on related pickup ion studies by other groups. In section 3.3.1 the performance of the Poisson Analysis that was used for the observation of the  $\text{Ne}^+$  focusing cone is tested and compared to a so-called box rate method.

In chapter 4 we investigate the source of interstellar pickup ions and derive the inflow direction of the interstellar medium  $\lambda_{\text{LISM}}$  as seen by an observer inside the heliosphere [Drews *et al.*, 2012]. Here we also compare our results to previously derived values of  $\lambda_{\text{LISM}}$  and discuss the existing deviation. In sections 4.3.1 and 4.3.2 we present a performance test of the analysis used to infer  $\lambda_{\text{LISM}}$  and discuss possible systematic biases that would influence the result of  $\lambda_{\text{LISM}}$ .

In chapter 5 we explain the pickup process and describe the kinetic properties of interstellar  $\text{He}^+$  immediately after its ionization. We also address the important implication of our research on existing pickup ion models [Drews *et al.*, 2013]. Section 5.3 contains an explanation of the Virtual Detector, which is a tool we used to transform a model of the pickup ion velocity distribution function into an expected count rate spectrum as seen from PLASTIC.

At the beginning of chapters 3, 4, and 5 also a brief introduction and overview of the respective chapter is given. Finally, chapter 6 contains a conclusion and outlook of this work.

## 2. Instrumentation

In this chapter we give a brief description of the instrumentation that is used for the pickup ion studies specified in sections 3.2, 4.2, and 5.2. Section 2.1 gives an overview of the Solar Terrestrial Relations Observatories - two twin spacecraft orbiting the Sun. Each spacecraft carries a science payload of 18 individual sensors. In this work we use the PLAsma and SupraThermal Ion Composition (PLASTIC) instrument to study pickup ions. The design and principle of operation of PLASTIC is described in section 2.2. In section 2.3 we describe the necessary steps to acquire and process the pickup ion data. The description of the STEREO mission and the PLASTIC instrument follows the description given in *Russell* [2008], *Galvin et al.* [2008] and *Drews* [2009].

### 2.1. STEREO

The Solar TERrestrial RELations Observatory mission (STEREO) was launched on October 2006. It consists of two near-identical spacecraft orbiting the Sun. Viewed from the Sun, the two spacecraft separate from Earth by roughly  $22^\circ$  per year, where STEREO Ahead (A) leads along and STEREO Behind (B) trails behind the orbit of Earth. The spacecraft are situated at a distance of around one Astronomical Unit (AU) with respect to the Sun, which varies by  $\sim 1\%$  for STEREO A and  $\sim 2\%$  for STEREO B due to the small eccentricity of the orbits. The orbital periods of STEREO A and B are 347 and 388 days respectively. An illustration of STEREO's orbit can be found in Fig. 2.1.

The specific scientific goals of the STEREO Mission are:

- Understand the causes and mechanisms of coronal mass ejection initiation.
- Characterize the propagation of coronal mass ejections through the heliosphere.
- Discover the mechanisms and sites of energetic particles acceleration in the low corona and the interplanetary medium.
- Improve the determination of the structure of the ambient solar wind [*Kaiser et al.*, 2008].

However, the persistent stream of in-situ data also allows the forecast of space weather, which is a secondary objective of the STEREO missions. Although pickup ion investigations are not a specific science goal of the mission, the combination of interplanetary magnetic field measurements with high cadence by IMPACT, measurements of ionized particles in the energy range of 1 keV/e to 80 keV/e with unprecedented statistics by PLASTIC, and the unique twin spacecraft setup at different locations along the orbit of Earth, makes it ideal for such an investigation. Mission success required a continuous operation of both spacecraft for a period of two years, which has been accomplished on January 23, 2009 [*Kaiser et al.*, 2008].

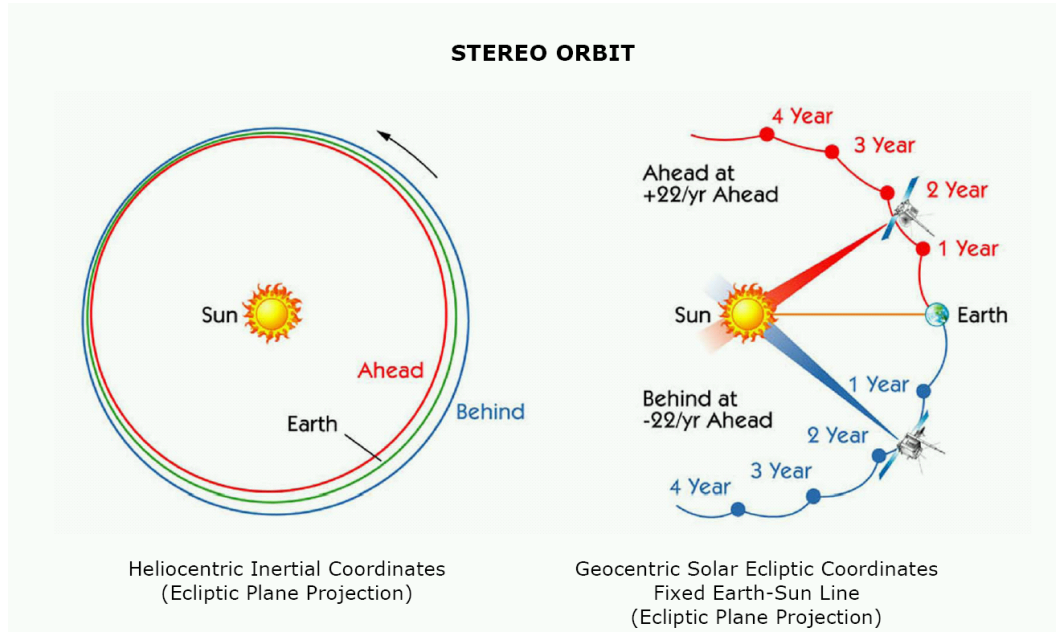


Figure 2.1.: Illustration of STEREO’s orbit in Heliocentric Inertial Coordinates (left) and Geocentric Solar Ecliptic Coordinates (right). STEREO A (red) and STEREO B (blue) are separating from each other by roughly  $45^\circ$  each year. Extracted from <http://stereo.gsfc.nasa.gov/img/STEREObooklet.pdf>.

The complete STEREO’s science payload consists of four instrument suites with a total of 18 individual sensors on each observatory [Russell, 2008]. The four suites are:

- The Sun Earth Connection Coronal and Heliospheric Investigation (SECCHI) provides an extreme ultraviolet imager, two white-light coronagraphs and a heliospheric imager to study the evolution of coronal mass ejections from the Sun towards their eventual impact at the Earth’s orbit in three dimensions.
- In-situ Measurements of Particles and CME Transients (IMPACT) consists of 7 sensors and measures the three dimensional distribution of solar wind plasma electrons, solar energetic particles, and the interplanetary magnetic field.
- STEREO/WAVES (SWAVES) measures radio disturbances and plasma waves from the Sun with three mutually orthogonal monopole antenna elements.
- The Plasma and SupraThermal Ion Composition (PLASTIC) studies properties of solar wind protons, alpha particles, and heavy ions as well as suprathermal particles.

An illustration of the spacecraft and its payload is shown in Fig. 2.2.

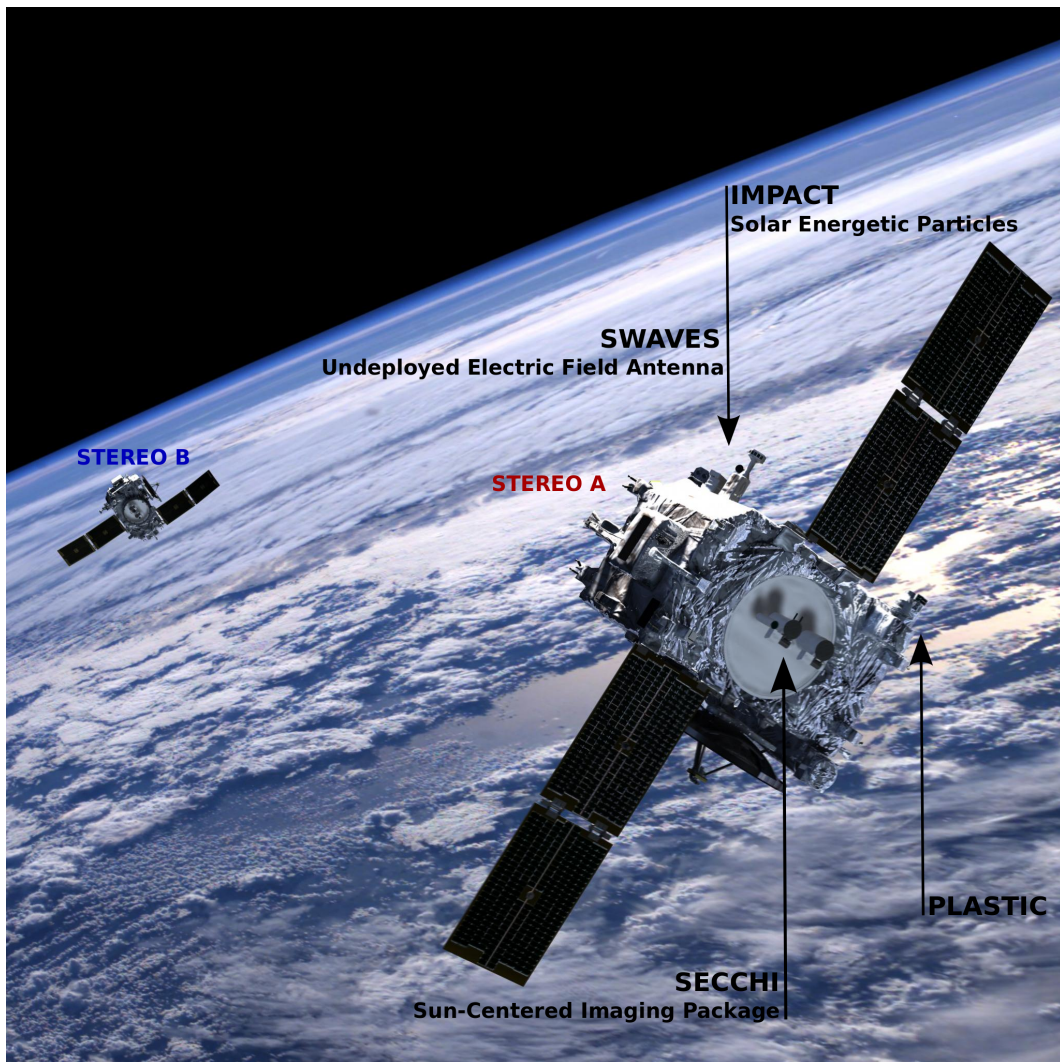
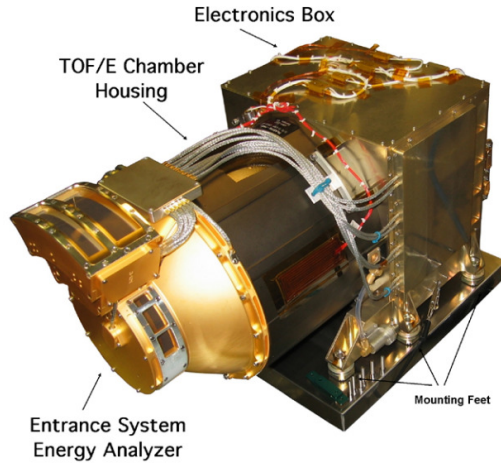


Figure 2.2.: Artistic presentation of the two STEREO spacecraft during the phasing orbit stage. One or two gravity-assist lunar swing-bys were performed to attain the final heliocentric orbits of STEREO A and B respectively (shown in Fig. 2.1). The illustration is taken from <http://airandspace.si.edu>, annotations by the author C. Drews.

Figure 2.3.

Photograph of the PLASTIC Flight Model, consisting of three main components: The Entrance System (golden, dome-like component) is divided into four different sections, Solar Wind Sector - Main Channel, Solar Wind Sector - Small Channel, Wide Angle Partition SSD and Wide Angle Partition NOSSD. The TOF/E chamber (black cylindrical center section) contains both time-of-flight and energy measurement equipment, while the Electronic Box comprises high voltage supplies and various electronics. The figure is taken from *Galvin et al.* [2008].



## 2.2. PLASTIC

The PLASma and SupraThermal Ion Composition instruments (PLASTIC) on the two STEREO spacecraft are linear time-of-flight mass spectrometers that measure in-situ properties of solar wind  $H^+$ ,  $He^{2+}$ , heavy ions, as well as pickup ions. PLASTIC provides a nominal energy-per-charge coverage of 0.3 keV/e to 80 keV/e and is capable to determine the angle of incidence of ions by a combination of different entrance apertures, complex deflection systems, and discrete or continuous position detectors that are discussed below. The instrument is divided into three main constituents. The Entrance System / Electrostatic Analyzer (ESEA) is used for the energy-per-charge measurement of ions. It is further divided into three different entrance apertures, i.e., the Solar Wind Section (SWS), the Wide Angle Partition SSD (WAPSSD), and the Wide Angle Partition NOSSD (WAPNOSSD), that together span a field-of-view of almost  $360^\circ$  in the ecliptic plane. In the Time-of-Flight / Energy chamber the time-of-flight and energy of incident particles is measured. The Electronic Box contains high voltage supplies as well as electronic boards necessary for the operation of the instrument [*Galvin et al.*, 2008]. A photograph of the instrument can be found in Fig. 2.3.

In the following we will describe PLASTIC's basic principle of work. We will characterize the ESEA and the Time-of-Flight / Energy chamber in more detail and describe how to derive an ion's mass, mass-per-charge, and velocity from the three measurements of the energy-per-charge, time-of-flight, and residual energy. The description of the PLASTIC sensor follows the description given in *Galvin et al.* [2008].

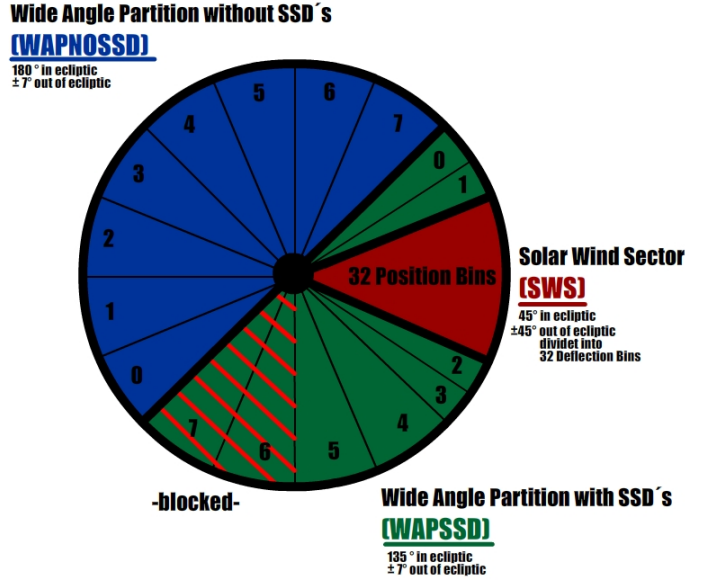
### 2.2.1. Entrance System / Energy Analyzer

PLASTIC measures both solar wind and suprathermal ion distributions and therefore has to span a wide range of different ion fluxes. By segmenting the Entrance System into four apertures with different geometry factors, PLASTIC is capable of measuring solar wind  $H^+$  and  $He^{2+}$  (Solar Wind Section (SWS) - Small Channel), solar wind heavy ions (SWS - Main Channel), and different types of suprathermal ion distributions (Wide



Figure 2.4.

The entrance system of PLASTIC is divided into three subsystems. The Solar Wind Sector (red) is centered on the connection line between the instrument and the Sun. It is accessible for incident particles in an angular range of  $-22.5^\circ$  to  $22.5^\circ$  in the ecliptic and  $-20^\circ$  to  $20^\circ$  out of the ecliptic. It also allows to distinguish between  $32 \times 32$  different incident angles in- and out-of-ecliptic that are linearly spaced in the given angular ranges. The WAPSSD (green) and WAPNOSSD (blue) sections complete the full  $360^\circ$  coverage in the ecliptic plane with 8 discrete anodes. WAPSSD and WAPNOSSD do not provide resolution in polar direction, i.e. out of the ecliptic. The figure is taken from *Drews* [2009].



Angle Partition (WAP) SSD and NOSSD) within one instrument. An illustration of the Entrance System as seen from the top is shown in Fig. 2.4. An illustration of the ESEA and its working principle is shown in Fig. 2.5

### ElectroStatic Analyzer (ESA)

After ions have entered the instrument through either the SWS or WAP they are focused at the focusing point (illustrated in Fig. 2.5) directly above the electrostatic analyzer. The ESA consists of two electrode pairs of toroidal domes that are cylindrically symmetric around the instrument azimuth, which allows PLASTIC to simultaneously collect solar wind ions within a  $360^\circ$  field of view in the ecliptic. Both domes can be swept through 128 different logarithmically spaced voltages and therefore act as an energy-per-charge filter for incident ions. A complete sweep from a nominal energy-per-charge of  $E/q = 0.3$  keV/e up to  $E/q = 80$  keV/e takes  $\sim 56$  seconds, which is followed by  $\sim 4$  seconds used for sampling housekeeping, data transfer, resetting registers, implementing commands, and setting up the next collection cycle [Galvin *et al.*, 2008]. The relative uncertainty of the energy-per-charge measurement, which is governed by the spatial separation of the two domes, is  $\Delta E/q = 6\%$ . The voltage of the polar deflectors required for the measurement of the polar incident angle are matched for each of the applied ESA steps and stepped every 12.8 ms. The nominal energy-per-charge response of the ESA is given by

$$E/q \text{ [keV/e]} = 0.2 \cdot 1.04895^{127 - E/q\#}, \quad (2.1)$$

where  $E/q\#$  denotes the concurrent  $E/q$  step number of the ESA cycle. An illustration of the ESEA can be found in Fig. 2.5. A detailed discussion of the ESEA and its pre-flight calibration can be found in Galvin *et al.* [2008].

### Solar Wind Section (SWS)

The center of the Solar Wind Section (SWS) is aligned along the connection line between the spacecraft and the Sun and provides a  $\pm 22.5^\circ$  field of view in azimuthal and  $\pm 20^\circ$  in polar direction. It is divided into two entrance apertures, the Main- and Small-Channel, to account for the wide variety of different fluxes of solar wind ions. The solar wind consists of  $\sim 96\%$   $\text{H}^+$ ,  $\sim 3.9\%$   $\text{He}^{2+}$  and less than  $\sim 0.1\%$  heavy ions, whereas the most abundant heavy ion  $\text{O}^{6+}$  is still  $\sim 1500$  times less abundant than solar wind protons [von Steiger *et al.*, 2010]. To combine measurements of the abundant solar wind component as well as heavy ions, PLASTIC makes use of two different entrance apertures:

- The Main-Channel provides a large geometry factor ( $3 \cdot 10^{-3} \text{ cm}^2\text{eV}/\text{eV sr}$ ), that allows to measure a statistically relevant flux of solar wind heavy ions as well as pickup ions. If exposed to the far more abundant solar wind protons however, the geometry factor of the Main-Channel would quickly cause saturation and probably damage to the instrument, and certainly premature aging of the Micro Channel Plates
- The Small-Channel provides a small geometry factor ( $6 \cdot 10^{-7} \text{ cm}^2\text{eV}/\text{eV sr}$ ) and is suited to measure the abundant components of the solar wind, i.e.  $\text{H}^+$  and  $\text{He}^{2+}$ . The Small-Channel is, due to its small collection power, not able to measure solar wind heavy ions with sufficient statistics.

During operation, PLASTIC alternates between the Small- and Main-Channel triggered by a monitored count rate (see Fig. 2.5 for details). Spatial resolution in polar direction, i.e. out of the ecliptic plane, is realized by a combination of polar deflectors, which can be stepped through 32 different voltages. These so-called deflection steps are swept through within 435 ms, 12.8 ms per deflection step, and filter incoming particles of constant mass-per-charge ratio by polar direction. In combination with the electrostatic analyzer, PLASTIC is able to distinguish between 32 polar angles of incident ions that are linearly spaced within the range  $\pm 20^\circ$ . The polar angle acceptance per deflection step is  $\sim 1.2^\circ$ . Furthermore, the azimuthal angle of incidence ions is reported by a resistive anode position detector. It covers 32 azimuth angles that are linearly spaced in the range of  $\pm 22.5^\circ$  in the ecliptic plane with an angular acceptance of  $\sim 1.4^\circ$  per position bin.

### Wide Angle Partition (WAP)

The Wide Angle Partition has a larger geometry factor than either of the two SWS entrance slits and is therefore suited to measure the less abundant suprathermal ions. The WAP is divided into two different sections. WAPSSD covers a field of view of  $135^\circ$  in the ecliptic adjacent to the SWS. For WAPSSD the residual energy of incident ions is measured by a solid state detector after passage of the electrostatic analyzer. WAPNOSSD lacks these measurements and secondary electrons emitted from the carbon foil are instead directly guided onto the MCPs (see Fig. 2.6). WAPNOSSD completes the almost  $360^\circ$  coverage with a field of view of  $180^\circ$  in the ecliptic. The azimuthal incident angle of incoming ions is reported by a combination of 8 discrete anodes for WAPSSD and WAPNOSSD each. They provide a varying angular acceptance as can be seen from Fig.

2.4. The Wide Angle Partition has a polar angle acceptance of  $\pm 7^\circ$  but does not provide information on the out-of-ecliptic incident angle of ions.

### 2.2.2. Time-of-Flight / Energy Chamber

#### Time-Of-Flight (TOF)

After passage of the ESA ions are post-accelerated by constant a voltage drop of 20kV and enter the Time-Of-Flight / Energy chamber through a  $\sim 144 \text{ \AA}$  thick carbon foil. Traversing the carbon foil has two important consequences. First of all, a shower of secondary electrons is emitted, which is guided by a system of electrodes onto a Micro Channel Plate (MCP) to trigger the start signal for an ion's time-of-flight measurement. Secondly, ions lose a fraction of their energy due to interactions with the carbon foils nuclei and electrons. This causes a net-deceleration of the ion, which has to be considered when interpreting the time-of-flight measurement. After the ion has traversed the 8 cm (SWS, WAPSSD) or alternatively 5.6 cm (WAPNOSSD) long time-of-flight path it hits one of PLASTIC's sixteen solid state detectors (SWS, WAPSSD) or alternatively directly the MCP (WAPNOSSD). Ions hitting the SSD cause a shower of secondary electrons, which are then steered onto a MCP where they trigger the time-of-flight stop signal and complete the time-of-flight,  $\tau$ , measurement. As aforementioned,  $\tau$  is lengthened by the energy loss of ions passing through the carbon foil. Furthermore, angular scattering due to interaction of ions with the carbon foil's nuclei or defects of the foil's atomic structure can alter the time-of-flight measurement. These effects are implicitly considered in the energy loss parameter  $\alpha(E, m)$ , which is introduced in section 2.2.3 and was derived by an in-flight calibration in *Drews* [2009]. A more elaborate discussion on the energy loss parameter can be found in *Allegrini* [2007], where the ion optical calibration of the PLASTIC sensor is described. An illustration of PLASTIC's Time-Of-Flight / Energy chamber is shown in Fig. 2.6.

Finally, the conversion from time-of-flight channel,  $\tau_{\#}$ , to  $\tau$  [ns] is described by the following equation

$$\tau[\text{ns}] = \tau_{\#} \cdot 0.25 + 1.3. \quad (2.2)$$

The equation is based on pre-flight calibration as described in *Allegrini* [2007].

#### Residual Energy

To measure the energy of ions, sixteen Solid State Detectors (SSD) pixels are located at the end of the time-of-flight path in the SWS and WAPSSD. They are custom-made Canberra Passivated Implanted Planar Silicon (PIPS) detectors with an equivalent entrance window of 25 nm silicon. Energies are measured within a range of up to  $\sim 2000 \text{ keV}$  and converted in 1024 linearly spaced SSD channel. However, due to the dead layer, phonon excitation, or electron-hole-pair recombination inside the detector only a fraction of the ion's energy is measured. This, so-called Pulse Height Defect  $\beta(E, m)$ , is a function of an ion's mass and energy and introduced in section 2.2.3, where it is used to derive a particles mass  $m_{\text{ion}}$ . Because the SSDs of ACE/SWICS have very similar characteristics compared to PLASTIC's SSDs, values from *Köten* [2009] have been adapted and further refined for PLASTIC's SSDs in *Drews* [2009].

The average conversion from SSD channel,  $E_{\#}$ , to  $E$  [keV/e] for the eight different SSD pixels is described by the following equation and based on pre-flight calibrations

$$E[\text{keV/e}] = E_{\#} \cdot 2.2 - 6.4. \quad (2.3)$$

Ions hitting the SSDs also cause a shower of secondary electrons used as a trigger for the stop signal of the time-of-flight measurement. The calibration of the solid state detectors, including information on the energy response function, is described in *Blush et al.* [2005].

### 2.2.3. Principle of Work

Fig. 2.7 shows longterm data collected with the SWS of STEREO A/PLASTIC for an energy-per-charge of 7.9 keV/e. Because the independent measurements of the time-of-flight,  $\tau$ , residual energy,  $E$ , and energy-per-charge,  $E/q$ , depend on the mass, mass-per-charge and velocity of incident particles, plotting the energy over the time-of-flight for a given energy-per-charge step allows us to visually distinguish different particles species and charge states. The position of a small sample of solar wind as well as pickup ions in the longterm data is also shown in Fig. 2.7. The expected positions of these ions were derived in *Drews* [2009]. Obviously, uncertainties of the  $\tau$  and  $E$  measurements can cause overlap of adjacent ion species, which makes species classification a highly non-trivial subject. A discussion on species classification can be found in chapters 2.3 and 3.2.

The three measurements of the energy-per-charge  $E/q$ , time-of-flight  $\tau$ , and residual energy  $E$  of incoming particles are connected to an ion's mass  $m_{\text{ion}}$ , mass-per-charge  $\frac{m_{\text{ion}}}{q_{\text{ion}}}$ , and velocity  $v$  by the following set of equations,

$$\frac{m_{\text{ion}}}{q_{\text{ion}}} = 2 \cdot (E/q + V_{\text{PAC}}) \alpha(E, m) \left(\frac{\tau}{d}\right)^2 \quad (2.4)$$

$$m_{\text{ion}} = 2 \cdot \frac{E}{\beta(E, m)} \left(\frac{\tau}{d}\right)^2 \quad (2.5)$$

$$v = \sqrt{2 \cdot E/q \frac{q_{\text{ion}}}{m_{\text{ion}}}}. \quad (2.6)$$

Here  $d$  is the flight path in the TOF chamber and  $V_{\text{PAC}}$  the post acceleration voltage.  $\alpha(E, m)$  denotes the species dependent energy loss of ions in the carbon foil and  $\beta(E, m)$  denotes the pulse height defect of the solid state detector. Both functions were determined by in-flight calibrations in *Drews* [2009]. With an event's mass, mass-per-charge, and velocity we have derived an event's species and energy spectrum, which in combination with the angles of incidence is all we need for the following pickup ion study. The interested reader may refer to *Köten* [2009] for a detailed description of time-of-flight mass spectrometers and the difficult task of their in-flight calibration. Throughout this work we will discuss certain aspects of PLASTIC's in-flight calibration at the time they are required to follow our pickup ion study.

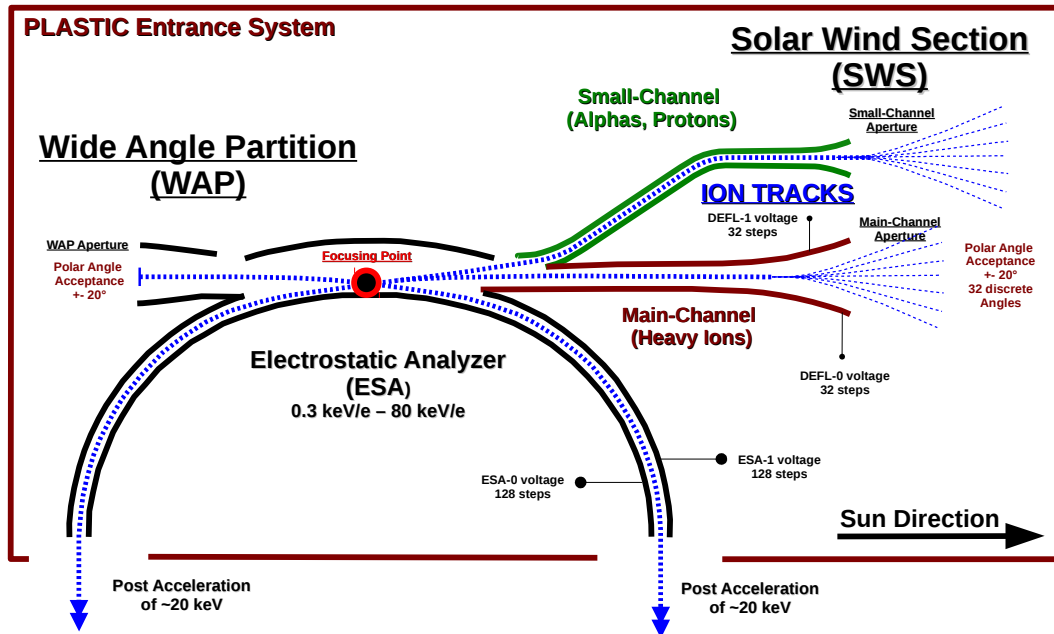


Figure 2.5.: Illustration of a 2-D cut through PLASTIC's Entrance System / Electrostatic Analyzer (ESEA). Ions enter the instrument either through the Solar Wind Section (right side of the figure) or through the Wide Angle Partition (left side). The Solar Wind Section is pointing towards the Sun and has an angular acceptance of  $45^\circ$  in- and  $\pm 20^\circ$  out of the ecliptic. The Wide Angle Partition completes the almost  $360^\circ$  coverage in the ecliptic and has an out-of-ecliptic acceptance of  $\pm 7^\circ$ . Ions that enter the instrument (blue tracks) are filtered by their energy-per-charge ratio with an electrode pair of toroidal domes that are used as an electrostatic analyzer (ESA-0, ESA-1). Both voltages are swept through 128 different, logarithmically spaced values to cover the energy-per-charge range between  $0.3 \text{ keV/e}$  to  $80 \text{ keV/e}$ . The Solar Wind Section is further divided into two entrance apertures, whereas only one aperture is active at once. Channel switching is based upon a monitored count rate. The less abundant solar wind heavy ions as well as pickup ions are collected first in the initial part of the energy-per-charge stepping cycle by enabling the Main-Channel aperture (red). When the ion flux reaches a critical value on a specific energy-per-charge step, which usually marks the beginning of solar wind  $\text{H}^+$  and  $\text{He}^{2+}$  to enter the instrument, the IDPU switches from the Main-Channel to the Small-Channel (green) with a much smaller geometry factor for the rest of the energy-per-charge cycle. The Main- and Small-Channel also allow to select ions by their out-of-ecliptic angle within the range of  $\pm 20^\circ$  by a pair of polar deflectors, which are ramped through 32 different deflection voltages (DEFL-0, DEFL-1).

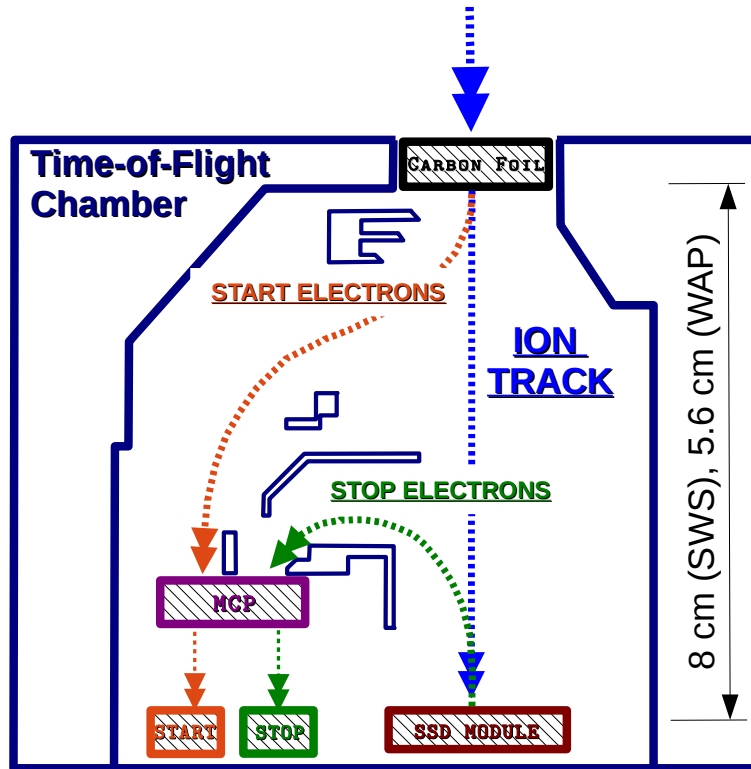


Figure 2.6.: Illustration of PLASTIC's time-of-flight/energy-chamber. Ions (blue track) enter by passing a  $3.5\mu\text{g}/\text{cm}^2$  thin carbon foil where they emit secondary electrons (orange track). These electrons are guided by a system of electrodes onto a Micro Channel Plate (MCP). The amplified electron cascade is then steered onto the start-anode, which triggers the start signal of the time-of-flight measurement. After passage of the carbon foil, ions travel a distance of 8 cm to a Solid State Detector (SSD) in the Solar Wind Section or alternatively a distance of 5.8 cm directly to the MCP for the Wide Angle Partition. Ions hitting the SSD will produce secondary electrons that are steered by a pair of electrodes onto the MCP for the time-of-flight stop signal. The complex design of the time-of-flight/energy chamber, i.e. the non-trivial guidance of secondary electrons by a system of electrodes onto the MCP, was required due to the overall complexity of the ESEA. Unfortunately, the complex design also increased the overall uncertainty of the time-of-flight measurement, which would mainly be governed by angular spread and energy straggling of the ions' carbon foil passage.

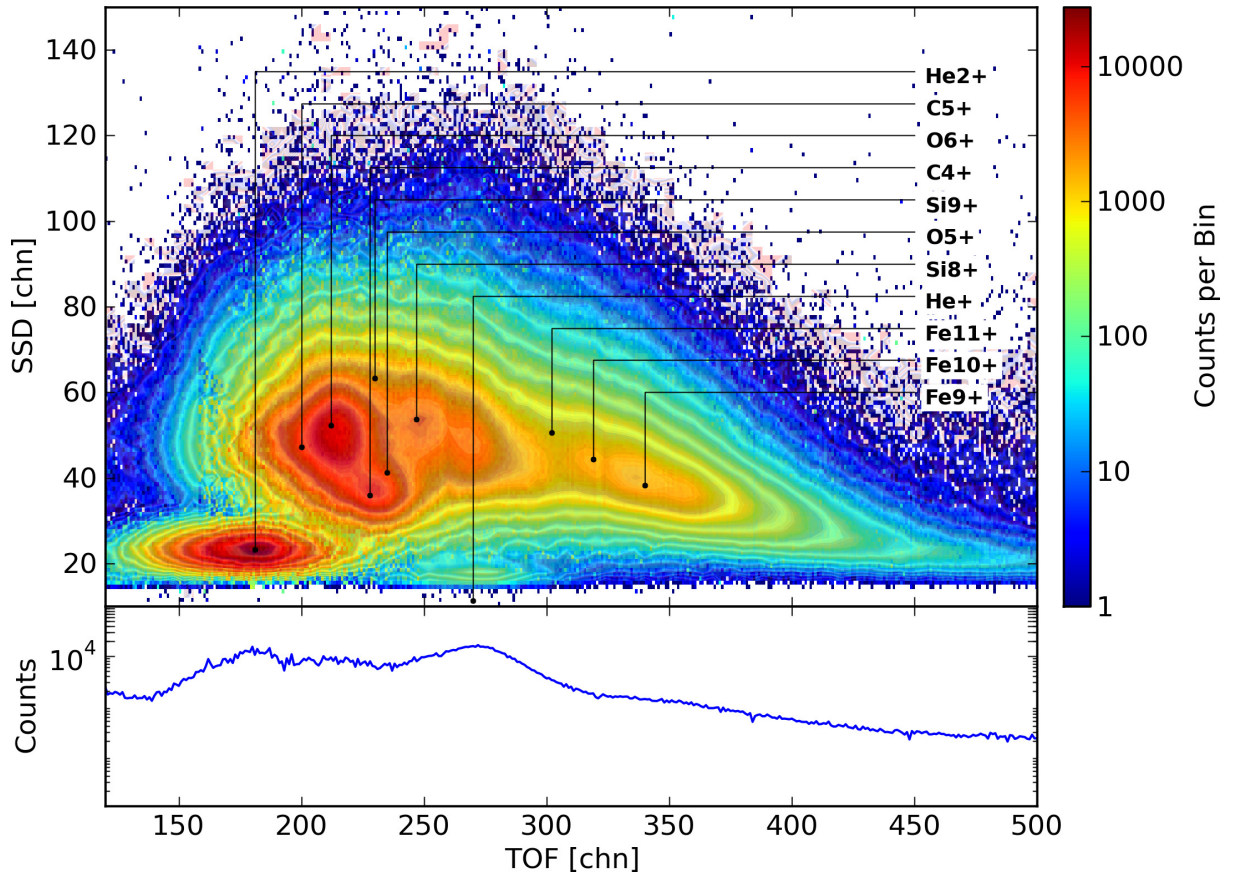


Figure 2.7.: PLASTIC Pulse Height Analysis (PHA) data measured with the Solar Wind Section in a time period of 1400 days beginning in February, 2007. All events had an energy-per-charge of  $7.9 \text{ keV/e}$  ( $v_{\text{He}^+} = 633 \text{ km/s}$ ) which corresponds to ESA step 50. The upper panel shows a color coded intensity plot of the PHA data sorted by time-of-flight (x-axis) and energy deposition in the solid state detector (y-axis). Both quantities are shown in instrumental channel numbers. The bottom panel shows so-called Double Coincidence Rates (DCR) - events that did not trigger a signal in the solid state detector. Furthermore, the expected positions of several solar wind as well as  $\text{He}^+$  pickup ions are shown, which were derived in *Drews* [2009].

## 2.3. Data Acquisition

PLASTIC provides two different types of data products. The matrix rate data is produced by an on-board algorithm that assigns to each incident event a given mass and mass-per-charge based on the event's energy-per-charge,  $E/q$ , time-of-flight,  $\tau$ , and deposited energy in the solid state detector,  $E$ . Events that lie within a certain mass and mass-per-charge range are then assigned to their respective matrix rate that is defined by a look-up table. These tables link the mass and mass-per-charge information to a certain ion or, in some cases, a mixture of multiple ions. Because the operation of a simple "look-up" is performance-wise much faster than a mass and mass-per-charge algorithm (see Eq. 2.4, 2.5), these tables prove to be an efficient way to determine the species of incident events.

The matrix rates contain information about the number of measured events of a given ion or mixture of ions within a certain time interval and energy range. They also provide information about the instrumental position and deflection bin, i.e. the incident angle of ions. The resolution of these rates may vary depending on the particular rate. A complete overview of the available matrix rates can be found in *Galvin et al.* [2008]. However, matrix rates do not provide any information on the time-of-flight and deposited energy in the SSD, which, in case of a defective look-up table, renders them to be very disadvantageous. Without the  $\tau$  and  $E$  information it is impossible to determine  $m_{\text{ion}}$  and  $m_{\text{ion}}/q_{\text{ion}}$  retrospectively. As a result an incorrect allocation by the look-up table can not be undone. In *Drews* [2009] we have shown that the currently used look-up tables, which are based on pre-calibrations, are indeed far from ideal. The mass and mass-per-charge ranges provided by the look-up table insufficiently cover the respective mass and mass-per-charge range of an ion's matrix rate - even for common solar wind ions such as  $\text{He}^{2+}$  and  $\text{O}^{6+}$ . As a result only a fraction of events is properly allocated to their respective rate, while in other cases events are simply misassigned.

The pickup  $\text{He}^+$  distribution is covered by  $\sim 50\%$  of its respective mass and mass-per-charge range assigned by the look-up table. Especially no spillover contaminates the  $\text{He}^+$  rate rendering it suitable for our purposes. For  $\text{C}^+$ ,  $\text{N}^+$ ,  $\text{O}^+$ , and  $\text{Ne}^+$ , however, only a consolidated heavy pickup ion rate exists. Considering that these heavy pickup ions exhibit quite different properties in terms of velocity and longitudinal distributions in the heliosphere, it is required to analyse each of the heavy pickup ions separately. Therefore so-called Pulse Height Analysis Data (PHA) is used for our further analysis - the second data product PLASTIC provides.

### 2.3.1. Pulse Height Analysis Data

Pulse Height Analysis data (PHA) provide the most detailed information available. Each incident event that satisfies the event selection logic conditions is characterized by the following set of information.

- $E/q_{\#}$  - Instrumental energy-per-charge step  
There are 128 logarithmic spaced energy-per-charge steps  $E/q_{\#}$  that are connected to the  $E/q$  information of an event by

$$E/q[\text{keV/e}] = 0.2 \cdot 1.04895^{127 - E/q_{\#}}. \quad (2.7)$$

- $\tau_{\#}$  - Instrumental time-of-flight channel  
The linearly spaced time-of-flight channel  $\tau_{\#}$  represents an ion's time-of-flight  $\tau$



through the 8 cm long time-of-flight path. It is connected to  $\tau$  by

$$\tau[\text{ns}] = 0.25 \cdot \tau_{\#} + 1.3. \quad (2.8)$$

- $E_{\#}$  - Instrumental energy deposition in the SSD

The linearly spaced energy deposition channel is linked to an ion's energy  $E$  by

$$E[\text{keV}] = 2.2 \cdot E_{\#} - 6.4. \quad (2.9)$$

- $\theta_{\#}$  Instrumental latitudinal angle of incidence

Inside the Solar Wind Section PLASTIC allows to distinguish between different latitudinal inflow angles of incident ions by a pair of deflector electrodes. The 32 so-called deflection steps  $\theta_{\#}$  are linearly spaced in the range between  $-20^{\circ}$  to  $20^{\circ}$  with respect to the orbital plane of the spacecraft and have a latitudinal acceptance of  $\Delta\theta = 2^{\circ}$ . Outside the Solar Wind Section PLASTIC does not provide any latitudinal information.

- $\phi_{\#}$  Instrumental azimuthal angle of incidence

A resistive anode position detector inside the Solar Wind Section provides information on the azimuthal inflow angle of incident ion. It can distinguish between 32 different azimuthal angles, that are linearly spaced in the range of  $-22.5^{\circ}$  and  $22.5^{\circ}$ . The two center position  $\phi_{15,16}$  are centered around the connecting line between the spacecraft and the Sun. The azimuthal acceptance of  $\phi_{\#}$  is  $\sim 3^{\circ}$ . The WAPSSD and WAPNOSSD sections each come with 8 discrete anodes which complete the  $360^{\circ}$  azimuthal coverage. These 16 discrete anodes have different azimuthal acceptances and are non-uniformly spread over an angular range of  $315^{\circ}$ . A detailed description of their characteristics can be found in chapter 2.2.

- $Q_{\#}$   $90^{\circ}$  Triggered instrument quadrant

- $SSD_{\#}$  Triggered SSD Pixel

Measurement of  $E$  inside the Solar Wind Section is performed with 8 independent SSD pixel  $SSD_{\#}$  that are linearly spaced between  $SSD_0$  and  $SSD_7$ . They can be used as an independent source for the azimuthal inflow angle of incident ions.

- $SEC_{\#}$  Triggered Instrument Section

The instrument is subdivided into four different sections - The Solar Wind Section ( $SEC_{0,1}$ ), the WAPSSD ( $SEC_2$ ), and the WAPNOSSD ( $SEC_3$ )

- $P_{\#}$  Events priority assignment

Due to the mission's limited telemetry bandwidth each event is assigned to a priority number  $P_{\#}$  that determines the likelihood of an actual transmission of that event. The priority number is based on the mass and mass-per-charge information.  $P_3$  (heavy ions including  $C^+$ ,  $N^+$ ,  $O^+$ , and  $Ne^+$ ) represents the highest priority, while  $P_0$  (main solar wind ions such as  $H^+$  and  $He^{2+}$ ) stands for lowest priority. A detailed description of the priority assignment can be found in *Galvin et al.* [2008] or *Drews* [2009].

### 2.3. DATA ACQUISITION

---

PLASTIC is capable of processing 512 PHA events per instrumental energy-per-charge step which adds up to a total of 65536 PHA events per minute. However, due to PLASTIC's limited telemetry allocation of 3kB/s only a small sample of 768 events can be transmitted to Earth while the remainder of the PHA data is only considered for the creation of the matrix rates - a heavily compressed version of the available data. The chosen PHA sample transmitted is solely based on the on-board priority assignment, which means that the sample not necessarily reflects the expected composition of the solar wind and pickup ions. Instead the priority assignment heavily favors ions of high energy-per-charge with masses  $m \geq 4$  amu ( $\text{He}^+$ ,  $\text{O}^{6+}$ ,  $\text{Fe}^{7+,8+,9+}$ , heavy pickup ions) over ions of lower energy-per-charge with masses  $m \leq 4$  amu ( $\text{H}^+$ ,  $\text{He}^{2+}$ ). To account for the priority based sample selection it is necessary to apply a so-called base rate weighting to the transmitted PHA data. It assigns to each transmitted PHA word a respective base rate weighting factor

$$b = N_{PHA}/T_{PHA}, \quad (2.10)$$

where  $N_{PHA}$  is the number of detected and  $T_{PHA}$  the number of transmitted PHA events of the respective priority  $P_{\#}$ , energy-per-charge step  $E/q_{\#}$ , section  $SEC_{\#}$  and five minute fraction of the day. Applying the base rate factor to the PHA data means that a PHA event is occasionally treated not as a single but instead as a collection of PHA events with the effect that the PHA data will properly reflect the solar wind and pickup ion composition. This procedure, however, can be also misleading, as it not only multiplies the number of PHA events, but also the accompanied informations of the time-of-flight, residual energy, and incident angles. As a consequence few events with a high base rate weighting factor could probably distort the observed  $\tau$ -,  $E$ -,  $\phi$ -, and  $\theta$ -distributions.

In general, pickup ions, with the exception of  $\text{H}^+$ , have at a fixed velocity a higher energy-per-charge than solar wind ions, which has two advantageous consequences. First of all, the priority bases selection scheme favors pickup ions over the more abundant solar wind ions, which means that most of the pickup ion data will be available as PHA data. As a result, we do not have to deal with a possible distortion of the  $\tau$ -,  $E$ -,  $\phi$ -, and  $\theta$ -distributions coming from base rate weighting. Secondly, pickup ions with masses  $m > 4$  amu are, at a given energy-per-charge step, well separated in terms of time-of-flight from the main solar wind constituents. This allows us to determine the species of heavy pickup ions solely from an event's mass-per-charge information, which reduces the 3-dimensional problem of species classification ( $E/q$ ,  $\tau$ ,  $E$ ) to a 2-dimensional one ( $E/q$ ,  $\tau$ ).

Figure 2.8 shows a sample of the transmitted PHA data that was collected during a period of 1400 days, beginning in February 2007, at an energy-per-charge of 42.2 keV/e. The top panel shows so-called Triple Coincidence Rates (TCR) events, i.e. events that triggered an  $E/q$ ,  $\tau$  (x-axis), and  $E$  (y-axis) signal, while the bottom panel shows Double Coincidence Rates (DCR) events, i.e. events with only a corresponding  $E/q$  and  $\tau$  signal. Most events without a corresponding energy deposit in one of the solid state detectors had an energy  $E$  that was smaller than the solid state detector threshold  $E_T$ . The purpose of the SSD threshold is to suppress noise of the SSD, which would otherwise waste a large part of the limited telemetry reserved for the PHA data.  $E_T$  was generally set to  $\sim 9.2$  keV ( $E_{14}$ ) for the observed time period. However, it has also been subject to frequent changes during the whole mission duration, which results in a non-constant  $E$  cutoff for PHA data accumulated over prolonged time periods (compare  $E_{10-16}$  in Figure 2.8). In

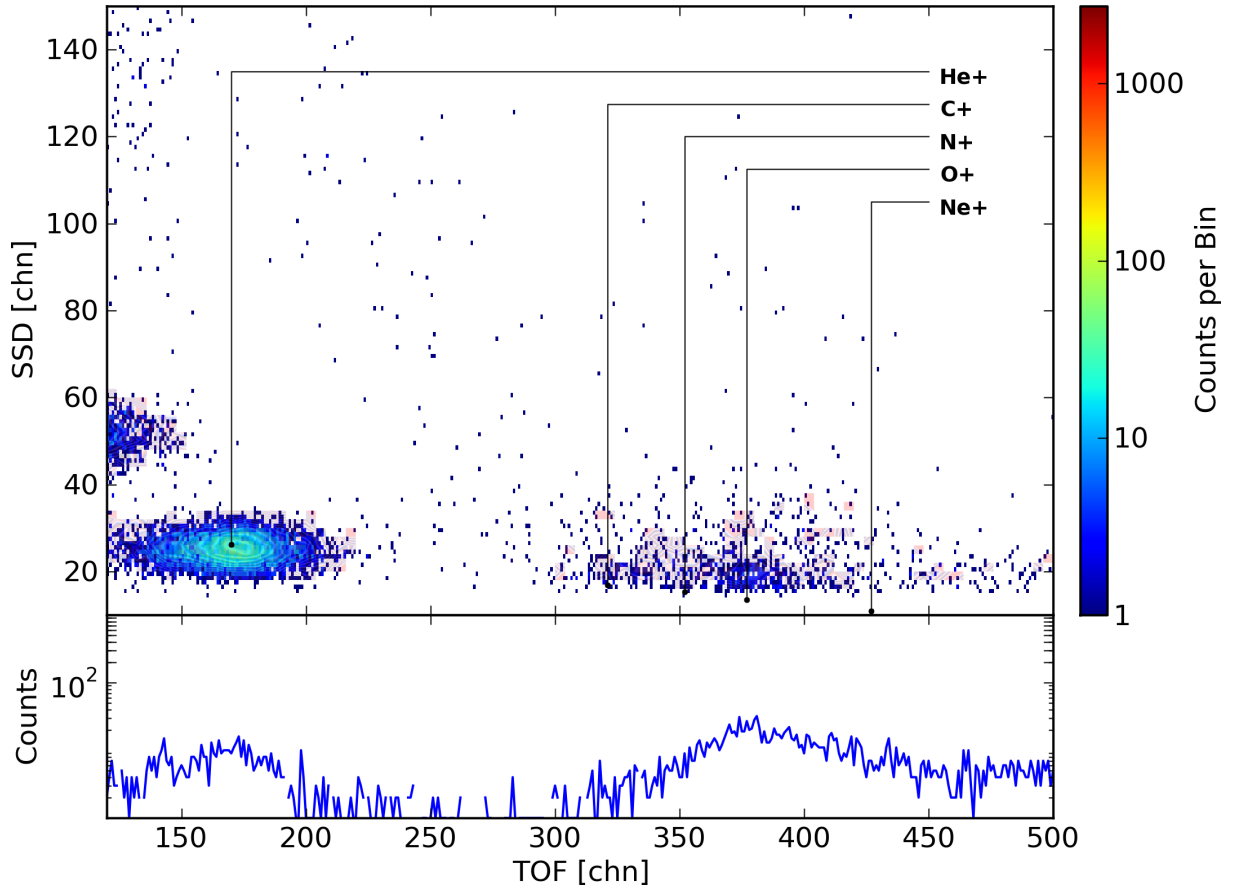


Figure 2.8.: PLASTIC Pulse Height Analysis (PHA) data measured with the Solar Wind Section in a time period of 1400 days beginning in February, 2007. All events had an energy-per-charge of 42.2 keV/e ( $v_{\text{He}^+} = 1462$  km/s), which corresponds to  $E/q_{15}$ . The expected position of  $\text{He}^+$ ,  $\text{C}^+$ ,  $\text{N}^+$ ,  $\text{O}^+$ , and  $\text{Ne}^+$  are shown.

addition, the probability to trigger a signal in one of the solid state detectors is even for events with  $E > E_T$  not 100% and a function of the particle's mass, energy and the detector characteristics, e.g. the dead layer of the SSD. A brief overview on the SSD characteristics and efficiency can be found in *Galvin et al.* [2008].

The presented PHA sample at  $E/q_{15}$  shows the most abundant pickup ions measurable with PLASTIC, i.e.  $\text{He}^+$  ( $v_{\text{He}^+} = 1462$  km/s),  $\text{C}^+$  ( $v_{\text{C}^+} = 843$  km/s),  $\text{N}^+$  ( $v_{\text{N}^+} = 781$  km/s),  $\text{O}^+$  ( $v_{\text{O}^+} = 730$  km/s), and  $\text{Ne}^+$  ( $v_{\text{Ne}^+} = 653$  km/s). Because the velocity of an ion is a function of its mass and the instrumental energy-per-charge step (see Eq. 2.6), singly charged pickup ions of different masses have different velocities at a given  $E/q_{\#}$ . As a result, the expected time-of-flight after an ion's passage of the carbon foil is unique and a good indicator for its species. Of all shown pickup ions  $\text{He}^+$  has the lowest mass and consequently its expected time-of-flight ( $\tau_{\text{He}^+} \sim 170$ ) is the smallest with respect to the remaining pickup ions. During passage of the thin carbon foil, however, ions lose a fraction of their energy. The energy loss is not only a function of an ion's energy but also a function of the particle's mass, which makes it rather complicated to find an analytical expression for the expected time-of-flight positions. A general rule of thumb is: The higher

### 2.3. DATA ACQUISITION

---

the mass-per-charge of an ion at a given  $E/q_{\#}$  the higher their expected time-of-flight position. For ions that have a very similar mass-per-charge but different charge state, e.g.  $\text{He}^+$  and  $\text{Fe}^{14+}$ , the ion with the higher charge state will have a slightly smaller expected time-of-flight position due to the instrumental post acceleration.

Because singly charged pickup ions have quite unique mass-per-charges with respect to solar wind ions, we don't necessarily need the expected  $E_{\#}$  position to identify their species. Solar wind ions on the other hand can have numerous charge states and therefore can also show a strong overlap in mass-per-charge space that requires further measurement of their energy  $E$  or rather mass  $m_{\text{ion}}$  for a clear species identification. The energy measurement after passage of the carbon foil is performed by several solid state detectors that have similar detector characteristics. The measured energy  $E$  of an ion is due to the Pulse Height Defect (PHD) always smaller than the actual energy  $E_{\text{ion}}$  of the respective ion. The PHD describes the energy loss caused by the SSD dead layer, phonon excitation, and electron-hole-pair recombination and scales between zero and one. Generally the PHD increases with increasing ion masses, which is also the reason why the pickup ion distributions in Figure 2.8 show a decreasing expected  $E_{\#}$  position with increasing masses.

As already stated, for a definite identification of the pickup ion species we need the expected time-of-flight (and optionally the residual energy) of each pickup ion species as a function of the instrumental energy-per-charge step  $E/q_{\#}$ . Finding the expected time-of-flight is primarily a matter of finding a suitable expression for the energy loss due to an ion's passage of the thin carbon foil. Such an analysis has already been performed in *Dreus* [2009] using the simulation program "The Stopping and Range of Ions in Matter" (SRIM) [*Biersack et al.*, 2008], which utilizes results of several stopping experiments for a semi-empirical model of the energy loss of particles in matter. With that we can derive the energy and species dependent energy loss parameter

$$\alpha(E, m_{\text{ion}}) = E_{\text{ion}}^{-1} \int_0^{d_{\text{foil}}} \frac{dE}{dx} dx, \quad (2.11)$$

that is required for the expected time-of-flight

$$\tau = \sqrt{\frac{1}{2} \frac{m_{\text{ion}}}{q_{\text{ion}}} \cdot ((E/q + V_{\text{PAC}}) \cdot \alpha(E, m_{\text{ion}}))^{-1}} \cdot d. \quad (2.12)$$

Here,  $d_{\text{foil}} = 144 \text{ \AA}$  denotes the carbon foil thickness,  $dE/dx$  the differential energy loss of the particle,  $V_{\text{PAC}} = 20 \text{ kV}$  the post-acceleration voltage, and  $d = 8 \text{ cm}$  the time-of-flight path.

The expected residual energy of ions was derived by performing a cross-calibration of the PHD between the SSDs of SWICS on-board ACE with the SSDs on-board PLASTIC, which are both Passivated Ion Implanted Planar (PIPS) detectors with very similar characteristics. With the energy and species dependent PHD parameter  $\beta(E, m_{\text{ion}})$  we can then calculate the expected residual energy of particles with

$$E = q_{\text{ion}}(E/q + V_{\text{PAC}}) \cdot \alpha(E, m_{\text{ion}}) \cdot \beta(E, m_{\text{ion}}) \quad (2.13)$$

A more elaborate discussion on the expected time-of-flight and residual energy with PLASTIC is given in *Dreus* [2009]. The resulting expected time-of-flight and residual energy positions for a sample of ions is shown in Figure 2.9.

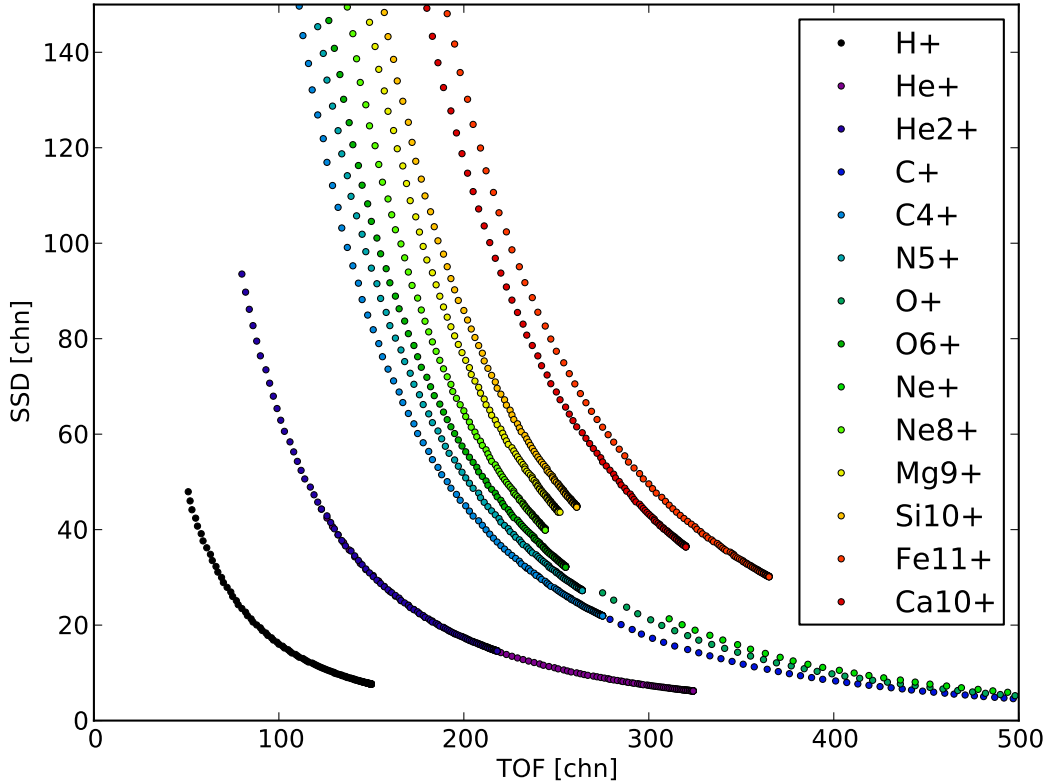


Figure 2.9.: Expected time-of-flight and residual energy positions for various solar wind and pickup ions at 128 instrumental energy-per-charge steps.

If we assume that the pickup  $\text{He}^+$  distribution does not overlap with adjacent distributions in  $\tau$ -space, we could allocate the available  $\text{He}^+$  data by a simple filtering method, also known as box-rate-method. Events that lie within a certain range of an ion's expected time-of-flight  $\tau_{\text{ion}}$  (and potentially residual energy  $E_{\text{ion}}$ ) would then be assigned to its respective species. Of course, the range must be chosen to reflect the actual uncertainty of the time-of-flight measurement to ensure that the data is not partially cropped by the applied filter. This requires an estimate of the expected time-of-flight uncertainty, which is primarily governed by

- the uncertainty of the energy loss  $dE/dx$  ( $\pm\Delta\tau$ )
- the uncertainty  $\Delta E/q = 6\%$  of the energy-per-charge measurement ( $\pm\Delta\tau$ )
- a variable carbon foil thickness or curvature ( $\pm\Delta\tau$ )
- the uncertainty of the start- and stop-trigger electronics ( $\pm\Delta\tau$ )
- angular scattering of ions passing through the carbon foil ( $+\Delta\tau$ ).

The first four items will create a deviation  $\Delta\tau$  of the expected time-of-flight that is either positive or negative, while the angular scattering due to passage of the thin carbon foil can only cause a positive  $\Delta\tau$ . However, all of these items can produce an asymmetric time-of-flight distribution as most of these effects don't scale linearly with  $\tau$ . Finding a suitable

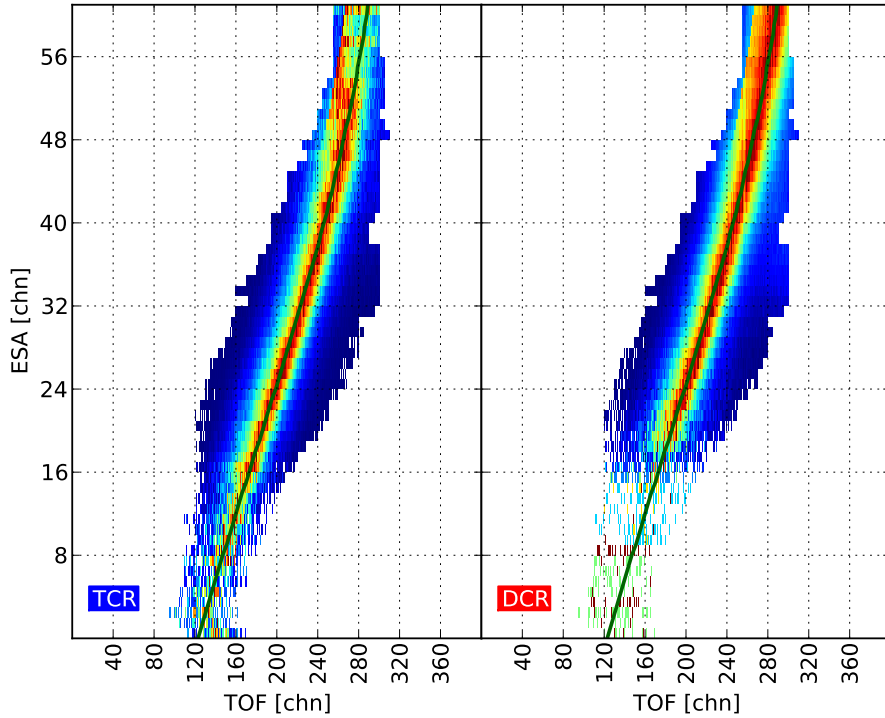


Figure 2.10.:  $\text{He}_{\text{TCR}}^+$ -box (left) and  $\text{He}_{\text{DCR}}^+$ -box (right) accumulated over a period of 100 days. The x-axes show time-of-flight channel and the y-axes energy-per-charge steps. The color coded intensity is normalized to 1 at each  $E/q_{\#}$ , where red denotes maximum intensity, blue minimum intensity, and white, areas where no counts were observed. The dark green line denotes the expected  $\tau$ -position of  $\text{He}^+$ . Within  $E/q_{1-60}$  the core of the  $\text{He}^+$  distribution is fully covered by our applied filter. At  $E/q_{>45}$  the  $\text{He}_{\text{TCR}}^+$  signal almost vanishes with respect to instrumental noise.  $\text{He}_{\text{DCR}}^+$ , on the other hand, shows a clear signal but also a  $\text{Fe}^{14+}$  induced background in this energy-per-charge regime. The background is visible in form of an increasingly distinct asymmetry towards small time-of-flights.

expression for the expected time-of-flight distributions is a very complex matter due to the variety of involved processes. In fact, most of them require a numerical simulation that is able to predict the behaviour of particles and secondary electrons in PLASTIC's time-of-flight chamber in order to give a profound estimate on the time-of-flight characteristics. For the moment, it is sufficient to assure that the  $\text{He}^+$ -box is neither partially cropped nor heavily polluted by a time-of-flight background. Without a detailed quantification of the time-of-flight characteristics, we can only assure a full coverage of the  $\text{He}^+$  distribution using a longterm data calibration. For that, a minimum and maximum  $\tau_{\#}$  and  $E_{\#}$  were manually chosen in the energy-per-charge range of  $E/q_{3-60}$ , that sufficiently covered the respective  $\text{He}^+$  distribution under consideration of spill-over counts by adjacent solar wind ions (see Figure 2.10). Spill-over, especially of  $\text{Fe}^{14+}$ , which has a very similar mass-per-charge, mainly occurs at  $E/q_{>45}$ . Almost all  $\text{Fe}^{14+}$  events have sufficient energy to trigger a residual energy signal and therefore primarily occur in form of TCR. Furthermore, they are well separated in terms of residual energy from  $\text{He}^+$  and don't produce any background in the  $\text{He}^+$ -box (see Figure 2.10, left panel). However,  $\text{Fe}_{\text{DCR}}^{14+}$ , despite being quite rare

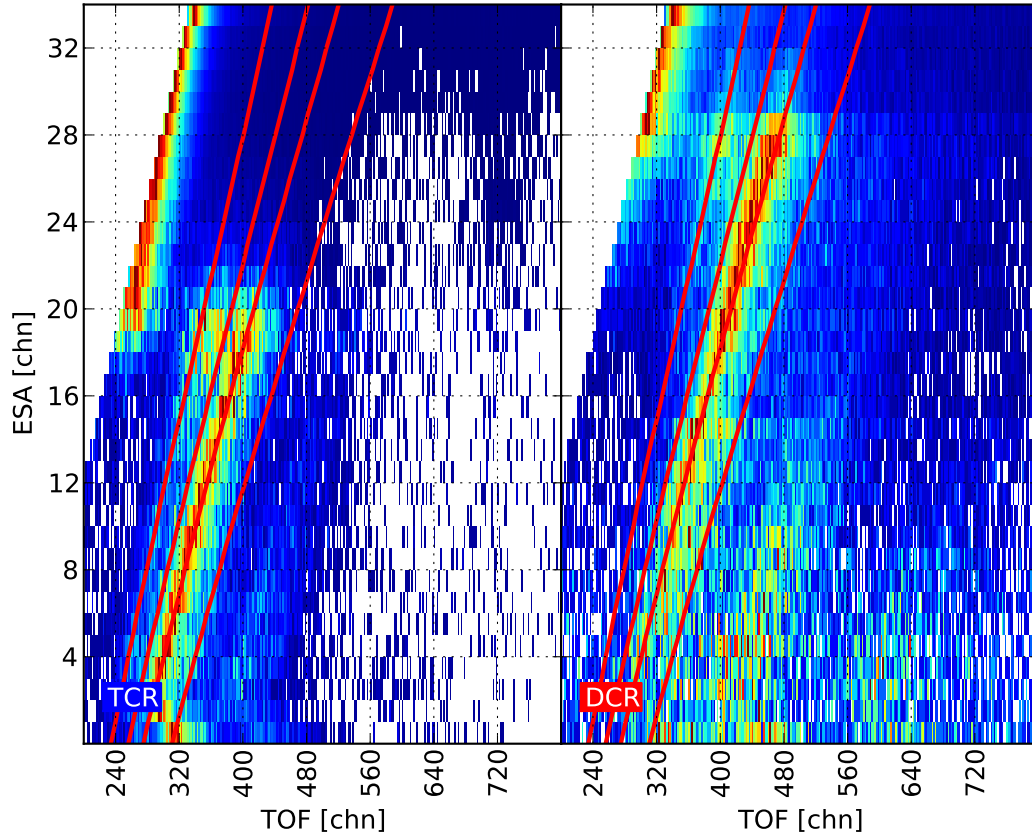


Figure 2.11.: TCR- and DCR-box of heavy pickup ions accumulated over a period of 1000 days. The x-axes show time-of-flight channel and the y-axes energy-per-charge steps. The color coded intensity is normalized to 1 at each  $E/q_{\#}$ , where red denotes maximum intensity, blue minimum intensity, and white, areas where no counts were observed. The red lines denote (from left to right) the expected  $\tau$ -position of  $C^+$ ,  $N^+$ ,  $O^+$ , and  $Ne^+$ .

compared to  $Fe_{TCR}^{14+}$ , is able to produce a significant background due to its similar mass-per-charge and the fact that it can't be separated in terms of residual energy. Because  $Fe^{14+}$  loses less energy per nucleon during its passage through the carbon foil, its expected time-of-flight is slightly smaller than that of  $He^+$ . As a result, the  $He_{DCR}^+$ -box shows with increasing  $E/q_{\#}$  an increasingly distinct asymmetry towards smaller time-of-flights induced by a  $Fe^{14+}$  background (see Figure 2.10, right panel).

For the acquisition of heavy pickup ion data it is not sufficient to apply a simple  $\tau/E$ -filter. Figure 2.11 shows the available pickup ion data accumulated over a period of 1000 days and clearly demonstrates that the  $C^+$ ,  $N^+$ ,  $O^+$ , and  $Ne^+$   $\tau$ -distributions overlap, which would cause a significant uncertainty of the respective box-rates. In section 3.2 our approach to separate the observed  $C^+$ ,  $N^+$ ,  $O^+$ , and  $Ne^+$  distributions from each other is discussed and compared to a simple box-rate method. However, we first need to collect the available data, which is achieved by a dynamic heavy pickup ion filter that, at an energy-per-charge range of  $E/q_{3-60}$ , allocates all events with a time-of-flight higher than the expected time-of-flight of  $C^+$  minus 100 channel. With that we can assure

to allocate only particles with a mass-per-charge value of at least  $\sim 9 \text{ amu}/e$  up to the maximum measurable mass-per-charge of PLASTIC. Because heavy pickup ions clearly dominate their respective mass-per-charge range, i.e. solar-wind ions are not expected to significantly contribute to the mass-per-charge range between  $12 \text{ amu}/e$  and  $24 \text{ amu}/e$ , it is not required to limit the heavy pickup ion data to TCR only. In fact, Figure 2.11 shows that heavy pickup ion DCRs can even be resolved up to  $\sim E/q_{32}$  while the TCRs seem to be polluted by an extended  $\tau$ -background at  $E/q_{>22}$  that has its maximum at low time-of-flights. This behaviour is quite contrary to what was observed for the  $\text{Fe}^{14+}$  induced background in the  $\text{He}^+$  box rate, where  $\text{He}_{\text{TCR}}^+$  was almost not affected by background. In the observed mass-per-charge range of pickup ions, however, the background is induced by  $\text{Fe}^{5+}$  ions.  $\text{Fe}^{5+}$  ions have due to their smaller mass-per-charge an expected time-of-flight that is clearly smaller than that of  $\text{C}^+$ . But it is also far more abundant than  $\text{C}^+$  and an asymmetry of its  $\tau$ -distribution towards higher time-of-flights can already produce enough spill-over to pollute the mass-per-charge range of heavy pickup ions. Furthermore, it deposits much less energy in the solid state detector than  $\text{Fe}^{14+}$  and as a consequence, its expected residual energy lies only slightly above that of  $\text{C}^+$ , which ultimately prevents us from separating them in terms of residual energy deposit. The  $\text{Fe}^{5+}$  induced background also affects the heavy pickup ion DCRs, but to a smaller extent and only at  $E/q_{>32}$  where the residual energy deposit of  $\text{Fe}^{5+}$  is not sufficient to trigger an energy signal anymore.

Although DCRs generally provide a more promising approach for an analysis of heavy pickup ion data (see Figure 2.11), our observation of the neon focusing cone (see chapter 3.2) was performed using only heavy pickup ion TCRs in the energy-per-charge range of  $E/q_{3-28}$ . This decision was made under the impression that TCRs would provide a better signal-to-noise ratio and to preserve comparability of the applied  $\text{He}^+$  and heavy pickup ion filters. However, later studies have shown that adding DCRs to our analysis can not only enhance the overall statistics and quality of our data (see chapter 4) but also greatly extend the observable energy-per-charge range of pickup ions.



## 3. Observations of the Neon Focusing Cone

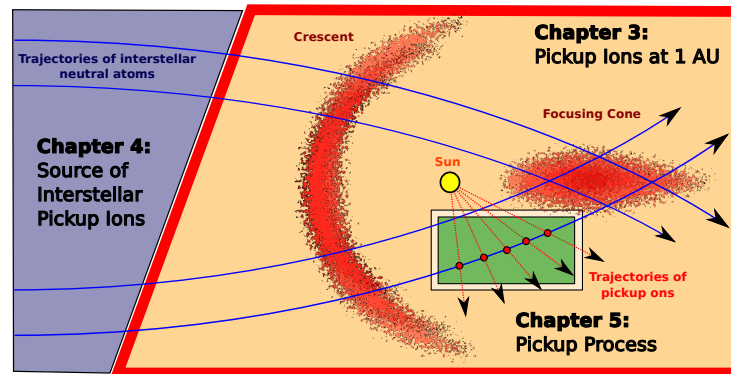


Figure 3.1.: This chapter addresses the spatial distribution of pickup ion at 1 AU (yellow shaded area). Hereby we will especially address the formation of the neon focusing cone.

### 3.1. Introduction

#### Chapter Overview

This chapter covers our first publication "Observations of interstellar neon in the helium focusing cone" [Drewns *et al.*, 2010], which was published in October 2010 in the Journal of Geophysical Research, Vol 115. The publication was supervised by Dr. Lars Berger and Prof. Robert Wimmer-Schweingruber, who were involved in all scientific discussions and added greatly to the overall quality of the publication. The remaining co-authors, namely Antoinette B. Galvin, Berndt Klecker, and Eberhard Möbius assisted in form of fruitful discussions about our results and technical issues regarding PLASTIC. The 1<sup>st</sup> author, Christian Drewns, has contributed  $\sim 75\%$  of the performed study. In section 3.2 our publication [Drewns *et al.*, 2010] is presented. Section 3.3.1 contains supplementary material covering a comparison between the proposed Poisson analysis and a common box rate method for species classification.

#### Abstract of Publication

"Using the large geometric factor of the Plasma and Suprathermal Ion Composition instrument on the Solar Terrestrial Relations Observatory mission, we have studied heavy pickup ions in the mass-per-charge range 12-20 during 2007 and 2008. We have clearly identified  $C^+$ ,  $N^+$ ,  $O^+$ , the  $H_2O^+$  group, and  $Ne^+$  among the heavy pickup ions. Out of these,  $Ne^+$  shows clear enhancements during two consecutive focusing cone passages, as evidenced by concurrent  $He^+$  enhancements during these periods, whereas all the other species are evenly distributed. This is the first observation of the interstellar focusing

### 3.2. PUBLICATION

---

cone for Ne, whose survival probability as neutrals is only slightly lower than that of He and substantially higher than for other elements” (from *Dreus et al.* [2010]).

### 3.2. Publication

## Observations of interstellar neon in the helium focusing cone

Christian Drews,<sup>1</sup> Lars Berger,<sup>1</sup> Robert F. Wimmer-Schweingruber,<sup>1</sup>  
Antoinette B. Galvin,<sup>2</sup> Berndt Klecker,<sup>3</sup> and Eberhard Möbius<sup>2</sup>

Received 20 April 2010; revised 28 June 2010; accepted 29 July 2010; published 19 October 2010.

[1] Extended pickup ion distributions in the heliosphere have been found to originate either from interstellar neutral gas or from the so-called inner source. Because of the motion of the Sun through the interstellar medium, interstellar neutral gas flows through the inner heliosphere and for some of the species is focused on the downwind side by the gravitation of the Sun. This gravitational focusing cone, which is absent for inner source ions, has been identified for He with UV backscattering and pickup ion observations and is used to diagnose the interstellar parameters. Using the large geometric factor of the Plasma and Suprathermal Ion Composition instrument on the Solar Terrestrial Relations Observatory mission, we have studied heavy pickup ions in the mass-per-charge range 12–20 during 2007 and 2008. We have clearly identified C<sup>+</sup>, N<sup>+</sup>, O<sup>+</sup>, the H<sub>2</sub>O<sup>+</sup> group, and Ne<sup>+</sup> among the heavy pickup ions. Out of these, Ne<sup>+</sup> shows clear enhancements during two consecutive focusing cone passages, as evidenced by concurrent He<sup>+</sup> enhancements during these periods, whereas all the other species are evenly distributed. This is the first observation of the interstellar focusing cone for Ne, whose survival probability as neutrals is only slightly lower than that of He and substantially higher than for other elements.

**Citation:** Drews, C., L. Berger, R. F. Wimmer-Schweingruber, A. B. Galvin, B. Klecker, and E. Möbius (2010), Observations of interstellar neon in the helium focusing cone, *J. Geophys. Res.*, 115, A10108, doi:10.1029/2010JA015585.

### 1. Introduction

[2] Because of the Sun's motion relative to the surrounding interstellar medium interstellar atoms with high first ionization potential penetrate deeply into the inner heliosphere as an interstellar wind [e.g., Fahr, 1974]. These atoms enter the heliosphere unimpeded by the heliospheric magnetic field. Once close to the Sun, they are ionized, picked up by the combined forces of the interplanetary magnetic and the motional electric field of the solar wind, and can then be observed as Pickup Ions (PIs) [e.g., Möbius *et al.*, 1985; Gloeckler *et al.*, 1998]. Because of the low relative speed between heliosphere and the local interstellar medium, the trajectories of atoms are gravitationally focused on the downwind side of the Sun, thus leading to a substantial density enhancement in the neutral gas distribution, termed the focusing cone [Fahr, 1974], for all interstellar neutral species except for hydrogen for which solar radiation pressure compensates for gravitation. The focusing cone has been observed for He using resonant backscattering of solar ultra-

violet (UV) light [Paresce *et al.*, 1974; Weller and Meier, 1974] and pickup ions [e.g., Möbius *et al.*, 1995; Gloeckler *et al.*, 2004]. Combined observations of the He focusing cone with UV backscattering techniques [Lallement *et al.*, 2004] and pickup ions [Gloeckler *et al.*, 2004], and direct neutral gas flow measurements [Witte, 2004] were used to derive a consolidated set of interstellar gas parameters for interstellar helium [Möbius *et al.*, 2004]. So far, a focusing cone has not been observed for any other interstellar gas species.

[3] In addition to interstellar pickup ions the generation of pickup ions from dust in the inner heliosphere was discussed by Fahr *et al.* [1981]. First observations of singly charged heavy ions ( $m > 4$  amu) with a velocity distribution that points to a source close to the Sun, hence inner source, were reported by Geiss *et al.* [1995]. With abundances similar to but still distinct from those of the solar wind [Gloeckler and Geiss, 1998; Gloeckler *et al.*, 2000], these ions have been interpreted as solar wind absorbed by dust particles close to the Sun and then reemitted as atoms or singly charged ions [Schwadron *et al.*, 2000], with a peak production between about 10 and 20 solar radii from the Sun. The process of reemission is unclear, and alternate production models have been suggested. Wimmer-Schweingruber and Bochsler [2003] proposed the penetration of solar wind through small dust grains and related charge exchange, Bzowski and Krolkowska [2004] suggested Sun-grazing comets as a potential source, and Mann and Czechowski [2005] studied the collisional breakup of dust in the inner heliosphere. Each scenario has

<sup>1</sup>Institute for Experimental and Applied Physics, Christian-Albrechts-University zu Kiel, Kiel, Germany.

<sup>2</sup>Space Science Center and Department of Physics, University of New Hampshire, Durham, New Hampshire, USA.

<sup>3</sup>Institute for Extraterrestrial Physics, Max-Planck Institute, Garching, Germany.

**Table 1.** Expected  $m/q$  Bins After Energy Loss in Carbon Together With  $\Delta m/q$ , Which Denotes the Absolute Uncertainties of our Calculation

Ion	$m/q$ (u/e)	$\Delta m/q$ (u/e)
C <sup>+</sup>	12.06	0.18
N <sup>+</sup>	14.15	0.27
O <sup>+</sup>	16.24	0.35
H <sub>2</sub> O <sup>+</sup>	18.41	0.41
Ne <sup>+</sup>	20.42	0.44

different consequences for the pickup ion abundances and velocity distributions.

[4] In this paper, we report on observations of heavy pickup ions in the mass range of 12–20 amu taken with the Plasma and Suprathermal Ion Composition (PLASTIC) instrument on the Solar Terrestrial Relations Observatory (STEREO) A during 2007 and 2008. We show that a mixture of C<sup>+</sup>, N<sup>+</sup>, O<sup>+</sup>, and the H<sub>2</sub>O<sup>+</sup> group, with maximum abundance of O, is most likely contributed to the inner source, while the majority of the observed Ne<sup>+</sup> is identified as interstellar because it shows a distinct focusing cone structure collocated with the He<sup>+</sup> focusing cone.

## 2. Instrumentation and Data Analysis

[5] Here, we report observations of PUIs with the PLASTIC instrument [Galvin *et al.*, 2008] on the STEREO [Kaiser *et al.*, 2008] mission. STEREO consists of two spacecraft, A and B, one moving Ahead (A) of the Earth, and one Behind (B) at an angle increasing by roughly 22° per year. PLASTIC is a time-of-flight mass spectrometer which, by a combination of electrostatic deflection, time of flight and total energy measurement, measures the kinetic energy, mass, and charge of heliospheric ions. It has a large geometric factor which makes it especially well-suited for the investigation of rare heavy pickup ions. For our analysis we used the Solar Wind Section (SWS) of PLASTIC which provides a field of view of 45° in the ecliptic and ±20° in the polar direction, and is centered on the Sun-Earth line.

[6] Until 2010 the Sun has been in an unusually prolonged state of low activity, resulting in a very simple structure of the inner heliosphere dominated by the interaction of high-speed streams from coronal holes and slow solar wind. Since early 2007, we have been observing a more or less regularly recurring pattern of alternating high-speed streams and slow wind. This period is ideal for our studies of inner-source and interstellar PUIs because it is nearly entirely free of Interplanetary Coronal Mass Ejections (ICMEs) which show occasional enhancements of low-charge states of heavy ions [e.g., Gloeckler *et al.*, 1999]. Indeed, only 11 ICMEs were observed in situ at STEREO A from January 2007 to March 2009 which ensures a very clean interplanetary background for observing PUIs.

[7] We used PLASTIC Pulse Height Analysis (PHA) words to determine the energy, mass, and mass-to-charge ratio of heavy pickup ions, mainly C<sup>+</sup>, N<sup>+</sup>, O<sup>+</sup>, the H<sub>2</sub>O<sup>+</sup> group and Ne<sup>+</sup>, as well as heavier ions, such as Mg<sup>+</sup>, Si<sup>+</sup>, S<sup>+</sup>. The PHA words provide the full measurement information, energy-per-charge,  $E/q$ , time of flight,  $\tau$ , and residual energy,  $E_{res}$ , measured in the solid-state detectors [Galvin *et al.*, 2008].

As PLASTIC steps down through its  $E/q$  range beginning at  $E/q \sim 80$  keV/e, heavy pickup ions are well separated from the solar wind because of their single charge and the fact that all ions in the solar wind flow at roughly the same speed. Because pickup ions can exceed the solar wind velocity within a factor of two we had to account for PLASTIC's maximum  $E/q$  step of  $\sim 80$  keV/e, that can cause velocity spectra of the heavier PUIs to be cut off. Especially spectra of Ne<sup>+</sup>, that is covered by PLASTIC's energy range up to a velocity of  $\sim 900$  km/s, are not fully covered by the instrument when solar wind velocities exceed 450 km/s. We therefore calculated in each temporal bin  $w_{max} = v_{Ne_{max}^+}/v_{SW}$  that constitutes the maximum  $w = v_{ion}/v_{SW}$  for which Ne<sup>+</sup> can be detected. In addition  $w_{min} = v_{Ne_{min}^+}/v_{SW}$  is derived, that constitutes the smallest  $w$  in which Ne<sup>+</sup> exceeds the solid-state detector threshold. Events of the remaining pickup species are then only taken into account for our investigation if their  $w = v_{ion}/v_{SW}$  was below  $w_{max}$  and above  $w_{min}$ . We are then able to compare different PUI species to each other despite their different coverage in velocity space. Because pickup ions are rare, we have limited ourselves to a time resolution of 1 h or longer.

[8] Figure 1 demonstrates that different species of heavy pickup ions can be identified, especially Neon and Helium (not shown), upon which this work is based. The  $m/q$  classification is based on the time-of-flight measurement which in turn is sensitive to the energy lost in the thin carbon foil used in PLASTIC to trigger the start signal of the time-of-flight measurement. To predict the observed  $m/q$  bin of different heavy PUI species, we simulated the species- and energy-dependent energy loss,  $\alpha(E, m)$ , in PLASTIC's carbon foil for C<sup>+</sup>, N<sup>+</sup>, O<sup>+</sup>, H<sub>2</sub>O<sup>+</sup>, and Ne<sup>+</sup> and calculated the resulting mass-per-charge with equation (1),

$$\frac{m}{q} = 2(E/e + V_{PAC})\alpha(E, m)\left(\frac{\tau}{d}\right)^2, \quad (1)$$

where  $d$  denotes the flight path of ions in the instrument and  $V_{PAC}$  the post acceleration voltage. Results are presented in Table 1.

[9] The long-term  $m/q$  spectrum of Figure 1, which was collected in a period of 900 days beginning in February 2007, is modeled by a combination of five Gaussians using the derived  $m/q$  values from Table 1 as the center of density. The Gaussians' sigmas are set and kept fixed to 0.91 and constitute values that are able to reproduce the long-term  $m/q$  spectrum seen in Figure 1. The intensities of the Gaussians are determined by a fit to the data. The resulting model is shown in Figure 1 (black dashed line) and shows for  $m/q < 23$  no distinct deviations from the data, which implies that our assumed sigma is a good approximation. Events of  $m/q > 23$ , which indicate possible contributions from Mg<sup>+</sup>, Si<sup>+</sup>, CO<sup>+</sup>, Fe<sup>2+,3+</sup>, are disregarded for further studies due to their very low abundance relative to the already low abundance of the five major contributions of heavy PUIs.

[10] We have to note that contributions to a PUI long-term  $m/q$  spectrum by molecules at 1 AU have not been investigated yet. Our assumption that solely singly charged water molecules contribute to the observed enhancement between

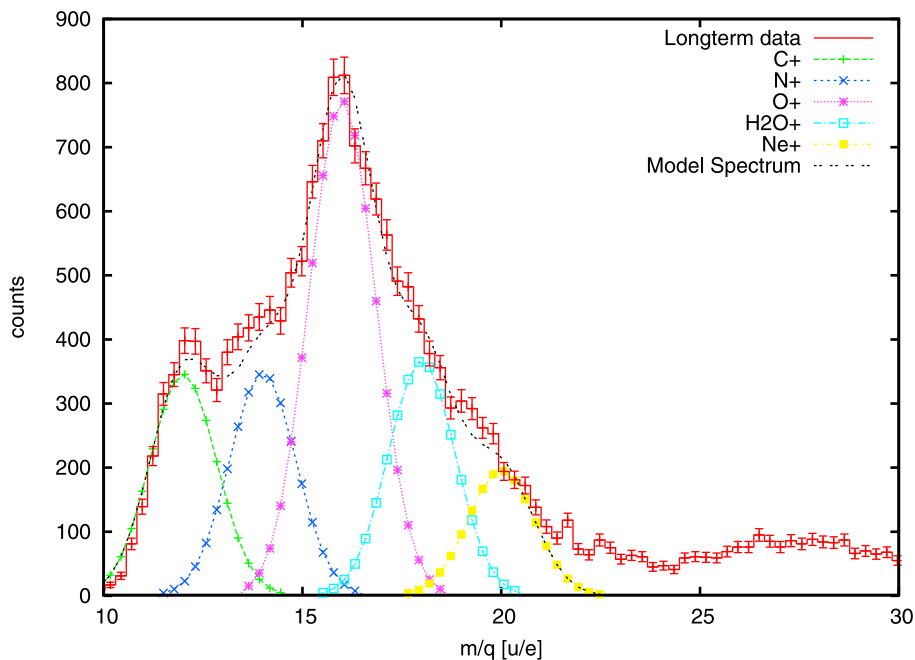


**Figure 1.** Mass-per-charge ( $m/q$ ) spectrum of heavy pickup ions measured with PLASTIC’s solar wind section (SWS) on STEREO A during a period of 900 days. The data were collected in a solar wind velocity range of 316–616 km/s and sorted into  $m/q$  bins of 0.33 amu/e width. Contributions of  $C^+$ ,  $N^+$ ,  $O^+$ , the  $H_2O^+$  group, and  $Ne^+$  (colored curves) are determined by a simultaneous fit of five Gaussians with the peak heights as free parameters. The resulting model spectrum (black dashed line) is a direct indicator for the quality of the assumed model and shows no significant deviation from the long-term data.

mass-per-charges of 18 amu/e to 20 amu/e is likely a simplification. Investigations of PUIs made with the SWICS instrument onboard Ulysses [Gloeckler and Geiss, 2001] have shown that also  $OH^+$  or  $H_3O^+$  may contribute to the observed count rates. We chose to disregard contributions by these molecules in our analysis because they show up in a very narrow  $m/q$  range between 18 amu/e and 20 amu/e and are difficult to resolve. Therefore, derived count rates of water group molecules can only be seen as an upper limit of the  $H_2O^+$  abundance.

[11] The derived sigma, center of density, and intensity of the five major  $m/q$  peaks can now be used to evaluate the counts for each of the five major ion species separately despite their strong overlap in  $m/q$  space. The algorithm used to derive the Gaussian intensities for a long-term  $m/q$  spectrum is a Levenberg-Marquardt algorithm [Press et al., 1999] that uses a standard  $\chi^2$  Maximum Likelihood Estimator (MLE) to determine the likelihood of model  $y(x_i, \vec{a})$  being related to the normally distributed data samples  $y_i$ . A description of the algorithm, that is used for resolving the heavy PUI species for shorter time periods (<24 h) is given in Appendix A.

[12] In Figure 2 we present a time series of hourly count rates of heavy PUIs with  $m/q < 23$  in a period of 15 days, that were collected with PLASTIC onboard STEREO A. A strong correlation with the solar wind velocity, caused by the energy and species dependent detection probability (efficiency) can be seen. In fast solar wind streams, ions have a higher kinetic energy and thus have a higher chance of triggering a valid event. In slow solar wind streams the probability of triggering a valid event decreases propor-

tionally to the particle’s mass and energy. This systematic effect introduces a bias into our measurements that could be corrected for by applying an efficiency function that is available for several ions based on preflight beam calibrations. However, in actual flight conditions, we must also compensate for the aging of the Micro Channel Plates (MCP) that leads to a decrease in detection efficiency for the time-of-flight measurements. This decrease is partially compensated for by adjusting the MCP bias voltage periodically, and this makes the overall efficiency function time-dependent and complicated. We therefore pursue the approach discussed below for the corrections. Apart from the velocity correlation one also notices an enrichment of counts at the leading edges of high-speed streams, which is most likely caused by the compression of the solar wind (see days 367 and 372 in Figure 2) and has recently been discussed in connection with the  $He^+$  focusing cone observations using STEREO PLASTIC [Möbius et al., 2010].

[13] The large variability of count rates seen in Figure 2 is the result of two effects. On the one hand, as already alluded to, the probability to trigger a valid event depends on the velocity of the ion. On the other hand, within one single temporal bin, many different solar wind speeds have likely been sampled. If we consider longer time bins, we can remove part of the velocity dependence by giving every velocity bin an equal weight. This can be done even if we do not know the exact velocity or energy dependence of the detection efficiency. As mentioned in Appendix A averaging hourly count rates over periods >24 h will also decrease

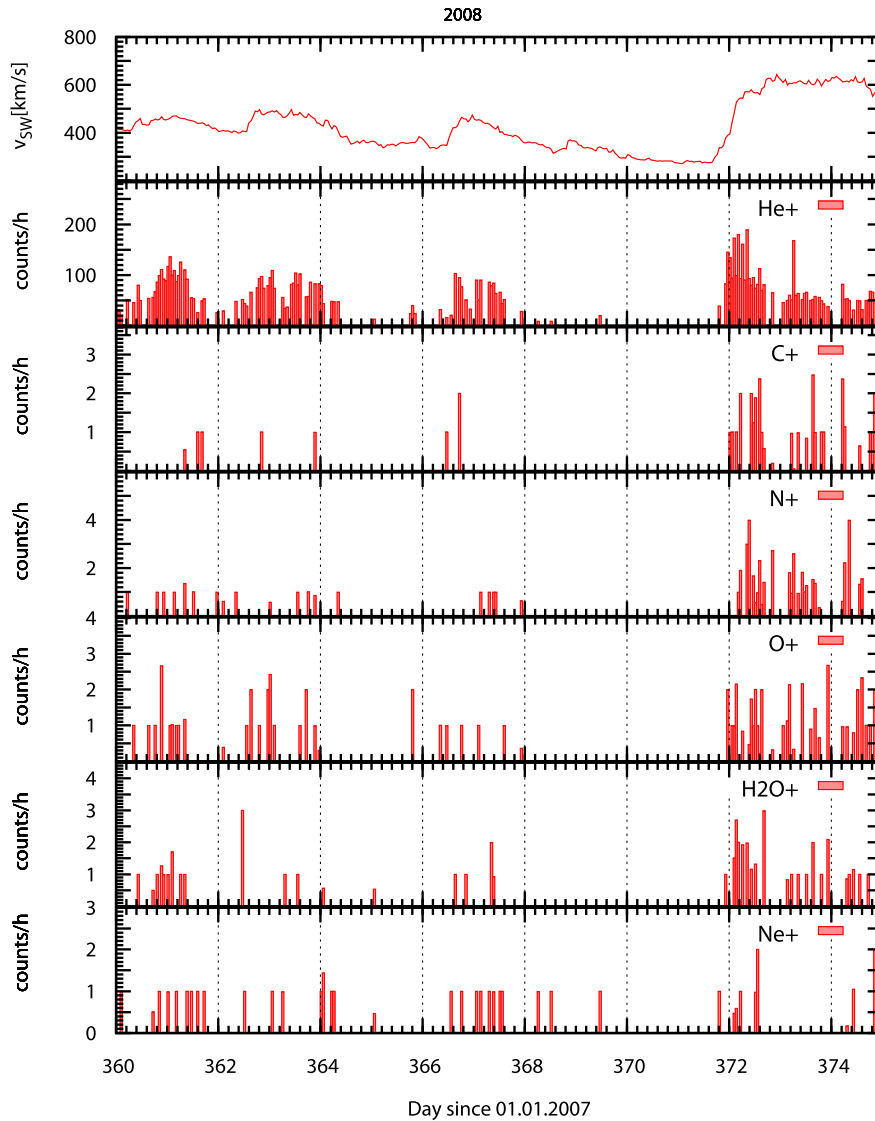


**Figure 2.** A time series of hourly count rates of  $\text{He}^+$ ,  $\text{C}^+$ ,  $\text{N}^+$ ,  $\text{O}^+$ , the  $\text{H}_2\text{O}^+$  group, and  $\text{Ne}^+$  is shown. (top) The corresponding proton bulk velocity. Count rates are strongly correlated with solar wind speed, as no efficiency correction has been applied.

the uncertainties in the abundance that are deduced from our fit (see Figure A1).

[14] Therefore, we consider, from now on, only long-term averages and bin all quantities into 27 day temporal bins. Within one 27 day bin, we consider hourly values for the pickup ion count rates our basic data product and divide the solar wind velocity range  $316 \text{ km/s} < v < 616 \text{ km/s}$  into 6 velocity bins, each 50 km/s wide. We now count how often every velocity bin occurs and call that number  $N_{v,tb}$ , where  $t_b$  is the time of the temporal (27 day) bin. In each velocity bin, we also count the number of pickup ions measured,  $C_{v,tb}$ . In order to be able to compare the results from time bin  $b$  with those in time bin  $b + 1$ , we need to ensure that all velocity bins have the same weight. Therefore, we sum the ratio of pickup ion counts per velocity bin,  $C_{v,t}$ , with the number of occurrences of that bin,  $N_{v,tb}$  and

divide it by the length of the temporal bin,  $t_w$ , expressed in hours. This then gives us a smoothed value for the hourly count rate,

$$\bar{C}_{t_b} = \sum_{t=t_b}^{t_b+t_w} \sum_v \frac{C_{v,t}}{N_{v,tb} t_w}. \quad (2)$$

The  $v_{SW}$  window of 316–616 km/s assures every velocity bin to occur at least once per time bin  $t_b$ , so that  $N_{v,tb} > 0$ . The length of the time bin,  $t_w$  is determined by some typical time scale, in our case, the solar rotation with  $t_w = 27$  days. Choosing one solar rotation as the time bin width should remove most of the remaining velocity dependence because of the quasi-regular recurrence of high-speed streams and slow wind in this unique period of solar activity. Note that this is not really the rotation period at STEREO A, where it

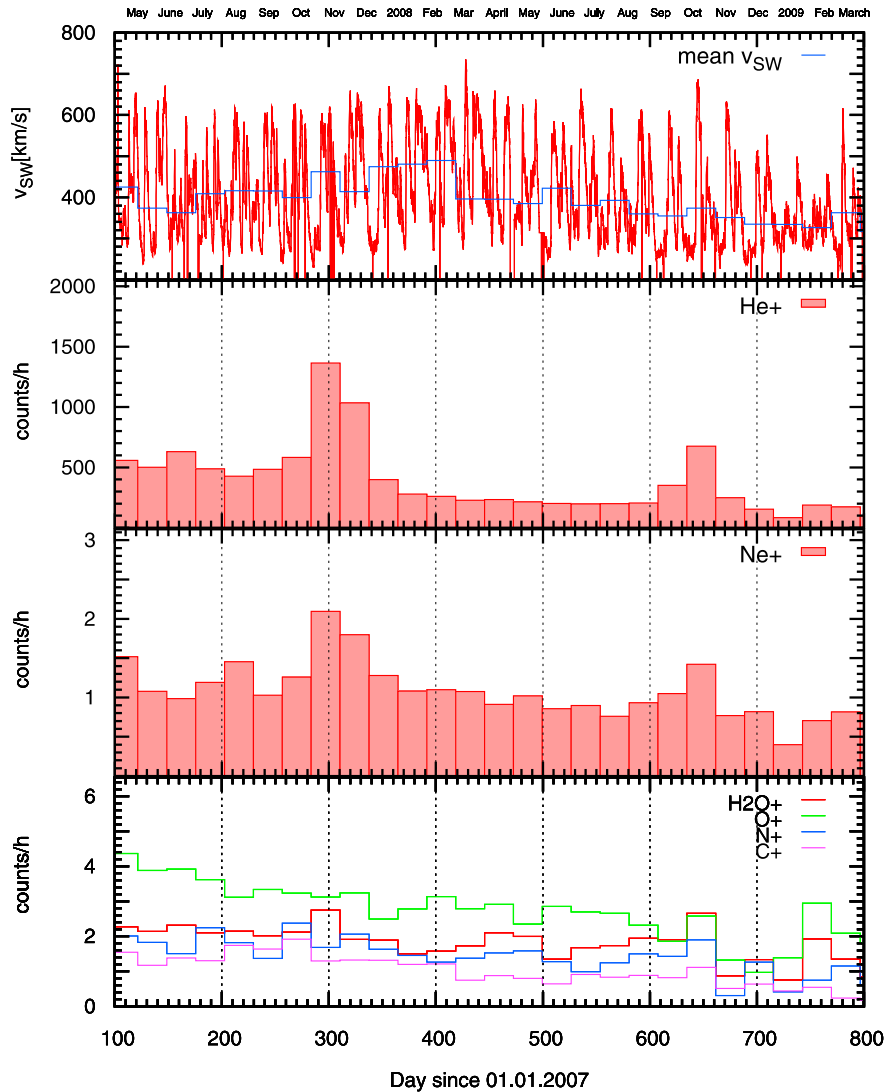


**Figure 3.** Mean PUI count rates of STEREO A in a period of 700 days. Counts are binned over 27 days and normalized to a constant occurrence of velocity bins with a width of 50 km/s (consult text for details on the binning procedure). The second and third panels from the top show time series of mean count rates of  $\text{He}^+$  and  $\text{Ne}^+$ . (bottom) Time series of the remaining heavy PUI species. (top) The corresponding proton bulk velocity.

would be  $\sim 28$  days, neither is it that of STEREO B where it would be about  $\sim 26$  days, but the average of the two, which also coincides with the synodic rotation period. This choice assures that in the future we can compare our data with observations from STEREO B or ACE and SOHO.

### 3. Data Interpretation

[15] We are now able to create time series of pickup ion count rates for  $\text{He}^+$ ,  $\text{C}^+$ ,  $\text{N}^+$ ,  $\text{O}^+$ , the  $\text{H}_2\text{O}^+$  group, and  $\text{Ne}^+$  that are not affected by the already mentioned detection-efficiency-related correlation of count rates with the solar wind speed. We have to note that, using equation (2), it is not possible to derive PUI ratios from pickup ion count rates.

A discussion of PUI ratios would require precise knowledge of the efficiency functions of heavy PUIs.

[16] Figure 3 shows count rates of heavy PUIs in a time period beginning in May 2007 and ending in March 2009 using the binning procedure given by equation (2) and discussed above. We see the helium cone traversal around days 310 and 640 with an approximate half width of 54 days that reflects the chosen bin width of 27 days. By calculating the weighted mean of the two enhanced and its two neighboring time bins we are able to give an estimate for the interstellar wind flow direction in ecliptic longitude of  $\lambda \approx 66^\circ \pm 27^\circ$ , that is in rough agreement with values from *Gloeckler et al.* [2004], who derived a direction of  $\lambda = 74.6^\circ$ . The He focusing cone appears to be more pronounced on day 310 than on the second passage around day 640.

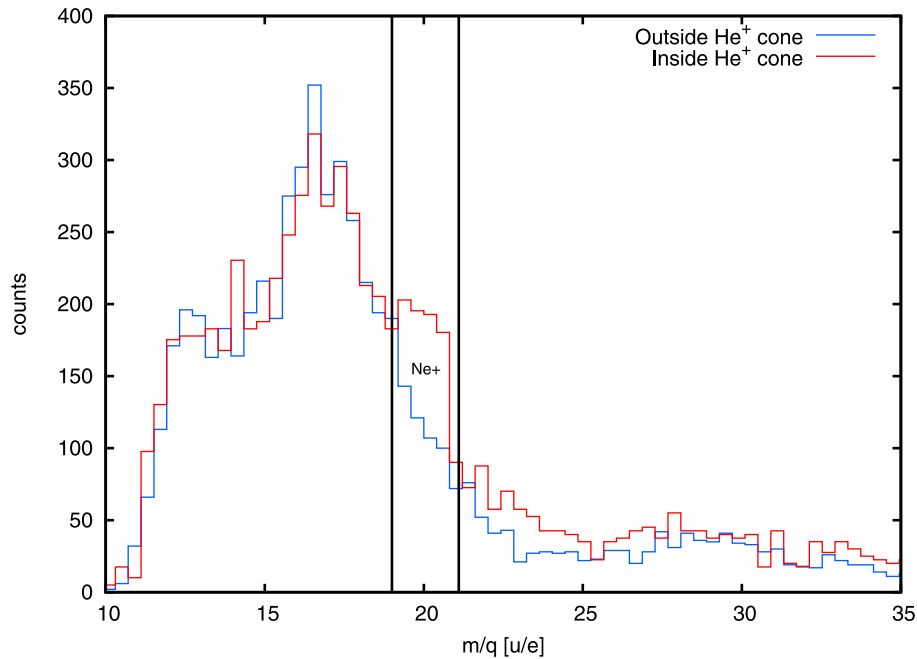


**Figure 4.** Mass-per-charge spectra of heavy pickup ions in two different time periods, one within focusing cone passage (red) and one outside (blue). In both spectra, velocity bins below 316 km/s and above 616 km/s are excluded. The inside spectrum is normalized to the intensity of the outside spectrum by multiplying a constant factor of 2.43 (consult text for details).

However, this is most likely an effect of changes in the instrument gain due to Micro Channel Plate (MCP) aging, which is only partially mitigated by adjustments of the MCP bias voltage. While this is important for detailed studies, this apparent change in the intensity of the focusing will not influence our findings detailed below.

[17] Aligned with the  $\text{He}^+$  enhancements we also observe a distinct increase of  $\text{Ne}^+$  counts. The  $\text{H}_2\text{O}^+$  group shows a slight enhancement along with  $\text{Ne}^+$  and will be discussed in detail below. During the first Helium cone traversal no recognizable enrichment is visible for the remaining heavy PUIs. During the second cone passage only a very small increase is present in one time bin which is led and followed by a decrease in the count rates. This is most likely an artifact of our binning procedure possibly due to a coincidence of rare velocity bins or an enhanced averaged solar wind velocity (compare Figure 3 (top)). For the  $\text{H}_2\text{O}^+$  group on the other hand two enrichments are observed that both constitute the highest count rate during the whole period. Although we cannot fully exclude the possibility that these enhancements are real, we have to point out that our fitting procedure can be responsible for the observed behavior of the  $\text{H}_2\text{O}^+$  group abundance. Our fit for the classification of the PUI species (compare equation (A5)) can misassign events that have occurred in the narrow mass-per-charge range between the  $\text{H}_2\text{O}^+$  group and  $\text{Ne}^+$ . Thus, events of  $\text{Ne}^+$  during cone passages with  $m/q < 20$  can be responsible for the observed enrichment as they can also be attributed to  $\text{H}_2\text{O}^+$  group in small fractions.

[18] If we keep in mind that Helium and Neon have a high First Ionization Potential (FIP) compared to other PUI species it is evident that they could originate from the same

source region, the interstellar medium. Although the depletion of interstellar neutral Neon ( $\text{FIP}_{\text{Ne}} = 21.6$  eV) at 1 AU by solar radiation is stronger than for interstellar neutral Helium ( $\text{FIP}_{\text{He}} = 24.6$  eV), their similar FIP still allows an enhancement as shown in Figure 3 to be produced by the focusing effect of interstellar Neon atoms.

[19] In order to verify our findings, we also investigated  $m/q$  spectra inside and outside passage of the Helium cone. Here, we are not able to quantify the enrichment found during cone passages, as both passages occurred during different averaged detection efficiencies. Instead we can present evidence that the observed enrichment is not produced by an uncertainty of our species classification nor is solely a result of our binning procedure. This is shown in Figure 4, where a  $m/q$  spectrum inside both focusing cones ([300:354, 640:694] days) is compared to a spectrum outside both cones ([200:308, 500:608] days). The inside spectrum is normalized to the intensity of the outside spectrum by multiplying a constant factor of  $\phi = 2.43$ , so that we can compare the two different time lengths. The factor was determined by a fit with an absolute uncertainty of 0.08. For the fit the mass-per-charge range of Neon ( $19 < m/q < 21$ ) has been excluded. The expected enhancement due to focusing of interstellar neon, as already shown in Figure 3, is clearly visible.

[20] In Figure 5 we give an estimate on the significance of this enhancement. It shows the difference between both  $m/q$  spectra of Figure 4 together with an error that is produced by the statistical uncertainty in counts and the uncertainty of the parameter  $\phi$ . In the given  $m/q$  range  $\text{Ne}^+$  is the only ion that shows a clear deviation between an inside- and outside-cone  $m/q$  spectrum. We have to note that the thus well resolved  $\text{Ne}^+$  peak of Figure 5 in mass-per-charge space (black line)



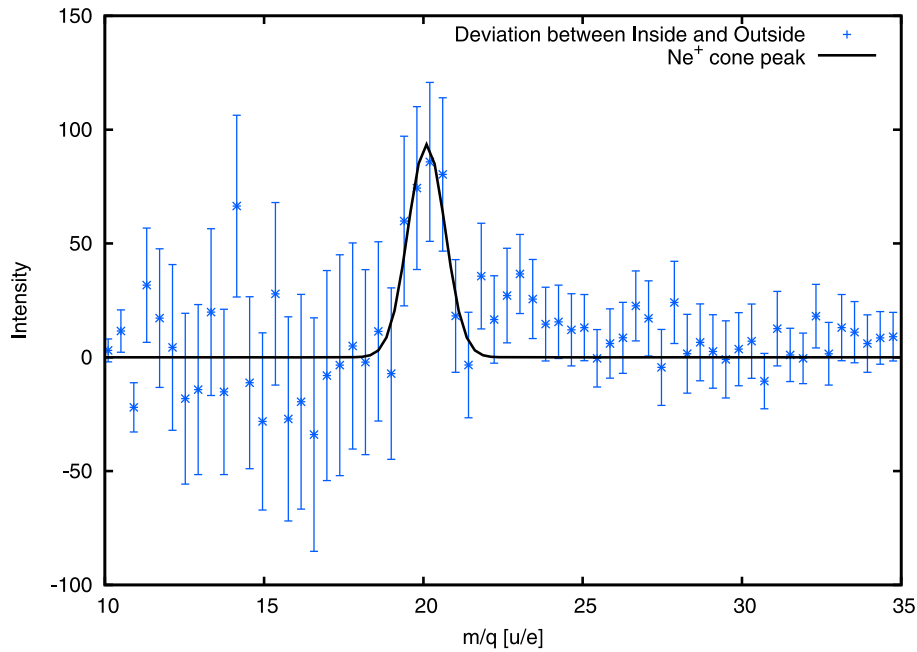


**Figure 5.** Difference between  $m/q$  spectra of heavy PUIs inside and outside the helium focusing cone.

is also in good agreement with our previously expected model for  $\text{Ne}^+$  of Figure 1.

#### 4. Discussion and Conclusions

[21] Using data from the PLASTIC instrument aboard STEREO A, we have observed enhancements of the count rate in  $\text{He}^+$  during passage of the so-called focusing cone. It is generally believed that these enhancements are due to the gravitational focusing of interstellar helium on its passage through the heliosphere. The thus enhanced neutral He density results in an enhanced production rate of pickup  $\text{He}^+$  which can be and has been observed [Möbius *et al.*, 1985; Gloeckler *et al.*, 2004].

[22] Coincident with these enhancements in  $\text{He}^+$ , we have also observed enhancements of singly charged neon ions. Considering the chosen velocity window of our  $m/q$  spectrum that excludes “rare” velocity bins and an accumulation time of at least one solar rotation per time period, we point out that an enrichment, as seen in Figures 3 and 4, cannot be caused by an efficiency related effect. Also contributions to the observed neon peak by adjacent PUI distribution are small due to the almost constant background of PUI counts. Thus, we conclude that the observed enhancement of neon, most likely caused by the gravitational focusing of interstellar neutral neon, is real and marks the first observation of this kind.

[23] We also note that enhancements of pickup carbon, nitrogen, and oxygen ions during cone passages are not observed. In fact, interstellar carbon ( $\text{FIP}_C = 11.3$  eV), nitrogen ( $\text{FIP}_N = 14.5$  eV), and oxygen ( $\text{FIP}_O = 13.6$  eV) are ionized much farther out in the heliosphere than helium and neon because of their higher ionization probability. Their abundance inside one AU is depleted by two orders of magnitude. Therefore, interstellar C, N, and O are likely not

responsible for the observed count rates of these species, and probably the inner source contributes most of them.

#### Appendix A: Maximum Likelihood Estimator Based on Poissonian Statistics

[24] Maximum likelihood fitting is a common tool in data analysis. The concept of this technique is to find a Maximum Likelihood Estimator (MLE)  $E_{y_i, x_i, \sigma_i}(\vec{a})$  that depending on a set of parameters  $\vec{a}$  describes the probability that a given set of measurements  $y_i, x_i, \sigma_i$  emanates from a model  $y(x_i, \vec{a})$ . The task of finding the best set of parameters  $\vec{a}_{\text{max}}$  is solved by finding the extremal value of  $E_{y_i, x_i, \sigma_i}(\vec{a})$ . The most common used MLE is the so-called  $\chi^2$  MLE. It assumes that the measuring inaccuracy is governed by Gaussian statistics. The likelihood that a set of measurements results from the model then can be written as

$$P_M^G(\vec{a}) = \prod_{i=1}^N \frac{1}{\sqrt{2\pi}\sigma_i} \exp -\frac{(y_i - y(x_i, \vec{a}))^2}{2\sigma_i^2}, \quad (\text{A1})$$

where the index  $M$  denotes the set of measurements and model  $y_i, x_i, \sigma_i, y(x_i, \vec{a})$ . For computational reasons instead of maximizing  $P_M^G(\vec{a})$

$$-\ln P_M^G(\vec{a}) = \sum_{i=1}^N \frac{(y_i - y(x_i, \vec{a}))^2}{2\sigma_i^2} - \sum_{i=1}^N \ln \frac{1}{\sqrt{2\pi}\sigma_i} \quad (\text{A2})$$

is minimized. With the second sum being constant we get

$$\chi^2 = \sum_{i=1}^N \frac{(y_i - y(x_i, \vec{a}))^2}{2\sigma_i^2} \quad (\text{A3})$$

as a MLE.

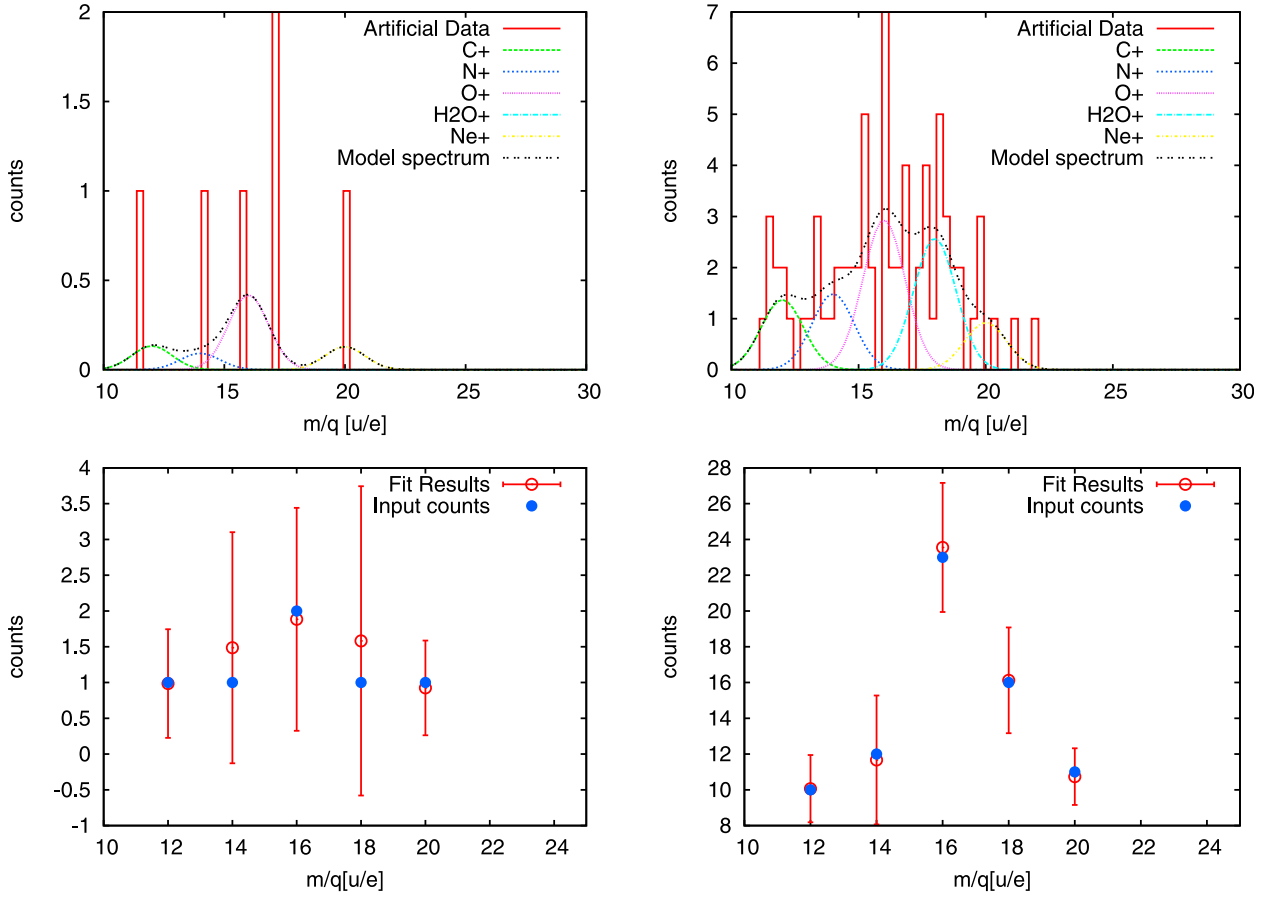


**Figure A1.** (top) Artificial  $m/q$  spectra containing (left) 6 and (right) 72 counts. They were created by Monte Carlo method based on our model from equation (A7). In addition, the results from our analysis applied to the artificial data are shown. (bottom) A comparison between evaluated counts from our analysis and the number of artificial counts (blue circles) that were generated for the five major heavy PUI distributions. The mean counts and the standard deviation from 24 analyzed sets of artificial data are shown in red. The results are in good agreement with the number of generated counts.

[25] As shown above the  $\chi^2$  can be used if Gaussian statistics can be assumed. But if we deal with low count rates the assumption of Gaussian statistics no longer holds true and we have to take Poissonian statistics into account. Equation (A1) then becomes

$$P_M^P(\vec{a}) = \prod_{i=1}^N \frac{y(x_i; \vec{a})^{y_i}}{y_i!} \exp(-y(x_i; \vec{a})). \quad (\text{A4})$$

[26] Again maximizing  $P_M^P(\vec{a})$  is equivalent to minimizing  $-\ln P_M^P(\vec{a})$ . Neglecting the constant term we get

$$E_M^P(\vec{a}) = \sum_{i=1}^N y(x_i; \vec{a}) - y_i \ln(y(x_i; \vec{a})), \quad (\text{A5})$$

as a MLE that is not biased toward low statistics.

[27] For our analysis where we deal with periods of hours  $m/q$  spectra typically contain less than five counts. In order to resolve heavy PUIs in such short time periods we used a

MLE as given in equation (A5). As discussed in section 2 we used Gaussians to model the contributions by heavy PUIs to the  $m/q$  spectra

$$y_i(m/q, a_i) = \frac{a_i}{\sqrt{2\pi} \cdot \sigma} \exp - \frac{(m/q - m/q_{0,i})^2}{2\sigma^2} \quad (\text{A6})$$

with  $y_i(m/q, a_i) = 0$  outside  $3\sigma$ . In addition to  $C^+$ ,  $N^+$ ,  $O^+$ ,  $H_2O^+$ , and  $Ne^+$  two distributions for  $^{22}Ne^+$ , and  $Mg^+$  were fitted. They assure that the trailing edge of the  $Ne^+$  distribution is treated correctly. The final model of the  $m/q$  spectra then becomes

$$y(m/q, \vec{a}) = \sum_{i=1}^7 y_i(m/q, a_i), \quad (\text{A7})$$

where  $\vec{a}$  contains the counts for the fitted species. The minimization is done by a Levenberg-Marquardt algorithm [Press *et al.*, 1999]. Because the fit deals with real numbers but the number of measured counts is an integer, the sum of the

resulting “best fit” parameters  $\bar{a}^F$  is used to get the final ion counts  $\bar{C}$  from the measured counts  $N(m/q)$

$$C_i = \sum_{m/q} N(m/q) \frac{y_i(m/q, a_i^F)}{y(m/q, \bar{a}^F)}. \quad (\text{A8})$$

This serves to assure that  $\sum_i C_i = \sum_{m/q} N(m/q)$ .

[28] We have tested our analysis by applying it to artificial data. The results are shown in Figure A1. Based on our model given by equation (A7) two different sets of artificial data were generated using Monte-Carlo method, one with a total of 6 events (Figure A1 (left)) and one containing 72 events (Figure A1 (right)). Figure A1 (bottom) shows the original number of events, that were generated for each ion separately (blue dots). The red dots denote the averaged count rate results by the fit of 24 generated random samples. Figure A1 (top) shows an example of an artificial data sample together with the derived five major ion contributions. On average a real  $m/q$  spectrum within one h contains five counts, which is comparable to the presented artificial data in Figure A1 (left). As seen from the error bars for a single data set the results can deviate within a factor of two from the original count rates. But averaging the fit results of 24 generated data sets, which is equivalent to binning the hourly count rates of the real data over a day, yields averaged results that are in good agreement with the original count rates. For daily  $m/q$  spectra that are averaged over ten days (Figure A1 (right)), the resulting counts are almost in perfect agreement with the original count rates.

[29] **Acknowledgments.** This work was supported in parts by the German Science Foundation, DFG, under grant Wi-2139/4-1 and University of New Hampshire under NASA STEREO contract NAS5-00132 and grant NNX09AVA49G.

[30] Philippa Browning thanks Hans J. Fahr and another reviewer for their assistance in evaluating this paper.

## References

- Bzowski, M., and M. Krolikowska (2004), Are the Sun-grazing comets the inner source of pickup ions and energetic neutral atoms?, *Astron. Astrophys.*, *435*, 723–732.
- Fahr, H. J. (1974), The extraterrestrial UV-background and the nearby interstellar medium, *Space Sci. Rev.*, *15*, 483–540.
- Fahr, H. J., H. W. Ripken, and G. Lay (1981), Plasma-dust interactions in the solar vicinity and their observational consequences, *Astron. Astrophys.*, *102*, 359–370.
- Galvin, A. B., et al. (2008), The Plasma and Suprathermal Ion Composition (PLASTIC) Investigation on the STEREO Observatories, *Space Sci. Rev.*, *136*, 437–486, doi:10.1007/s11214-007-9296-x.
- Geiss, J., G. Gloeckler, L. A. Fisk, and R. von Steiger (1995), C<sup>+</sup> pickup ions in the heliosphere and their origin, *J. Geophys. Res.*, *100*(A2), 23,373–23,377, doi:10.1029/95JA03051.
- Gloeckler, G., and J. Geiss (1998), Measurement of the abundance of helium-3 in the Sun and in the local interstellar cloud with SWICS on Ulysses, *Space Sci. Rev.*, *84*, 275–284.
- Gloeckler, G., and J. Geiss (2001), Heliospheric and interstellar phenomena deduced from pickup ion observations, *Space Sci. Rev.*, *97*, 169–181.
- Gloeckler, G., et al. (1998), Investigation of the composition of solar and interstellar matter using solar wind and pickup ion measurements with SWICS and SWIMS on the ACE spacecraft, *Space Sci. Rev.*, *86*, 497–539.
- Gloeckler, G., L. A. Fisk, S. Hefli, N. Schwadron, T. Zurbuchen, F. M. Ipavich, J. Geiss, P. Bochsler, and R. Wimmer (1999), Unusual composition of the solar wind in the 2–3 May 1998 CME observed with SWICS on ACE, *Geophys. Res. Lett.*, *26*(2), 157–160, doi:10.1029/1998GL900166.
- Gloeckler, G., L. A. Fisk, J. Geiss, N. A. Schwadron, and T. H. Zurbuchen (2000), Elemental composition of the inner source pickup ions, *J. Geophys. Res.*, *105*(A4), 7459–7463, doi:10.1029/1999JA000224.
- Gloeckler, G., et al. (2004), Observations of the helium focusing cone with pickup ions, *Astron. Astrophys.*, *426*, 845–854, doi:10.1051/0004-6361:20035768.
- Kaiser, M. L., T. A. Kucera, J. M. Davila, O. C. St. Cyr, M. Guhathakurta, and E. Christian (2008), The STEREO mission: An introduction, *Space Sci. Rev.*, *136*, 5–16, doi:10.1007/s11214-007-9277-0.
- Lallement, R., J. C. Raymond, J. Vallerger, M. Lemoine, F. Dalaudier, and J. L. Bertaux (2004), Modeling the interstellar-interplanetary helium 58.4 nm resonance glow: Towards a reconciliation with particle measurements, *Astron. Astrophys.*, *426*, 875–884.
- Mann, I., and A. Czechowski (2005), Dust destruction and ion formation in the inner solar system, *Astrophys. J.*, *621*, L73–L76.
- Möbius, E., D. Hovestadt, B. Klecker, M. Scholer, G. Gloeckler, and F. M. Ipavich (1985), Direct observation of He<sup>+</sup> pick-up ions of interstellar origin in the solar wind, *Nature*, *318*, 426–429.
- Möbius, E., D. Rucinski, D. Hovestadt, and B. Klecker (1995), The helium parameters of the very local interstellar medium as derived from the distribution of He<sup>+</sup> pickup ions in the solar wind, *Astron. Astrophys.*, *304*, 505–519.
- Möbius, E., et al. (2004), Synopsis of the interstellar He parameters from combined neutral gas, pickup ion and UV scattering observations and related consequences, *Astron. Astrophys.*, *426*, 897–907.
- Möbius, E., et al. (2010), He pickup ions in the inner heliosphere—Diagnostics of the local interstellar gas and of interplanetary conditions, *Proceedings of the 9th International Astrophysics Conference*, edited by J. Heerikhuisen et al., Cent. for Space Plasma and Aeron. Res., Univ. of Ala. Huntsville, Huntsville, Ala., in press.
- Paresce, F., S. Bowyer, and S. Kumar (1974), Observations of He i 584 Å nighttime radiation: Evidence for an interstellar source of neutral helium, *Astrophys. J.*, *187*, 633–639.
- Press, W. H., S. A. Teukolsky, W. T. Vetterling, and B. P. Flannery (1999), *Numerical Recipes in C—The Art of Scientific Computing*, 2nd ed., Cambridge Univ. Press., Cambridge, U. K.
- Schwadron, N. A., J. Geiss, L. A. Fisk, G. Gloeckler, T. H. Zurbuchen, and R. von Steiger (2000), Inner source distributions: Theoretical interpretation, implications, and evidence for inner source protons, *J. Geophys. Res.*, *105*(A4), 7465–7472, doi:10.1029/1999JA000225.
- Weller, C. S., and R. R. Meier (1974), Observations of helium in the interplanetary/interstellar wind—The solar-wake effect, *Astrophys. J.*, *193*, 471–476.
- Wimmer-Schweingruber, R. F., and P. Bochsler (2003), On the origin of inner-source pickup ions, *Geophys. Res. Lett.*, *30*(2), 1077, doi:10.1029/2002GL015218.
- Witte, M. (2004), Kinetic parameters of interstellar neutral helium. Review of results obtained during one solar cycle with the Ulysses/GAS instrument, *Astron. Astrophys.*, *426*, 835–844.

L. Berger, C. Drews, and R. F. Wimmer-Schweingruber, Institut für experimentelle und angewandte Physik, Christian-Albrechts-Universität zu Kiel, Leibnizstr. 11, D-24118 Kiel, Germany. (berger@physik.uni-kiel.de; drews@physik.uni-kiel.de; wimmer@physik.uni-kiel.de)

A. B. Galvin and E. Möbius, Space Science Center and Department of Physics, University of New Hampshire, Morse Hall, 8 College Road, Durham, NH 03824, USA. (toni.galvin@unh.edu; eberhard.moebius@unh.edu)

B. Klecker, Max-Planck-Institut fuer extraterrestrische Physik, D-85741 Garching, Germany. (berndt.klecker@mpe.mpg.de)

### 3.3. Supplementary Remarks

#### 3.3.1. Performance of the Poisson Analysis

In order to quantify the overall performance of the proposed species classification (see [Drews *et al.*, 2010], appendix) we compared our analysis to a common box rate technique using an artificial data set. By "box rates" we refer to rates that contain events of a mass-per-charge range that is linked to a certain ion species. By choosing the mass-per-charge ranges of the respective ion species carefully, i.e. making sure the defined  $m/q$  range covers the whole  $m/q$ -distribution of the respective ion, it is possible to achieve a basic species classification. A typical example of box rates are PLASTIC's matrix rates, which were briefly introduced in chapter 2.3. Each matrixrate is defined by a mass-per-charge and mass range that generally covers one and in some cases several ion species. An illustration of a small sample of matrix rates is shown in Fig. 3.2.

Obviously, a box rate technique is able to perform as well as the proposed analysis in the appendix of Drews *et al.* [2010] if the heavy pickup ion mass-per-charge distribution do not overlap. As was shown in Fig. 1 in Drews *et al.* [2010] however, the mass-per-charge distributions of heavy pickup ions as observed by PLASTIC strongly overlap. Therefore, we will compare the results of a box rate technique with our proposed analysis for the case of overlapping mass-per-charge distributions. For that we have used heavy pickup ion box rates that cover the mass-per-charge of  $\pm 1 amu/e$  around the expected mass-per-charge position of the respective ion. The artificial data set has been created in analogy to the description given in the appendix of Drews *et al.* [2010]. A comparison between both methods is shown in Fig. 3.3.

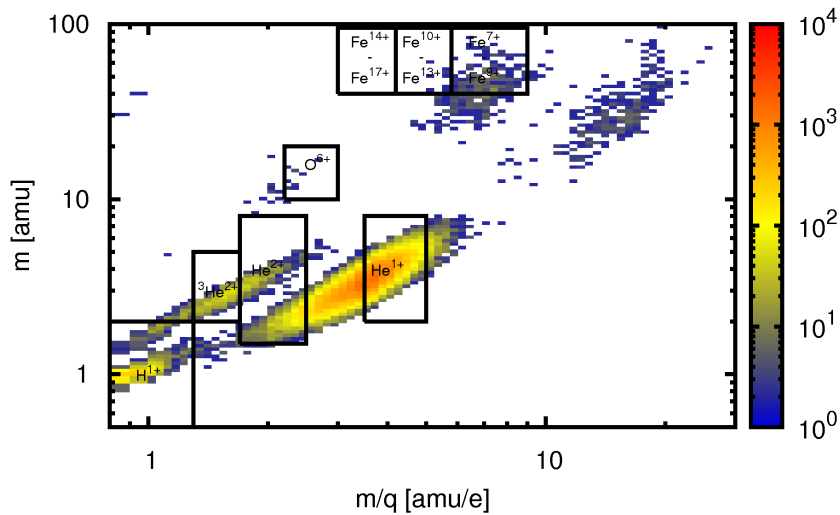


Figure 3.2.: PLASTIC PHA data accumulated over 700 days and sorted into mass (y-axis) and mass-per-charge (x-axis) bins. Several matrix rates (mass and mass-per-charge ranges confined by the black rectangles), which are currently used for the flight model of the instrument, are shown. The figure is taken from Drews [2009].

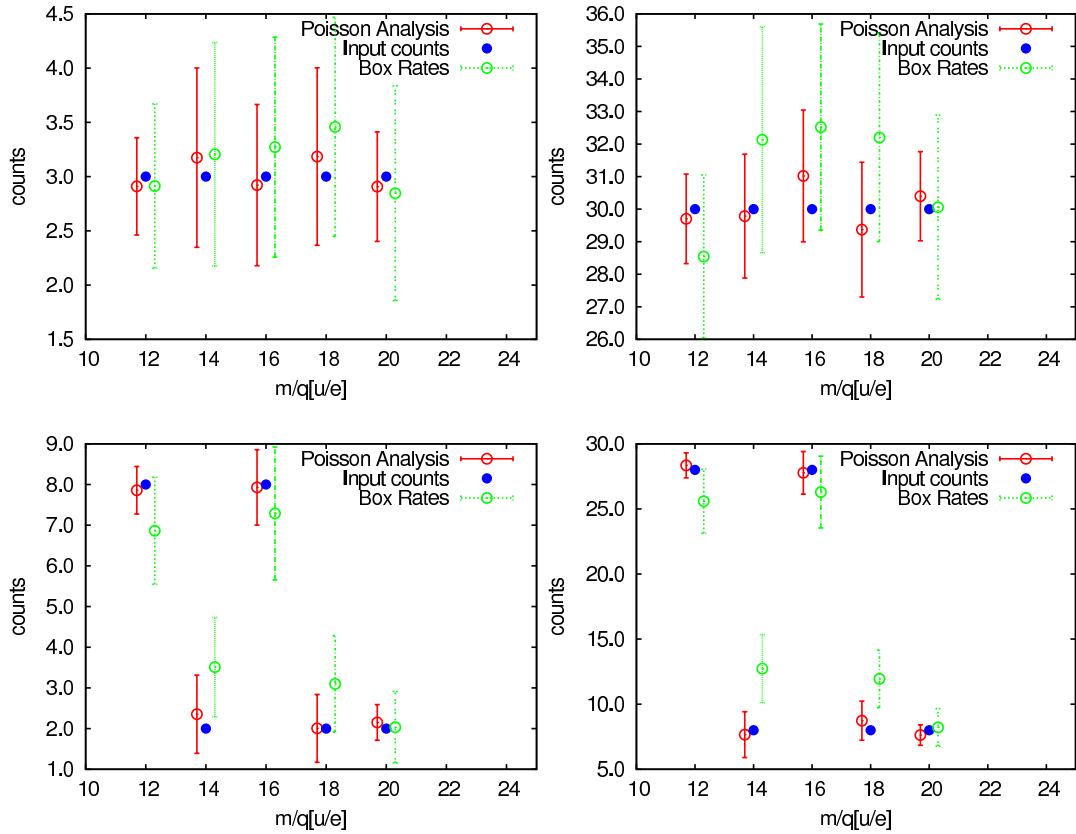


Figure 3.3.: Comparison between the Poisson analysis and box rate method for species classification. The panels show averaged results of the Poisson analysis (red), box rate method (green), and original counts of the underlying model (blue) for a low statistic case (left) and a high statistic case (right). For each case we tested a uniform (top) and non-uniform (bottom) model distribution. The analysis was repeated 100 times to derive the average result and standard deviation of both methods. Despite the overall larger uncertainty of the box rate technique, it is notable that the box rate method also produces a systematic error that comes from spillover of adjacent ion distributions. The significance of this systematic error depends on how uniform the counts are distributed.



## 4. Inflow Direction of the Interstellar Medium

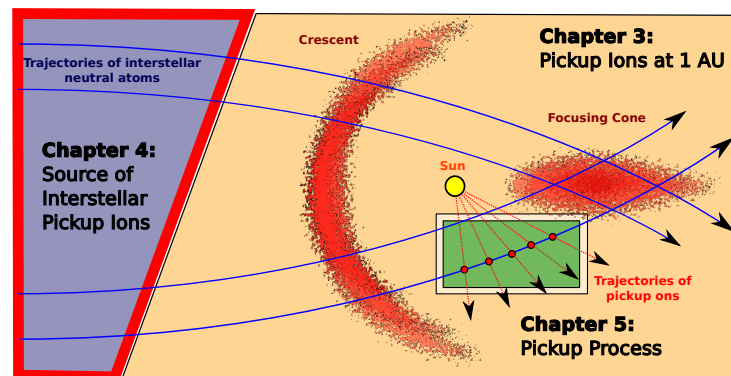


Figure 4.1.: This chapter addresses the spatial distribution of pickup ion at 1 AU (yellow shaded area) with a heavy focus on the formation of the interstellar focusing cone and crescent. Furthermore, the source of interstellar pickup ions is characterized - the interstellar medium (blue shaded area).

### 4.1. Introduction

#### Chapter Overview

This chapter covers our second publication "Inflow direction of interstellar neutrals deduced from pickup ion measurements at 1 AU" [Dreus *et al.*, 2012], which was published in September 2012 in the *Journal of Geophysical Research*, Vol 117. The publication was supervised by Dr. Lars Berger and Prof. Robert Wimmer-Schweingruber, who were involved in all scientific discussions and added greatly to the overall quality of the publication. The remaining co-authors, namely Peter Bochsler, Antoinette B. Galvin, Berndt Klecker, and Eberhard Möbius assisted in form of fruitful discussions about our results and technical issues regarding PLASTIC. The 1<sup>st</sup> author, Christian Dreus, has contributed ~ 80% of the performed study.

In section 4.2 our publication [Dreus *et al.*, 2012] is presented. Section 4.3.1 contains supplementary material covering performance studies of our proposed analysis to determine the inflow direction of interstellar matter. Section 4.3.2 discusses in detail possible systematic influences on our results.

**Abstract of Publication**

”Observations of interstellar pickup ions inside the heliosphere provide an indirect method to access information on the surrounding interstellar medium. The so-called pickup ion focusing cone and pickup ion crescent, which show an imprint of the related longitudinal distribution of interstellar neutrals in form of two overabundances on the down- and upwind side of the sun, are both believed to be aligned along the inflow vector of the interstellar medium. By finding their longitudinal positions we can give an accurate value for the inflow direction  $\lambda_{\text{ISM}}$  of interstellar matter. For that we performed an epoch analysis of interstellar pickup ions measured by the PLASMA and SupraThermal Ion Composition instrument (PLASTIC) on the Solar TERrestrial RELations Observatory mission (STEREO) and were able to reveal in-situ the longitudinal distribution of interstellar  $\text{He}^+$ ,  $\text{O}^+$  and  $\text{Ne}^+$  pickup ions in the ecliptic plane at 1 AU. The previously accepted values for the inflow direction of interstellar matter in ecliptic longitude, as obtained with Ulysses/GAS ( $\lambda = 75.4^\circ \pm 0.5^\circ$ ), Prognoz 6 ( $\lambda = 74.5^\circ \pm 1^\circ$ ), and ACE/SWICS ( $\lambda = 74.43^\circ \pm 0.33^\circ$ ), are currently debated, especially in view of recent results from the Interstellar Boundary Explorer mission (IBEX) that show an inflow direction of interstellar neutral helium of  $\lambda = 79^\circ + 3.0^\circ (-3.5^\circ)$ . Four years of data collected with PLASTIC aboard STEREO A provided sufficient statistics not only to obtain values for the inflow direction of interstellar helium ( $\lambda_{\text{Cone}} = 77.4^\circ \pm 1.9^\circ$  and  $\lambda_{\text{Crescent}} = 80.4^\circ \pm 5.4^\circ$ , deduced from an analysis of the  $\text{He}^+$  focusing cone and crescent respectively), but also to derive values for the inflow direction of interstellar neon ( $\lambda_{\text{Cone}} = 77.4^\circ \pm 5.0^\circ$  and  $\lambda_{\text{Crescent}} = 79.7^\circ \pm 2.6^\circ$ ) and oxygen ( $\lambda_{\text{Crescent}} = 78.9^\circ \pm 3.1^\circ$ ). Although our values for  $\text{He}^+$ ,  $\text{O}^+$  and  $\text{Ne}^+$  are consistent with results from ACE, Ulysses, and Prognoz 6, considering the statistical and systematic uncertainties (except  $\lambda_{\text{Ne,Crescent}}$ ), they are systematically larger than the previously accepted values of  $74.99^\circ \pm 0.55^\circ$  and show a better agreement with the values from IBEX” (from *Dreus et al.* [2012]).

**4.2. Publication**



## Inflow direction of interstellar neutrals deduced from pickup ion measurements at 1 AU

Christian Drews,<sup>1</sup> Lars Berger,<sup>1</sup> Robert F. Wimmer-Schweingruber,<sup>1</sup> Peter Bochsler,<sup>2</sup> Antoinette B. Galvin,<sup>2</sup> Berndt Klecker,<sup>3</sup> and Eberhard Möbius<sup>2,4</sup>

Received 19 March 2012; revised 4 July 2012; accepted 6 August 2012; published 22 September 2012.

[1] Observations of interstellar pickup ions inside the heliosphere provide an indirect method to access information on the surrounding interstellar medium. The so-called pickup ion focusing cone and pickup ion crescent, which show an imprint of the related longitudinal distribution of interstellar neutrals in form of two overabundances on the down- and upwind side of the sun, are both believed to be aligned along the inflow vector of the interstellar medium. By finding their longitudinal positions, we can give an accurate value for the inflow direction  $\lambda_{\text{ISM}}$  of interstellar matter. For that we performed an epoch analysis of interstellar pickup ions measured by the PLASMA and SupraThermal Ion Composition instrument (PLASTIC) on the Solar TERrestrial RELations Observatory mission (STEREO) and were able to reveal in situ the longitudinal distribution of interstellar  $\text{He}^+$ ,  $\text{O}^+$ , and  $\text{Ne}^+$  pickup ions in the ecliptic plane at 1 AU. The previously accepted values for the inflow direction of interstellar matter in ecliptic longitude, as obtained with Ulysses/GAS ( $\lambda = 75.4^\circ \pm 0.5^\circ$ ), Prognoz 6 ( $\lambda = 74.5^\circ \pm 1^\circ$ ), and ACE/SWICS ( $\lambda = 74.43^\circ \pm 0.33^\circ$ ), are currently debated, especially in view of recent results from the Interstellar Boundary Explorer (IBEX) mission that show an inflow direction of interstellar neutral helium of  $\lambda = 79^\circ + 3.0^\circ(-3.5^\circ)$ . Four years of data collected with PLASTIC aboard STEREO A provided statistics sufficient not only to obtain values for the inflow direction of interstellar helium ( $\lambda_{\text{Cone}} = 77.4^\circ \pm 1.9^\circ$  and  $\lambda_{\text{Crescent}} = 80.4^\circ \pm 5.4^\circ$ , deduced from an analysis of the  $\text{He}^+$  focusing cone and crescent, respectively) but also to derive values for the inflow direction of interstellar neon ( $\lambda_{\text{Cone}} = 77.4^\circ \pm 5.0^\circ$  and  $\lambda_{\text{Crescent}} = 79.7^\circ \pm 2.6^\circ$ ) and oxygen ( $\lambda_{\text{Crescent}} = 78.9^\circ \pm 3.1^\circ$ ). Although our values for  $\text{He}^+$ ,  $\text{O}^+$ , and  $\text{Ne}^+$  are consistent with results from ACE, Ulysses, and Prognoz 6, considering the statistical and systematic uncertainties (except  $\lambda_{\text{Ne,Crescent}}$ ), they are systematically larger than the previously accepted values of  $74.99 \pm 0.55^\circ$  and show a better agreement with the values from IBEX.

**Citation:** Drews, C., L. Berger, R. F. Wimmer-Schweingruber, P. Bochsler, A. B. Galvin, B. Klecker, and E. Möbius (2012), Inflow direction of interstellar neutrals deduced from pickup ion measurements at 1 AU, *J. Geophys. Res.*, 117, A09106, doi:10.1029/2012JA017746.

### 1. Introduction

[2] The first in-situ measurement of interstellar pickup ions was performed with SULEICA (SUpra-thermaL Energy Ionic Charge Analyzer) aboard the AMPTE (Active Magnetospheric

Particle Tracer Explorer) spacecraft [Möbius *et al.*, 1985]. This observation not only confirmed the characteristic shape of the  $\text{He}^+$  velocity spectra but also the influence of gravitational focusing on the downwind side of the Sun, which leads to a strong density enhancement of interstellar particles with a low ionization probability. This so-called focusing cone is aligned along the inflow direction of the interstellar medium [Fahr, 1974] and has been observed for  $\text{He}^+$  by resonant backscattering of solar ultraviolet (UV) light [e.g., Paresce *et al.*, 1974] and in-situ measurement of  $\text{He}^+$  pickup ions [e.g., Möbius *et al.*, 1995]. Although the focusing effect is also expected for neon, which has a similar first ionization potential as helium, it was not until 2010 that the first in-situ measurement of the neon focusing cone was made with PLASTIC (Plasma and Suprathermal Ion Composition) on board STEREO A (Solar TERrestrial RELations Observatory Ahead) [Drews *et al.*, 2010]. In addition to the formation of the focusing cone, a second characteristic feature forms

<sup>1</sup>Institute for Experimental and Applied Physics, Christian-Albrechts-University zu Kiel, Germany.

<sup>2</sup>Space Science Center and Department of Physics, University of New Hampshire, New Hampshire, USA.

<sup>3</sup>Institute for Extraterrestrial Physics, Max-Planck Institute, Garching, Germany.

<sup>4</sup>Space Science and Applications, Los Alamos National Laboratory, Los Alamos, New Mexico, USA.

Corresponding author: C. Drews, Institut für experimentelle und angewandte Physik, Christian-Albrechts-Universität zu Kiel, Leibnizstr. 11, 24118 Kiel, Germany. (drews@physik.uni-kiel.de)

©2012. American Geophysical Union. All Rights Reserved. 0148-0227/12/2012JA017746

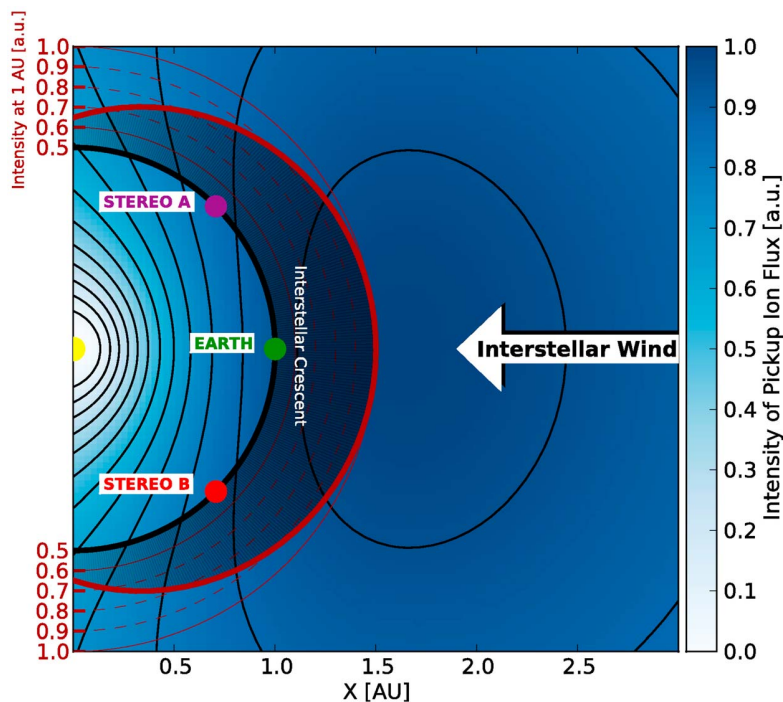


**Figure 1.** Schematic view of the  $\text{Ne}^+$  pickup ion flux in the upwind region of the heliosphere. The strong anisotropy is formed by the interplay of the interstellar neutral inflow, the radially varying ionization efficiency, and the radial expansion of pickup ions after their ionization. The structure at 1 AU strongly resembles the form of a crescent (shown here as a black shaded area). The crescent's intensity, which is normalized to 1 and drawn along Earth's orbit in polar coordinates (thick red line), shows a maximum that is aligned along the axis of the inflowing interstellar wind. Consequently, observations of the related pickup ion count rate at 1 AU allow us to determine the inflow direction of interstellar matter in two separate regions of space using the interstellar focusing cone on the downwind side (not shown) and the interstellar crescent on the upwind side of the sun. Contrary to the formation of the focusing cone, the crescent is most pronounced for species that have a high ionization probability, such as oxygen or hydrogen.

upwind of the Sun. It results from the increasing depletion of interstellar neutral particles with decreasing distance to the Sun. In general, interstellar pickup ions on the downwind side of the Sun show a stronger depletion than their upwind counterparts, as they have not only spent more time in the vicinity of the Sun but have also approached it much closer during their flyby. The resulting overabundance in the upwind region, which we will call interstellar crescent from now on, is aligned along the inflow direction of interstellar matter and spreads over a wide angular range of almost  $180^\circ$ . It is most pronounced for species that have an elevated ionization probability, such as oxygen or hydrogen [McComas *et al.*, 2004]. A schematic view of the interstellar crescent is shown in Figure 1.

[3] Combined measurements of interstellar neutrals, pickup ions and observations of the backscattering of solar ultraviolet radiation were used to derive a consolidated set of interstellar gas parameters, including density, temperature, and inflow direction of the interstellar medium. An overview of recent pickup ion studies and the resulting interstellar gas parameters can be found in Gloeckler *et al.* [2004]. Although the inflow direction of interstellar matter in ecliptic longitude has been estimated by several sources using the

observed signature of  $\text{He}^+$  and neutral helium [e.g., Gloeckler *et al.*, 2004; Möbius *et al.*, 2004], a very recent observation of the interstellar helium neutral gas flow with the Interstellar Boundary Explorer (IBEX) [Möbius *et al.*, 2012] raises doubts about the previously accepted value of  $\lambda_{\text{ISM}} = 74.99^\circ \pm 0.55^\circ$ . The newly estimated inflow direction by the IBEX team ( $\lambda_{\text{ISM}} = 79^\circ + 3^\circ(-3.5^\circ)$ ) [Möbius *et al.*, 2012; Bzowski *et al.*, 2012]) deviates considerably from the results reported by Lallement *et al.* [2004], Witte [2004], and Gloeckler *et al.* [2004]. As pointed out by Möbius *et al.* [2012], the previous helium flow direction of  $\lambda_{\text{ISM}} = 74.7^\circ$  based on Ulysses neutral gas observations [Witte, 2004] was given in B1950 coordinates. In the most commonly used J2000 coordinates this value is  $75.4^\circ$ , which leads to a slight correction of the weighted average quoted by Möbius *et al.* [2004], resulting in  $74.99^\circ \pm 0.55^\circ$ . For the pickup ion observations, it should be noted that interplanetary transport effects may result in a systematic shift of the pickup ion flux with respect to the interstellar inflow direction [e.g., Möbius *et al.*, 1996; Chalov and Fahr, 1999].

[4] Furthermore, a recent study by Lallement *et al.* [2005] on interstellar neutral hydrogen suggest that certain interstellar particles may indeed show a significant deviation from

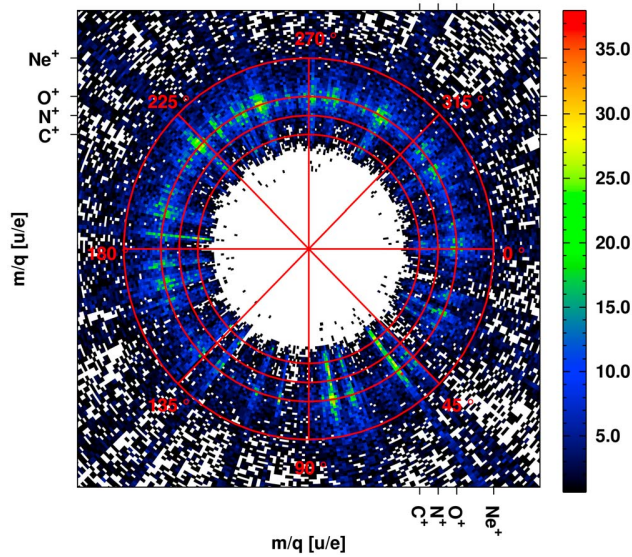


**Figure 2.** Two-dimensional histogram of heavy pickup ions sorted by mass-per-charge and heliographic longitude with respect to the vernal equinox. The data was accumulated for 4 consecutive orbits of STEREO A beginning in March 2007. Instrumental limitations allow for a data acquisition between 22.7 keV/e and 74.9 keV/e only. The four red circles correspond to the mass-per-charge location of  $C^+$ ,  $N^+$ ,  $O^+$ , and  $Ne^+$ .

the previously accepted value of  $\lambda_{ISM}$ . The reason for that is that the very local interstellar magnetic field outside the heliosphere may shape the overall velocity distribution of interstellar neutrals that have a high affinity to undergo charge exchange processes. This can introduce a secondary population of interstellar oxygen and hydrogen atoms, which have a shifted inflow direction with respect to the primary population. Observations at 1 AU of the related  $O^+$  pickup ions would consequently include the superposition of both populations, which could possibly lead to an inflow direction that deviates considerably from values given for helium by *Gloeckler et al.* [2004] or *Möbius et al.* [2004].

[5] Until now observations of the angular distribution of the less abundant heavy pickup ions in the ecliptic plane were still confined to short time periods or did not provide the necessary counting statistics for a detailed analysis. With PLASTIC, we have the capability of observing the heliospheric angular distribution of heavy pickup ions in situ with ample statistics over a duration of at least four years, which allows for the first time to determine the inflow direction of interstellar oxygen and neon and to further refine values given for the helium inflow direction deduced from pickup ion measurements at 1 AU.

## 2. Instrumentation and Data Analysis

[6] In this paper, we present recent observations of interstellar pickup ions with the PLASTIC instrument aboard STEREO A [*Galvin et al.*, 2008]. PLASTIC is a time-of-flight mass spectrometer and utilizes a stepped  $E/q$  analyzer

system together with time-of-flight and energy measurement to determine uniquely the mass, charge, and energy of an ion. The pickup ion data analyzed in this work is collected with the Solar Wind Section (SWS) of PLASTIC. The SWS points toward the Sun and has an angular acceptance of  $\pm 22.5^\circ$  in and  $\pm 20.0^\circ$  out of the ecliptic. Its entrance system can be switched between two different channels, one suited to determine properties of major solar wind ions ( $H^+$  and  $He^+$ ), and the other specifically designed to investigate heavy solar wind ions (e.g.,  $O^{6+}$ ,  $C^{5+}$ ,  $Fe^{3+-13+}$ , ..) as well as pickup ions. The so-called main channel provides a large collection area that is sufficiently large to investigate even the very rare heavy pickup ions, e.g.,  $C^+$ ,  $O^+$ , and  $Ne^+$ . The exceptionally good counting statistics and prolonged measurement time of four years during the extended solar minimum conditions, beginning in March 2007, allow, for the first time, to study the distribution of heavy pickup ions along Earth's orbit with unprecedented quality.

[7] Because pickup ions are singly charged, they are well separated in terms of time-of-flight and energy-per-charge from the other solar wind constituents. This is especially true for pickup ions with masses  $\geq 12$  amu, where only solar wind iron ions of low charge states may induce a small background to the observed pickup ion count rates. For pickup  $He^+$  a possible background from solar wind ions with  $m/q \approx 4$ , e.g.,  $Si^{7+,8+}$  may contribute to the observed count rates. To reduce influences of solar wind-induced background, we set a lower limit to the pickup ion collection to a minimum energy-per-charge of  $E/q_{min}^{HP} = 22.6$  keV/e for heavy pickup ions and  $E/q_{min}^{He^+} = 4.9$  keV/e for  $He^+$ , where  $E/q_{min}^{HP}$  and  $E/q_{min}^{He^+}$  are the typical energy-per-charge values of  $Si^{7+}$  and  $Fe^{3+}$  during standard solar wind conditions ( $v_{sw} = 450$  km/s).

[8] Our analysis makes use of so-called Pulse Height Analysis words to gain access to the full measurement information, including time-of-flight and energy-per-charge measurements. This is necessary to derive the mass-per-charge of incident particles upon which our species classification is based. The mass-per-charge can be calculated with

$$\frac{m}{q} = 2(E/q + V_{PAC})\alpha(E, m)\left(\frac{\tau}{d}\right)^2, \quad (1)$$

where  $\tau$  is the time of flight of incident ions,  $d$  is the time-of-flight path length in the instrument,  $V_{PAC}$  the post acceleration voltage and  $\alpha(E, m)$  the energy and species dependent fractional energy loss of ions during passage of the thin carbon foil, which in turn is necessary to trigger a start signal for the following time-of-flight measurement. Figure 2 shows the derived mass-per-charge spectra of heavy pickup ions sorted by heliographic longitude with respect to the vernal equinox. The data was accumulated over a period of 1450 days ( $\sim 1500^\circ$  in ecliptic longitude) beginning in March 2007 and covers four complete orbits of STEREO A around the Sun. The main contributors to the observed  $m/q$ -spectra are  $C^+$ ,  $N^+$ ,  $O^+$ , and  $Ne^+$  with corresponding  $m/q$  values marked by the red circles. Due to the relatively low time-of-flight resolution of the instrument, the species are not well resolved in mass-per-charge space and it is difficult to identify the pickup ion species based on a single  $m/q$  value. Instead we analyze ensembles of events accumulated within one hour time periods with a Maximum Likelihood method

that is based on Poisson statistics. For that, a Gaussian distribution for each of the heavy pickup ion species is fitted to the respective mass-per-charge range of the one hour  $m/q$ -spectra. As a result we obtain the most probable ion species for each measured  $m/q$  event. A description of this approach is given in greater detail by *Drews et al.* [2010] (see Appendix A), who successfully employed it to observe the focusing effect of  $\text{Ne}^+$ . We note that we did not use data from STEREO B because it does not add significant counting statistics to our sample (approximately a factor three less than STEREO A) and shows a poor signal-to-noise ratio that would add the complication of a second calibration uncertainty to our observations. Therefore, we will only discuss data from STEREO A in this work.

[9] Once the ion species has been derived, and the energy per charge is known, we can determine the pickup ion velocity  $v_{\text{ion}}$  and subsequently the dimensionless quantity

$$w = v_{\text{ion}}/v_{\text{sw}}. \quad (2)$$

Because inner-source pickup ions form deep in the inner heliosphere and cool adiabatically on the way to 1 AU, their  $w$  generally lies below  $w = 1.5$  [*Gloeckler and Geiss*, 1998]. Interstellar pickup ions, on the other hand, are formed mainly locally and their  $w$  generally lies above  $w = 1.5$ . Therefore, we can separate interstellar from inner-source pickup ions by discarding events with  $w \leq 1.5$ . Although a small amount of  $\text{C}^+$ , which stems almost exclusively from the inner source [*Geiss et al.*, 1995], can exceed up to  $w = 2.5$  (see Appendix A), this approach will exclude major contributions of inner-source pickup ions from our analysis. For the following analysis all we need is the  $w$  information which is accurately measured. Nevertheless, a brief description of the observed  $w$ -spectra of  $\text{He}^+$ ,  $\text{C}^+$ ,  $\text{O}^+$ , and  $\text{Ne}^+$  is given in Appendix A.

[10] Figure 3 shows the normalized count rates of  $\text{C}^+$  (top left),  $\text{O}^+$  (top right),  $\text{Ne}^+$  (bottom left), and  $\text{He}^+$  (bottom right) of four separate orbits of STEREO A around the Sun as a function of ecliptic longitude. The first orbit started in March 2007 with the remaining orbits being separated by 347 days each with respect to the prior orbit. The maximum observed count rate of each orbit has been scaled to unity to illustrate differences between the longitudinal distribution of each orbit. In addition we applied a 28-day sliding average to average out the effect of the varying solar wind velocity [see *Drews et al.*, 2010]. One has to keep in mind that although we filtered events by the respective interstellar  $w$ -range, the observed signature of  $\text{C}^+$  still arises from an inner source close to the Sun. The  $\text{C}^+$  events are faster than expected for a cooled inner-source distribution, possibly due to acceleration processes in the inner heliosphere. Moreover, we do not expect a distinct longitudinal pattern over the course of four orbits as for interstellar pickup ions [e.g., *Allegrini et al.*, 2005; *Geiss et al.*, 1996]. Thus, we can attribute most features of the  $\text{He}^+$ ,  $\text{O}^+$  and  $\text{Ne}^+$  longitudinal distributions, which are also visible in  $\text{C}^+$ , to instrumental effects, such as the detection efficiency and coverage in  $w$ , or to an imprint of the underlying solar wind structure, e.g., density compression or co-rotating interaction regions [*Möbius et al.*, 2010].

[11] The most distinct feature visible for  $\text{He}^+$  is the formation of the focusing cone, which has already been observed with PLASTIC by *Möbius et al.* [2010]. The cone is aligned around  $\sim 75^\circ$  and seems to vary by almost  $15^\circ$  from orbit to orbit. A likely explanation for this variation is a strong modulation by solar wind streams, as was reported by *Möbius et al.* [2010] for  $\text{He}^+$  and by *Drews et al.* [2010] for  $\text{He}^+$ ,  $\text{C}^+$ ,  $\text{O}^+$ , and  $\text{Ne}^+$ . In Figure 3 one can also observe the interstellar crescent of  $\text{He}^+$ , whose symmetry axis is aligned with that of the focusing cone as well for orbits one, two, and four, while the third orbit shows a highly asymmetric crescent.  $\text{Ne}^+$ , which has a slightly higher ionization rate at 1 AU of  $3.65 \cdot 10^{-7} \text{ s}^{-1}$  than  $\text{He}^+$  ( $1.19 \cdot 10^{-7} \text{ s}^{-1}$ ) [*Cummings et al.*, 2002], shows a crescent feature that is more pronounced in all orbits. However, it also shows stronger small-scale variations, which is likely due to the decreased counting statistics compared to  $\text{He}^+$ . Similar to  $\text{He}^+$ , we also observe a  $\text{Ne}^+$  focusing cone signature as was already shown by *Drews et al.* [2010]. Interestingly, the  $\text{Ne}^+$  cone seems to be well developed during orbits one and three, while orbits two and four show only a minor effect of focusing. During the fourth orbit this may be caused by an increase of the ionization probability, which started in 2010 during the renewed increase of solar activity. This is also supported by the fact that during this period  $\text{He}^+$  shows a crescent to focusing cone ratio, which is slightly increased compared to orbits one and two. During the second orbit, however, no significant increase of the ionization rates can be seen and the weakly developed focusing cone is likely due to an insufficient  $w$ -coverage (see Appendix A) or due to modulation of the solar wind. Such a modulation, e.g., transits of co-rotating interaction regions, density compression or simply high speed stream, are likely to have a greater effect on  $\text{Ne}^+$ , because neutral interstellar neon will have a lower thermal speed compared to neutral helium if the two have equal temperatures in the local interstellar medium, which then results in a narrower focusing cone. Therefore, modulations by the solar wind could substantially suppress the  $\text{Ne}^+$  cone structure, while the broader focusing cone of  $\text{He}^+$  still produces a clear signature in the observed count rates. The effect of a solar wind modulation has also been observed comparing the  $\text{He}^+$  focusing cone of PLASTIC aboard STEREO A and B [*Möbius et al.*, 2010].

[12] During all four orbits the  $\text{O}^+$  abundance drops to almost zero in the vicinity of the focusing cone passage. One exception is a small focusing signature during the third orbit that is also visible for  $\text{C}^+$ . As explained in Appendix A, we expect this signature to be of instrumental nature, likely caused by a background of energetic  $\text{He}^+$  events. Because  $\text{O}^+$  has the highest ionization rate with  $8.48 \cdot 10^{-7} \text{ s}^{-1}$  of the investigated interstellar species, it shows very well developed crescents that coincide nicely with the inflow direction of interstellar matter. Interestingly, the longitudinal structure of the  $\text{He}^+$ ,  $\text{O}^+$ , and  $\text{Ne}^+$  crescents show some resemblance even on scales of a few degrees, which indicates that modulation by the solar wind may have a considerable impact on the observed longitudinal structure.

[13] The observed  $\text{C}^+$  abundance shows no distinct features that are sustained over all orbits and is consistent with an isotropic source around the Sun as expected for an inner-source origin. In particular, no strong correlation between

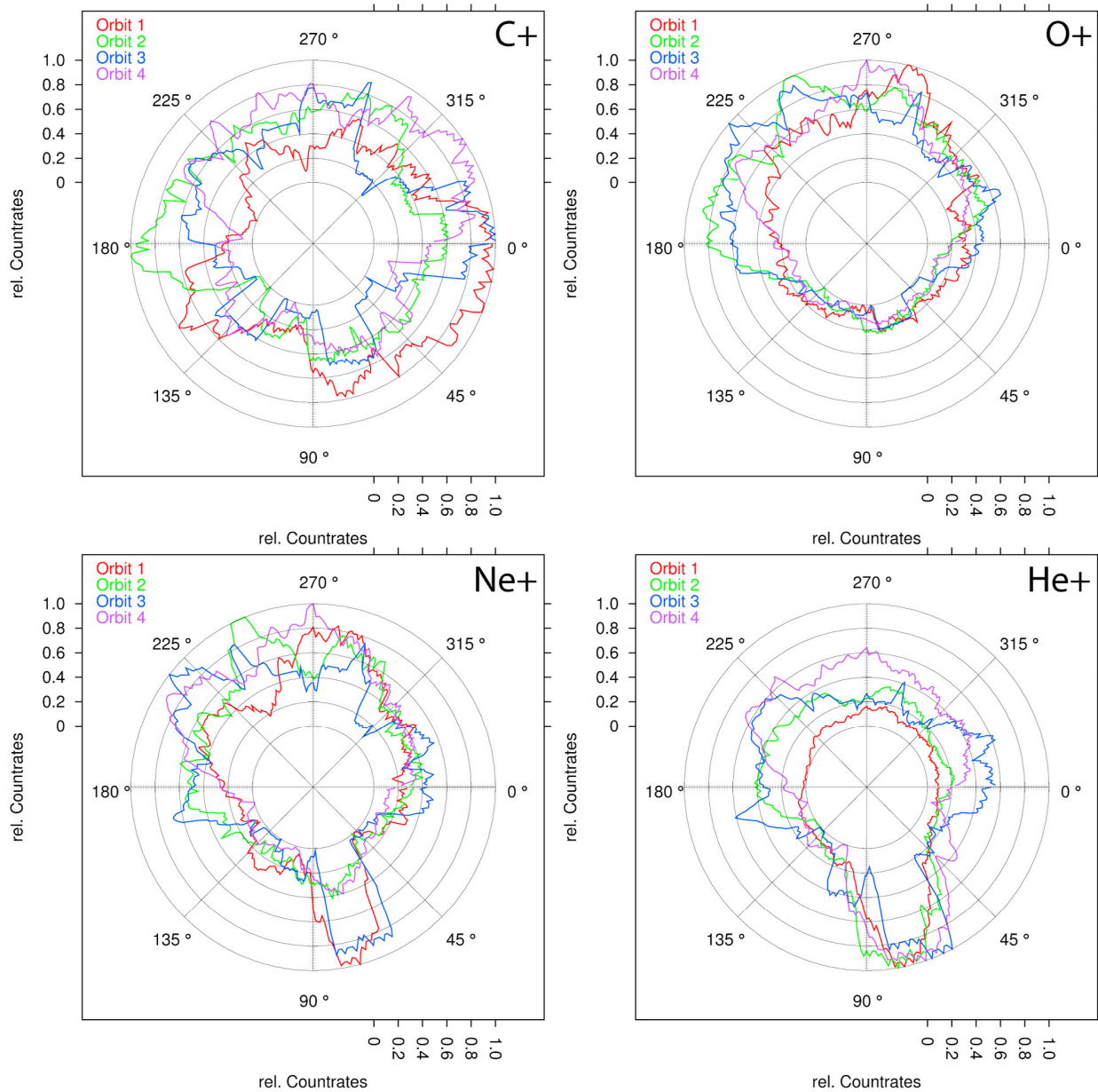


**Figure 3.** A 28-day sliding average of count rates of  $C^+$  (top left),  $O^+$  (top right),  $Ne^+$  (bottom left), and  $He^+$  (bottom right) for STEREO A with  $w > 1.5$  sorted into the respective ecliptic longitude. Each color represents 347 days of data, which corresponds to one orbit of STEREO A (start date of first orbit was 1 March 2007). In each 347-day interval the maximum intensity of the current orbit was normalized to 1. Interstellar  $He^+$  shows a clear focusing signature during all 4 orbits as well as  $Ne^+$ , for which the focusing cone is most prominent during orbits 1 and 3.  $C^+$  and  $O^+$ , which are expected to show no focusing effect (or at best a minor one for  $O^+$ ), also show a focusing signature during orbit 3. This signature is caused by an extended  $He^+$  TOF background during this particular cone passage that has the strongest impact on heavy pickup ions with low mass-per-charge. Consequently this signature is less prominent for  $O^+$  than for  $C^+$ . The crescent structure that forms between  $160^\circ$  and  $350^\circ$  occurs during all orbits. Here,  $O^+$  shows the clearest signature, while the  $He^+$  and  $Ne^+$  crescent structures seem to be superposed by small-scale structures (especially during orbit 3) that are possibly induced by underlying solar wind density and velocity variations.  $C^+$  shows neither a clear focusing nor crescent structure and is, apart from small-scale variations, in agreement with an isotropic distribution.

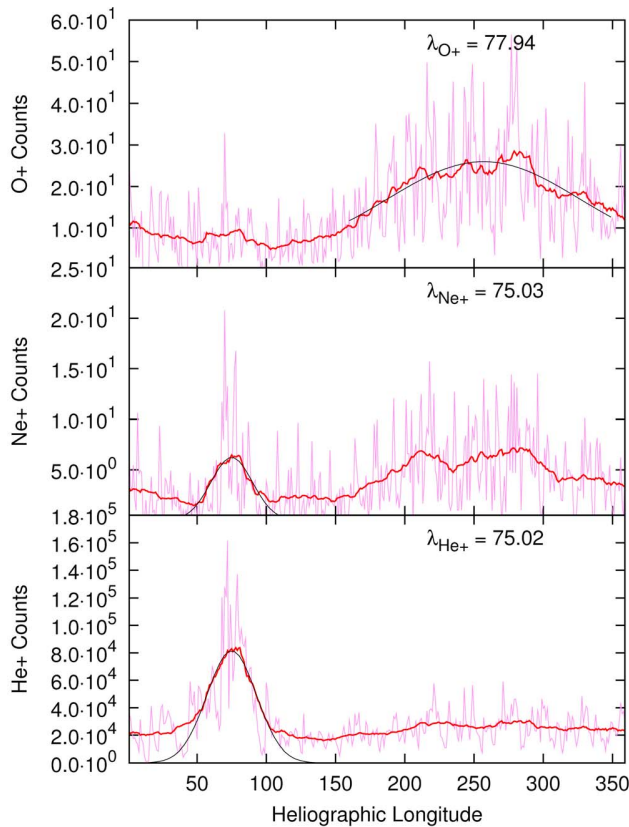


**Figure 4.** Count rates of  $O^+$  (top),  $Ne^+$  (center), and  $He^+$  (bottom) for four consecutive orbits of STEREO A with  $w > 1.5$  sorted into the respective ecliptic longitude. To determine the inflow direction, a Gaussian distribution is fitted to the focusing cone of  $He^+$  and  $Ne^+$  and a cold pickup ion model is applied to the  $O^+$  crescent signature.

inner-source  $C^+$  and interstellar  $He^+$ ,  $O^+$ , and  $Ne^+$  can be observed, from which we conclude that the observed interstellar features are indeed shaped by heliospheric processes rather than instrumental effects.

### 3. Data Interpretation

[14] The purpose of our analysis is to estimate and better define the inflow direction of interstellar atoms as deduced from pickup ion measurements at 1 AU. For that we will pursue two different approaches. The first will follow standard methods used throughout several publications about  $He^+$  pickup ions. The second is tailored to account for possible systematic biases in our analysis. As discussed in the following, such effects need to be accounted for to properly treat  $O^+$  and  $Ne^+$ .

[15] For the first approach, we superpose all available data points of four orbits of STEREO A to derive the distribution of  $He^+$ ,  $O^+$  and  $Ne^+$  with respect to ecliptic longitude. The results are shown in Figure 4, where the magenta colored curve denotes the raw pickup ion data and the red curve a 28-day sliding average. To determine the inflow direction, a Gaussian distribution is fitted to the observed focusing cone signature of  $He^+$  and  $Ne^+$ , and an interstellar cold model

[Vasyliunas and Siscoe, 1976] is fitted to the respective range of the  $O^+$  crescent. Both features are separated by  $180^\circ$  and believed to be aligned along the inflow direction of the interstellar medium. Using this approach we are able to derive the inflow directions as  $\lambda_{He^+} = 75.0^\circ$ ,  $\lambda_{O^+} = 77.9^\circ$ , and  $\lambda_{Ne^+} = 75.0^\circ$ . We do not expect any detrimental effect on the determination of the inflow direction due to our use of a Gaussian or the cold model instead of a more sophisticated warm model.

[16] To estimate the statistical uncertainty of our measurements, we use a rejection sampling technique to generate random samples of the observed  $He^+$ ,  $O^+$  and  $Ne^+$  signatures [Robert and Casella, 2004]. The probability distribution function (PDF) used for that technique has to be chosen to reflect the observed  $He^+$  and  $Ne^+$  focusing cone and the  $O^+$  crescent as accurately as possible. Considering that we already derived a best fit to the observed focusing cone and interstellar crescent signature, this is an easy task and we use a Gaussian distribution for the observed focusing cone signature ( $He^+$ ,  $Ne^+$ ) and an interstellar cold model for the observed crescent signature ( $He^+$ ,  $O^+$ ,  $Ne^+$ ) as our PDF. On the basis of that PDF, we generate 2000 random samples of the observed  $He^+$ ,  $O^+$ , and  $Ne^+$  signatures in the given angular range covered by the data. The number of generated events in each sample and for each pickup species is chosen to reflect the actual number of events found in our data sets. For each of the generated random samples we perform our analysis to determine the inflow direction and by finding the results' standard deviation we derive the statistical fluctuations of our measurement. We obtain statistical uncertainties of  $\Delta\lambda = 0.3^\circ$ ,  $1.4^\circ$ , and  $2.9^\circ$  for  $He^+$ ,  $O^+$  and  $Ne^+$ , respectively, which obviously scales with the size of the random samples.

[17] As already alluded to, the observed pickup ion count rates are further modulated by the underlying solar wind structure, such as density compressions, which can considerably alter the observed pickup ion signature [Möbius et al., 2010]. Furthermore, the solar wind speed affects the spectral coverage of the instrument (see Appendix A) and constrains the observable pickup ion velocity, which in turn influences the probability for pickup ion detection. As a net effect the observed interstellar features, namely the focusing cone and crescent, may be shifted by several degrees with respect to the interstellar inflow direction depending on the underlying solar wind structure. An example for this systematic bias is visible in Figure 3, where a strong variation of the  $He^+$  focusing cone position from orbit to orbit can be observed.

[18] In order to quantify and incorporate this systematic bias in our results, the influences of the energy and species dependent detection efficiency  $\eta(E, m)$  and spectral coverage have to be known. Pickup ion intensity variation by the spectral coverage can be estimated with an assumption for the expected pickup ion  $w$ -spectra and  $w$ -coverage (see Appendix A). To estimate the impact of the varying detection efficiency,  $\eta(E, m)$  has to be derived. Because  $\eta(E, m)$  is, due to instrumental aging effects, time dependent, it can only be derived in flight using flight data. Unfortunately, this method can only be used for  $He^+$  and not for the heavy pickup ions because of their low counting statistics. Furthermore, influences from density compression or co-rotating interaction regions on the observed pickup ion signature and the resulting bias on the determined inflow direction are

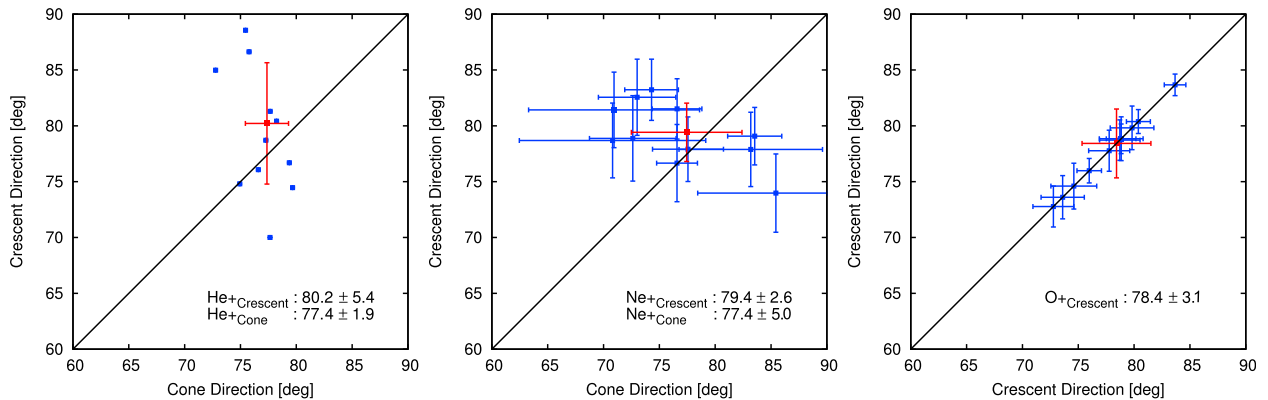


**Figure 5.** Inflow direction of He<sup>+</sup> (left), Ne<sup>+</sup> (center), and O<sup>+</sup> (right) measured in the upwind region ( $y$ -axis) and downwind region (He<sup>+</sup>, Ne<sup>+</sup>:  $x$ -axis). For each possible combination of orbits, noise was added to the observed count rates and the inflow direction was determined 2000 times to give an estimate of the expected statistical error (blue error bars) and mean inflow direction in upwind and downwind regions ( $x$ - and  $y$ -coordinate of blue squares, respectively). The red squares denote the average inflow direction with corresponding standard deviation (red error bars) of all orbit combinations. The mean value and standard deviation of the inflow direction were determined using a weighted average of all possible orbit combinations, whereas the weight was determined by the statistical uncertainty and number of data points of the given orbit combination. If the position of the focusing cone and crescent structure would be aligned along the same axis that is likely determined by the velocity vector of the LISM, the blue squares would align along the black line (Note that for O<sup>+</sup> the cone position cannot be determined and that the right panel shows the crescent position on the  $x$ -axis instead).

even more difficult to quantify. Therefore, our first approach yields an unknown systematic bias of  $\lambda_{\text{He}^+}$ ,  $\lambda_{\text{O}^+}$ , and  $\lambda_{\text{Ne}^+}$ .

[19] For the second approach we developed a method that enables us to preserve the longitudinal distribution of interstellar pickup ions despite any underlying small-scale structures. This method is especially well suited for taking into account stochastic variations, which are introduced by changes of the solar wind velocity and density on short timescales, and requires minimum knowledge of instrumental calibration parameters, such as the detection efficiency or spectral coverage. As long as certain requirements on the observed pickup ion signatures are met, we can use this approach to derive an unbiased value for the inflow direction of interstellar He<sup>+</sup>, as well as interstellar O<sup>+</sup> and Ne<sup>+</sup>. The necessary requirements are listed and discussed in the following paragraph.

[20] (1) The inflow direction of interstellar neutrals is time independent or at least constant over the observed period from February 2007 to June 2011. (2) The influence of the time dependent pickup ion ionization rate during the observed period from February 2007 to June 2011 is small or at least well known. (3) Any impact of the detection efficiency decay from MCP aging during the observed period from February 2007 to June 2011 is small or at least well known.

[21] Because it is very unlikely that the relative motion of our solar system through the local interstellar cloud has changed significantly over the course of four years, we have no reason to believe that requirement (1) is invalid. To validate (2) we investigated He<sup>+</sup> count rates with SWICS on board ACE over a period of 10 years and compared the observed signature with the solar UV rate given by the Solar Extreme Ultraviolet Monitor (SEM) on board the Solar and

Heliospheric Observatory (SOHO) [Hovestadt *et al.*, 1995]. Because the solar UV rate changes only slightly between 2007 and 2011, its effect on the observed He<sup>+</sup> signature, e.g., introducing an asymmetry to the observed angular distribution, is very weak and can be neglected. To validate (3) we have to estimate the impact of a sustained efficiency decay on our analysis, which would effectively introduce a negative skewness to the observed angular distribution. For that we applied our analysis, described below, to a series of artificial data sets, which were convoluted by different efficiency decays, to determine the expected influence on the deduced inflow direction. We found that an exponential efficiency decay from 100% to 40% over the course of four orbits, would introduce a systematic shift of around  $-4.0^\circ$  (crescent) and  $<0.5^\circ$  (cone) to our measurement of the interstellar inflow direction, while a linear efficiency decay introduces a shift of around  $-3.0^\circ$  (crescent) and  $<0.5^\circ$  (cone). In reality, the instrumental efficiency decay is neither exponential nor linear due to frequent increases of the MCP bias, which compensate, in part, for the decrease in efficiency. Consequently, we need to incorporate the real efficiency decay for validation of (3). To determine the He<sup>+</sup> efficiency decay, we followed an approach originally proposed by Klecker *et al.* [2009] that uses housekeeping data of PLASTIC to estimate the He<sup>+</sup> efficiency on a daily basis. This approach, however, can not be applied to Ne<sup>+</sup> or O<sup>+</sup> due to their small flux compared to solar wind ions and forces us to apply the He<sup>+</sup> efficiency decay also to the heavy pickup ions. Fortunately, pre-calibration of PLASTIC's MCPs performed with 60 keV H<sup>+</sup>, He<sup>+</sup>, O<sup>+</sup>, and Ar<sup>+</sup> clearly showed that aging of the MCPs will cause a greater decay of the MCP trigger probability for light ions than for heavy ions. Therefore, applying the He<sup>+</sup> efficiency decay for heavy pickup ions would result in an

overestimation of the expected systematic shift of the derived interstellar inflow direction deduced from  $O^+$  and  $Ne^+$ .

[22] Using the  $He^+$  efficiency decay we find, contrary to our expectations based on an exponential or linear efficiency decay that its actual impact only introduces a systematic error of  $+1^\circ$  (crescent) and  $-1.0^\circ$  (cone). The reason for that is that the  $He^+$  efficiency function shows no distinct decay during the last two orbits and is dominated by small-scale fluctuations, which, as discussed later, are treated properly with our analysis using approach 2.

[23] Our proposed method is based on the idea that one can disentangle the spatial and temporal variations of the observed pickup ion signature  $n(\phi, t)$

$$n(\phi, t) = V_r(\phi) \cdot M(v_{sw}(t), n_{sw}(t), \mathbf{B}(t), \eta(t), \dots) = V_r(\phi) \cdot M(t), \quad (3)$$

where the spatial variation is given by the pickup ion model  $V_r(\phi)$  which is independent from time  $t$ , given the requirements (1) and (2).  $M(t)$  constitutes a modulation parameter that incorporates changes in the observed pickup ion intensities by changes of the solar wind speed  $v_{sw}(t)$ , solar wind density  $n_{sw}(t)$ , magnetic field direction and strength  $\mathbf{B}(t)$ , and instrumental efficiency  $\eta(t)$ . Given the requirement (3), this parameter is time dependent but not related to the ecliptic longitude  $\phi$ . Multiplication of  $V_r(\phi)$  and  $M(t)$  then yields the pickup ion count rate observed by PLASTIC. Naturally, we do not know the underlying model nor the modulation parameter, but by using the assumption that  $V_r(\phi)$  does not change from orbit to orbit and that PLASTIC has already performed four orbits around the Sun, we can derive a relative modulation parameter  $G(t)$ , which constitutes the variation of the pickup ion intensity in one orbit relative to the average intensity over all considered orbits.  $G(t)$  is then defined as follows:

$$G(t) = \frac{n(\phi, t)}{\sum_{a=0}^{N_O-1} n(\phi, t + aT)} = \frac{M(t)}{\sum_{a=0}^{N_O-1} M(t + aT)}, \quad (4)$$

where  $n(\phi, t)$  and  $M(t)$  are defined in equation (3),  $T$  denotes the time it takes for STEREO A to complete one complete orbit and  $N_O$  is the number of orbits taken into account for the analysis since 2007.  $G(t)$  constitutes only relative changes of the pickup ion intensity, so it is necessary to take at least two orbits into account in equation (4) up to a maximum of four orbits.

[24] As  $G(t)$  is decoupled from the underlying pickup ion model, we can now try to find a suited pickup ion model  $V_m(\phi, \lambda_0)$ , which, by multiplication with  $G(t)$  and the total number of observed counts  $N_C$ , reproduces the observed pickup ion count rates  $n(\phi, t)$  of PLASTIC once the correct model parameter, e.g., the inflow direction of the interstellar medium, is found. Consequently, the model for the pickup ion count rates of PLASTIC is obtained as

$$F(\phi, t, \lambda_0) = N_C \cdot V_m(\phi, \lambda_0) \cdot G(t). \quad (5)$$

As our pickup ion model we use, in analogy to our first approach, an interstellar cold model for the crescent region and a normal distribution for the interstellar focusing cone.

We can then derive the most likely inflow direction of interstellar neutrals by minimizing the maximum-likelihood estimator (MLE)  $\xi_P(\lambda_0)$  of our assumed model  $F(\phi, t, \lambda_0)$  and the data set  $n(\phi, t)$

$$\xi_P(\lambda_0) = \sum_{a=0}^{N_O-1} \sum_{\phi=\phi_0}^{\phi_N} F(\phi, t + aT, \lambda_0) - n(\phi, t + aT) \quad (6)$$

$$\cdot \ln(F(\phi, t + aT, \lambda_0)). \quad (7)$$

[25] The MLE used here is based on Poisson statistics to account for the rare nature of heavy pickup ions. To give well defined values for  $\lambda_{He^+}$ ,  $\lambda_{O^+}$ , and  $\lambda_{Ne^+}$ , we also have to estimate possible statistical and systematic errors of our proposed method. To obtain the statistical error, we add Poisson noise to our data set  $n(\phi, t)$  and repeat our analysis 2000 times. The fluctuation of the thus obtained mean result yields the statistical error of our analysis. Note that our data set is already Poisson distributed, so this procedure results in an overestimation of the statistical error.

[26] To give an estimate of the systematic error, we first have to identify possible sources of systematic biases. We already ruled out significant influences by the solar UV rate or a gradual efficiency decay from MCP aging. Still, an unfavorable interplay of high speed solar wind streams during different orbits may introduce a bias to our analysis, which could shift our result either to lower or higher inflow directions. By taking advantage of the four full orbits STEREO A has performed since 2007, we can apply our analysis to eleven unique orbit permutations, which all show a unique interplay of solar wind streams. Using this approach, we will not be able to derive a distinct value of the inflow direction of each observed orbit, but can derive the most likely inflow direction of interstellar matter over the course of four orbits. Keep in mind that even one additional orbit in our analysis will increase the number of unique orbit permutations to 26, which will significantly reduce the systematic error by an unfavorable distribution of high speed streams.

[27] The results of our second approach are shown in Figure 5. Here we determined the inflow direction of  $He^+$  (left),  $Ne^+$  (center), and  $O^+$  (right) using the signature of the focusing cone ( $x$ -axis) and the interstellar crescent ( $y$ -axis, excluding  $O^+$ ). Our analysis was performed for each unique orbit permutation of STEREO A (blue squares) and repeated 2000 times to determine the statistical fluctuation (blue error bars). The red square and corresponding error bar in each panel denotes the most likely inflow direction of the given pickup ion over the course of four orbits.

[28] What has not been considered yet is the elliptical orbit of STEREO A and its inclination with respect to the inflow vector of the interstellar medium. The inclination influences the conversion from time to heliographic longitude and has been estimated to be negligible for our analysis. STEREO A's elliptical orbit, however, has a measurable impact on our results as its major axis is shifted by  $\sim 45^\circ$  (in ecliptic longitude) with respect to the axis of inflowing interstellar matter. As a result, the observed location of the focusing cone and crescent not only depends on the ecliptic longitude but also on STEREO A's distance from the sun, which varies by



**Table 1.** Inflow Direction of Interstellar Atoms Deduced From Pickup Ion Measurements<sup>a</sup>

	He <sup>+</sup>	O <sup>+</sup>	Ne <sup>+</sup>
$\lambda_{\text{Cone}} \pm \Delta\lambda[^\circ]$	$77.4 \pm 1.9$	-	$77.4 \pm 5.0$
$\lambda_{\text{Crescent}} \pm \Delta\lambda[^\circ]$	$80.4 \pm 5.4$	$78.9 \pm 3.1$	$79.7 \pm 2.6$

<sup>a</sup>The results are corrected for the eccentricity of STEREO A's orbit but may be systematically shifted by  $+1^\circ$  ( $\lambda_{\text{Crescent}}$ ) or  $-1^\circ$  ( $\lambda_{\text{Cone}}$ ) due to the detection efficiency decay. A weighted average using  $1/\Delta\lambda^2$  as our weight yields an inflow direction in ecliptic longitude of  $\lambda_{\text{ISM}} = 78.4^\circ \pm 1.3^\circ$ .

$\sim 1\%$  over the course of a complete orbit. We estimated the influence of the eccentricity on our results to be  $\Delta\lambda_{\text{He,Crescent}} = -0.2^\circ$ ,  $\Delta\lambda_{\text{O,Crescent}} = -0.5^\circ$  and,  $\Delta\lambda_{\text{Ne,Crescent}} = -0.3^\circ$ . We found that neutrals with low ionization potentials, which tend to produce a more pronounced crescent signature, are affected the most by the orbit eccentricity. Effects on the location on the focusing cone, however, are due to its small width negligible. The final results for the most likely inflow direction of the interstellar medium are summarized in Table 1.

#### 4. Discussion and Conclusion

[29] Using data from PLASTIC on board STEREO A we have performed an epoch analysis of four consecutive orbits of interstellar He<sup>+</sup>, O<sup>+</sup>, and Ne<sup>+</sup> pickup ion count rates. We have determined the inflow direction of interstellar matter using two different techniques of which the first one disregards influences of the solar wind structure on the observed interstellar features, while the second one was specifically designed to account for small-scale variations of the observed pickup ion signatures by external factors. We have shown that our first technique yields an inflow direction of interstellar helium and neon that is in agreement with results previously published by *Gloeckler et al.* [2004] and *Möbius et al.* [2004] and deduced from helium measurements. If we consider only the statistical errors and compare the derived inflow direction of He<sup>+</sup> with that of O<sup>+</sup>, we could state that they deviate from each other by  $\sim 1^\circ$ —a result that would be in agreement with the assumption of a secondary O<sup>+</sup> population influenced by the external interstellar magnetic field. Due to a larger statistical error Ne<sup>+</sup> would be consistent with both  $\lambda_{\text{He}^+}$  and  $\lambda_{\text{O}^+}$ , although a secondary Ne<sup>+</sup> population is not expected, due to its smaller cross section for charge exchange processes compared to O<sup>+</sup>. We have also argued that our results using the first technique are indeed biased by solar wind modulations. *Möbius et al.* [2010] proposed that small-scale variations of the magnetic field and ionization rate may also shape the form of the observed pickup ion signatures at 1 AU. Considering that these systematic biases are difficult to quantify with STEREO PLASTIC, especially for the low-flux heavy pickup ions, we claim that our first technique should not be applied to determine the inflow direction of interstellar matter.

[30] Our second technique, however, incorporates effects of small-scale variations induced by external influences. Using this technique, instrumental difficulties, e.g., the decay in detection efficiency, can still introduce a bias to our results. But using a consolidated data set of four orbits of STEREO A, we were able to give an upper limit of the expected systematic error, which finally allowed us to

derive a well-defined value for the inflow direction of interstellar matter deduced from He<sup>+</sup>, O<sup>+</sup>, and Ne<sup>+</sup> pickup ions. After including potential biases from the detection efficiency, we found an inflow direction of interstellar helium with respect to the vernal equinox of  $\lambda_{\text{He,Cone}} = 77.4^\circ \pm 1.9^\circ$  and  $\lambda_{\text{He,Crescent}} = 80.4^\circ \pm 5.4^\circ$ . These results are barely consistent with results from *Gloeckler et al.* [2004] ( $\lambda_{\text{He}} = 74.43^\circ \pm 0.33^\circ$ ) and *Möbius et al.* [2004] ( $\lambda_{\text{He}} = 74.99^\circ \pm 0.55^\circ$ , corrected for J2000). The large uncertainty of  $\lambda_{\text{He,Crescent}}$  is produced by the fact that the He<sup>+</sup> crescent is not well developed due to the low ionization probability of He<sup>+</sup> compared to O<sup>+</sup> and Ne<sup>+</sup>. Our results for Ne<sup>+</sup> are comparable with that of He<sup>+</sup> with  $\lambda_{\text{Ne,Cone}} = 77.4^\circ \pm 5.0^\circ$  and  $\lambda_{\text{Ne,Crescent}} = 79.7^\circ \pm 2.6^\circ$ , although the uncertainty by statistical fluctuations is much higher (Figure 5). Because O<sup>+</sup> shows no significant focusing effect, determination of the interstellar oxygen inflow direction is confined to measurements of the O<sup>+</sup> crescent and yields  $\lambda_{\text{O,Crescent}} = 78.9^\circ \pm 3.1^\circ$ .

[31] Differences between  $\lambda_{\text{He}}$ ,  $\lambda_{\text{O}}$ , and  $\lambda_{\text{Ne}}$  are not evident. In fact, influences of a secondary population of interstellar oxygen, as suggested by *Lallement et al.* [2005], are most likely too small to be seen in our measurement considering an error of  $\Delta\lambda_{\text{O,Crescent}} = \pm 3.1^\circ$ . Differences of  $\lambda_{\text{Crescent}}$  and  $\lambda_{\text{Cone}}$  are insignificant when the systematic bias of the detection efficiency decay is included. Considering the uncertainties of our results, only  $\lambda_{\text{Ne,Crescent}}$  shows an inflow direction that deviates by around  $2^\circ$  from the inflow direction given by *Gloeckler et al.* [2004] and *Möbius et al.* [2004]. Nonetheless, all five values seem to be systematically shifted toward larger ecliptic longitudes and show a better agreement with values given by IBEX  $\lambda_{\text{ISM}} = 79^\circ + 3^\circ (-3.5^\circ)$  [*Möbius et al.*, 2012; *Bzowski et al.*, 2012]. Arguably, it is very unlikely that all of our five measurements of  $\lambda$  using two different interstellar features, three different pickup ion species, and an average over 11 unique orbit permutations shows a similar systematic shift of the inflow direction. At this point, we conclude that values for the inflow direction of interstellar helium, oxygen, and neon, observed during the period between 2007 and 2010, are most likely to be in the range given by IBEX [*Möbius et al.*, 2012; *Bzowski et al.*, 2012] and by this study (Table 1).

[32] As pointed out in the introduction, the determination of the interstellar inflow direction by means of pickup ions may be affected systematically by transport effects due to asymmetric drifts according to the average Parker spiral orientation of the interplanetary magnetic field [e.g., *Möbius et al.*, 1996; *Chalov and Fahr*, 1999]. Although our two values for the inflow direction derived from the pickup ion focusing cone location lie within the uncertainty range of the values given by the IBEX team [*Möbius et al.*, 2012; *Bzowski et al.*, 2012], they show a tendency to smaller ecliptic longitudes with respect to values derived from the pickup ion crescent location. This may indicate that transport effects have a greater impact on small-scale structures, i.e., the pickup ion focusing cone, than they have on the pickup ion crescent. This would also explain why  $\lambda_{\text{He,Crescent}}$ ,  $\lambda_{\text{O,Crescent}}$ ,  $\lambda_{\text{Ne,Crescent}}$  generally show a better agreement with values from IBEX than  $\lambda_{\text{Cone}}$  from *Gloeckler et al.* [2004] and the present study. However, our values for  $\lambda_{\text{Ne,Cone}}$ ,  $\lambda_{\text{He,Cone}}$  still show a shift to higher ecliptic longitudes with respect to values from *Gloeckler et al.* [2004], which may indicate that

influences by stochastic modulations, e.g., density compressions, have a non-negligible impact on the longitudinal distribution of interstellar pickup ions at 1 AU.

[33] By including data from 2011 and 2012 in our analysis, we will be able to analyze a total of 57 different unique orbit permutations in the future, which would further reduce any systematic biases and substantially improve our analysis.

### Appendix A: Pickup Ion $w$ -Spectra

[34] For a proper analysis of pickup ion  $w$ -spectra, two important instrumental effects must be considered:

[35] (1) The observation of heavy pickup ions is limited to an energy-per-charge range of 22.6 keV/e to 74.9 keV/e, where 74.9 keV/e denotes the highest possible energy-per-charge value covered by the instrument and 22.7 keV/e the lowest energy-per-charge value that is not contaminated by a possible contribution of rare solar wind Fe<sup>3+,4+</sup>. Thus, the covered  $w$ -range is highly dynamic in terms of solar wind conditions (Figure A1), sometimes spanning a  $w$ -range between 1.2 and 2.2 during slow solar wind conditions ( $\sim 400$  km/s) and between 0.7 and 1.2 during high speed solar wind conditions ( $\sim 700$  km/s). It is further modulated by the pickup ion's mass that will shift the overall observable  $w$ -range to lower values with increasing mass. These broad variabilities complicate interpretation of pickup ion  $w$ -spectra, especially if one is interested in their temporal or angular evolution as the solar wind speed can change on short timescales.

[36] (2) The observed count rates of heavy pickup ions are modulated by the detection efficiency  $\eta(E, m)$  of the instrument. With respect to the solar wind velocity, we detect more events during high speed streams than during low speed streams [Drewns *et al.*, 2010]. Because of the frequent changes of the Microchannel Plate (MCP) voltage since March 2007, the detection efficiency,  $\eta(E, m)$ , for heavy ions is not well defined. The limited counting statistics of heavy pickup ions makes it difficult to derive accurate values for  $\eta(E, m)$  calibrated in flight. Thus, we are currently limited to observations of count rate spectra that are modulated by the instrumental response function.

[37] Influences by the instrumental behavior described in (1) and (2) complicate an interpretation of the observed data. An analysis that accounts for the instrumental behavior is in preparation and will allow us to perform a detailed analysis of pickup ion  $w$ -spectra in the future. For the sake of completeness and to give an impression of the  $w$ -information provided by PLASTIC, we will briefly summarize features visible in the observed  $w$ -spectra with consideration of the instrumental behavior.

[38] Figure A2 shows the derived  $w$ -spectra of C<sup>+</sup>, O<sup>+</sup>, Ne<sup>+</sup>, and He<sup>+</sup> accumulated over a time period of 1450 days. The count rate spectra are plotted as a function of ecliptic longitude for four superposed orbits of STEREO A. To partially suppress count rate variations of the changing solar wind speed, we applied a 28-day sliding average to the data. As already shown in Figure 3, He<sup>+</sup> shows a clear focusing cone signature (Figure A2, bottom right), which is aligned around a heliographic longitude of  $\sim 75^\circ$  with a characteristic cutoff at  $w \sim 2.0$ . Ne<sup>+</sup> (Figure A2, bottom left), which has a slightly higher ionization rate ( $3.65 \cdot 10^{-7} \text{ s}^{-1}$ ) than He<sup>+</sup> ( $1.19 \cdot 10^{-7} \text{ s}^{-1}$ ) [Cummings *et al.*, 2002], also shows a

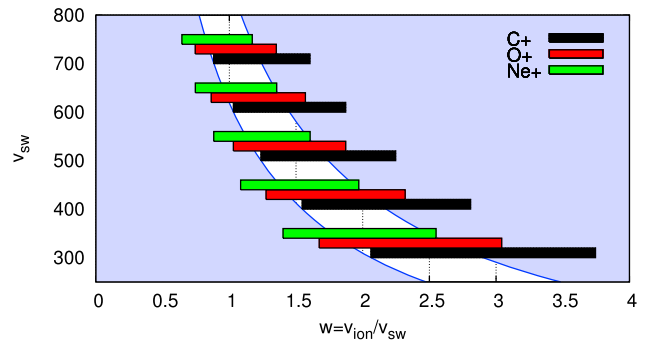


**Figure A1.** The  $w$ -coverage of C<sup>+</sup> (black), O<sup>+</sup> (red), and Ne<sup>+</sup> (green) at different solar wind speeds. Overall coverage increases and is shifted toward higher  $w$ 's with decreasing solar wind speed. The white shaded area constitutes a solar-wind-speed-dependent  $w$ -range that is likewise covered by C<sup>+</sup>, O<sup>+</sup>, and Ne<sup>+</sup>. Interstellar He<sup>+</sup>, which is not shown here, is well covered during all solar wind conditions.

focusing signature [Drewns *et al.*, 2010]. The higher ionization probability and lower abundance lead to decreased counting statistics by almost 4 orders of magnitude compared to helium and the structure is more dominated by sporadic events during beneficial solar wind conditions, e.g., high-speed streams or density compressions. Consequently, the structure, position and energy spectra of the Ne<sup>+</sup> focusing cone is more strongly affected by systematic influences.

[39] The crescent structure forms around an ecliptic longitude of  $\sim 255^\circ$  and shows a cutoff at  $w \sim 2.0$  with a wide angular spread of almost  $180^\circ$ . It is most pronounced for interstellar atoms that have high ionization rates. Of all interstellar atoms shown in Figure A2, O<sup>+</sup> (Figure A2, top right) has the highest ionization rate, with  $8.48 \cdot 10^{-7} \text{ s}^{-1}$  [Cummings *et al.*, 2002]. Consequently, the formation of the interstellar crescent is most pronounced for oxygen, while for the same reasons the formation of an interstellar oxygen focusing cone is not observed.

[40] C<sup>+</sup> (Figure A2, top left) shows, due to its inner-source origin, no clear angular distribution and its distribution is believed to be consistent with an isotropic source around the Sun [e.g., Allegrini *et al.*, 2005; Geiss *et al.*, 1996]. Deviations from an isotropic distribution, e.g., at  $\lambda_{1,2} = 270^\circ, 110^\circ$ , are likely induced by instrumental factors and solar wind modulations. A probable explanation for the observed depletion zones is an insufficient coverage in velocity space, as O<sup>+</sup> shows the same depletions but only at small  $w$ 's. The observed signature of C<sup>+</sup> mainly consists of events with  $w < 1.5$ , as expected for an inner-source pickup ion, but it also shows a clear focusing feature in this  $w$ -range. Due to the design of PLASTIC's time-of-flight chamber, ions show highly asymmetric time-of-flight distributions that have prolonged tails extending toward higher time-of-flights. These tails can induce a background to ions of higher mass-per-charges. In the case of C<sup>+</sup>, and also O<sup>+</sup> and Ne<sup>+</sup> to a lesser degree, the background is induced by He<sup>+</sup> ions. During normal conditions the impact of an extended He<sup>+</sup> time-of-flight tail is negligible for heavy pickup ions, especially considering their high mass-per-charge with respect to He<sup>+</sup>. But during passage of the focusing cone the intensity of He<sup>+</sup>

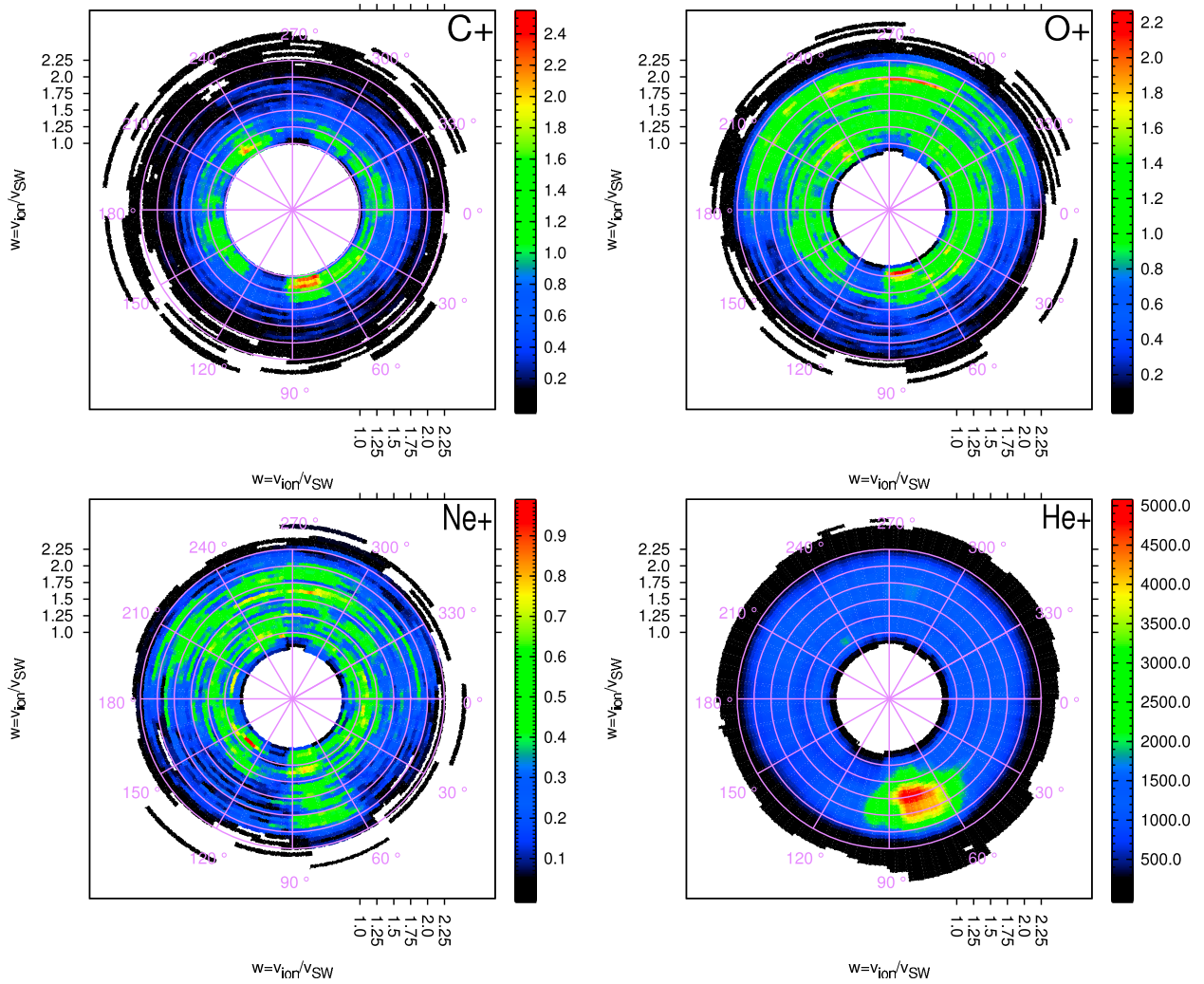


**Figure A2.** The  $w$ -spectra of  $C^+$  (top left),  $O^+$  (top right),  $Ne^+$  (bottom left), and  $He^+$  (bottom right) sorted into the respective ecliptic longitude with respect to the vernal equinox. The  $w$ -information is given by the radial distance from the plot center, whereas the innermost and outermost magenta circles correspond to a  $w$  of 1.0 and 2.25, respectively. The angle at which the data is plotted corresponds to the ecliptic longitude at which the measurement was conducted. The color represents the average number of counts that have been observed in a period of 28 days around the respective ecliptic longitude. To give an impression of the global velocity distribution of pickup ions and their dependence on the ecliptic longitude, 1450 days of STEREO A pickup ion data have been accumulated. Two prominent features are clearly resolved. The focusing cone, which is visible for  $Ne^+$  and  $He^+$ , forms around an ecliptic longitude of  $75^\circ$  with a sharp cutoff at  $w \approx 2$ , as expected for interstellar pickup ions. The interstellar crescent, which is prominent in the upwind region, spans over almost  $180^\circ$  and also shows a cutoff at  $w \approx 2$ . Both structures are believed to be symmetrically aligned around the inflow direction of interstellar neutrals.

time-of-flight distribution, and consequently its tail, increases almost by one order of magnitude. In this period, the induced  $He^+$  background is mistakenly interpreted as heavy pickup ion events of species  $X^+$ , which produces a signature of species  $X^+$  at  $w = \sqrt{m_{He^+}/m_{X^+}}$ . Consequently, a  $He^+$  background event with  $w_{He^+} = 2.0$  results in a misinterpreted event of  $C^+$ ,  $O^+$  or  $Ne^+$  at  $w = 1.15$ ,  $1.0$ , or  $0.85$  respectively. A possible  $He^+$  background will not have any significant effect on the observed signature of interstellar heavy pickup ions, which lie well above  $w = 1.5$ . As the  $He^+$  background decreases with increasing time-of-flight, its impact recedes

with increasing heavy pickup ion masses, which is consistent with our observation.

[41] **Acknowledgments.** This work was supported in part by the German Science Foundation (Deutsche Forschungsgemeinschaft) under grant Wi-2139/4-1; by the NASA STEREO mission through grant NAS5-00132; and by SR&T grant NNX09AW32G. E. Möbius gratefully acknowledges the support of the U.S. Department of Energy through LANL's Laboratory Directed Research and Development (LDRD) Program and the Institute of Geophysics and Planetary Physics.

[42] Philippa Browning thanks the reviewers for their assistance in evaluating this paper.

## References

- Allegrini, F., N. A. Schwadron, D. J. McComas, G. Gloeckler, and J. Geiss (2005), Stability of the inner source pickup ions over the solar cycle, *J. Geophys. Res.*, *110*, A05105, doi:10.1029/2004JA010847.
- Bzowski, M., et al. (2012), Neutral interstellar helium parameters based on IBEX-Lo observations and test particle calculations, *Astrophys. J. Suppl. Ser.*, *198*, 12.
- Chalov, S. V., and H. J. Fahr (1999), Signatures of the interplanetary helium cone reflected by pick-up ions, *Solar Phys.*, *187*, 123–144.
- Cummings, A. C., E. C. Stone, and C. D. Steenberg (2002), Composition of anomalous cosmic rays and other heliospheric ions, *Astrophys. J.*, *578*, 194–210.
- Drews, C., L. Berger, R. F. Wimmer-Schweingruber, A. B. Galvin, B. Klecker, and E. Möbius (2010), Observations of interstellar neon in the helium focusing cone, *J. Geophys. Res.*, *115*, A10108, doi:10.1029/2010JA015585.
- Fahr, H. J. (1974), The extraterrestrial UV-background and the nearby interstellar medium, *Space Sci. Rev.*, *15*, 483–540.
- Galvin, A. B., et al. (2008), The Plasma and Suprathermal Ion Composition (PLASTIC) investigation on the STEREO observatories, *Space Sci. Rev.*, *136*, 437–486.
- Geiss, J., G. Gloeckler, L. A. Fisk, and R. von Steiger (1995),  $C^+$  pickup ions in the heliosphere and their origin, *J. Geophys. Res.*, *100*(A12), 23,373–23,377, doi:10.1029/95JA03051.
- Geiss, J., G. Gloeckler, and R. von Steiger (1996), Origin of  $C^+$  ions in the heliosphere, *Space Sci. Rev.*, *78*, 43–52.
- Gloeckler, G., and J. Geiss (1998), Interstellar and inner source pickup ions observed with SWICS on Ulysses, *Space Sci. Rev.*, *86*, 127–159.
- Gloeckler, G., et al. (2004), Observations of the helium focusing cone with pickup ions, *Astron. Astrophys.*, *426*, 845–854.
- Hovestadt, D., et al. (1995), CELIAS – Charge, element and isotope analysis system for SOHO, *Solar Phys.*, *162*, 441–481, doi:10.1007/BF00733436.
- Klecker, B., et al. (2009), Pickup helium observations with STEREO PLASTIC A & B, paper presented at STEREO SWG 19, Pasadena, Calif., Feb. 3–5.
- Lallement, R., J. C. Raymond, J. Vallergera, M. Lemoine, F. Dalaudier, and J. L. Bertaux (2004), Modeling the interstellar-interplanetary helium 58.4 nm resonance glow: Towards a reconciliation with particle measurements, *Astron. Astrophys.*, *426*, 875–884.
- Lallement, R., E. Quémerais, J. L. Bertaux, S. Ferron, D. Koutroumpa, and R. Pellinen (2005), Deflection of the interstellar neutral hydrogen flow across the heliospheric interface, *Science*, *307*, 1447–1449.
- McComas, D. J., et al. (2004), The interstellar hydrogen shadow: Observations of interstellar pickup ions beyond Jupiter, *J. Geophys. Res.*, *109*, A02104, doi:10.1029/2003JA010217.
- Möbius, E., D. Hovestadt, B. Klecker, M. Scholer, G. Gloeckler, and F. M. Ipavich (1985), Direct observation of  $He^+$  pick-up ions of interstellar origin in the solar wind, *Nature*, *318*, 426–429.
- Möbius, E., D. Rucinski, D. Hovestadt, and B. Klecker (1995), The helium parameters of the very local interstellar medium as derived from the distribution of  $He^+$  pickup ions in the solar wind, *Astron. Astrophys.*, *304*, 505–519.
- Möbius, E., D. Rucinski, P. A. Isenberg, and M. A. Lee (1996), Determination of interstellar pickup ion distributions in the solar wind with SOHO and Cluster, *Ann. Geophys.*, *14*, 492–496.
- Möbius, E., et al. (2004), Synopsis of the interstellar He parameters from combined neutral gas, pickup ion and UV scattering observations and related consequences, *Astron. Astrophys.*, *426*, 897–907.
- Möbius, E., et al. (2010), He pickup ions in the inner heliosphere-diagnostics of the local interstellar gas and of interplanetary conditions, *Am. Inst. Phys. Conf. Ser.*, *1302*, 37–43.
- Möbius, E., et al. (2012), Interstellar gas flow parameters derived from Interstellar Boundary Explorer-Lo observations in 2009 and 2010: Analytical analysis, *Astrophys. J. Suppl. Ser.*, *198*, 11.
- Paresce, F., S. Bowyer, and S. Kumar (1974), Observations of He i 584 Å nighttime radiation: Evidence for an interstellar source of neutral helium, *Astrophys. J.*, *187*, 633–639.
- Robert, C. P., and G. Casella (2004), *Monte Carlo Statistical Methods*, 2nd ed., Springer, New York.
- Vasyliunas, V. M., and G. L. Siscoe (1976), On the flux and the energy spectrum of interstellar ions in the solar system, *J. Geophys. Res.*, *81*(7), 1247–1252, doi:10.1029/JA081i007p01247.
- Witte, M. (2004), Kinetic parameters of interstellar neutral helium. Review of results obtained during one solar cycle with the Ulysses/GAS-instrument, *Astron. Astrophys.*, *426*, 835–844.

### 4.3. Supplementary Remarks

#### 4.3.1. Performance of the Proposed Analysis

In *Drews et al.* [2012] we stated that our proposed analysis method for deriving the inflow direction of the interstellar medium (described by equation 4 and 6 in *Drews et al.* [2012]) is especially well suited for taking into account stochastic variations, which are introduced by changes of the solar wind velocity and density on short time scales. In order to prove this statement we performed several statistical tests with our analysis on artificial data sets with different modulation types. Fig. 4.2 schematically shows two different modulation types that can occur and their effect on a longitudinal structure as the focusing cone. While a stochastic modulation (as introduced by the solar wind velocity and density) can shift the focusing signature in either direction, a systematic modulation (as introduced by the efficiency decay, see section 4.3.2) will produce a shift in a defined direction.

Testing our proposed analysis method on an artificial data set (which is a basic representation of the expected longitudinal signature of interstellar pickup ions at 1 AU and was adapted from *Vasyliunas and Siscoe* [1976]) has the advantage that we exactly know the underlying model and with that the modeled inflow direction of the interstellar medium.

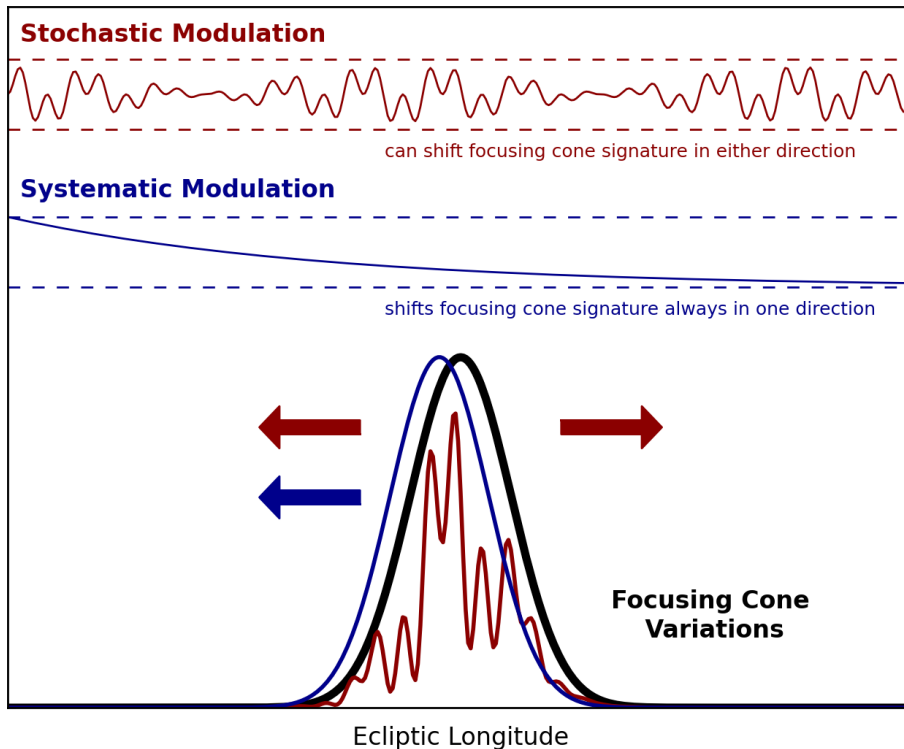


Figure 4.2.: A schematic showing the influence of two different modulations on the structure and resulting position of a longitudinal feature like the focusing cone. Stochastic modulations (red), like solar wind speed and density variations, can produce an unpredictable shift of the nominal location of the focusing cone every time it is measured. Systematic modulations (blue), like a detection efficiency decay, will produce a predictable shift of its location, but an unpredictable one if the nature of the systematic modulation is poorly known.

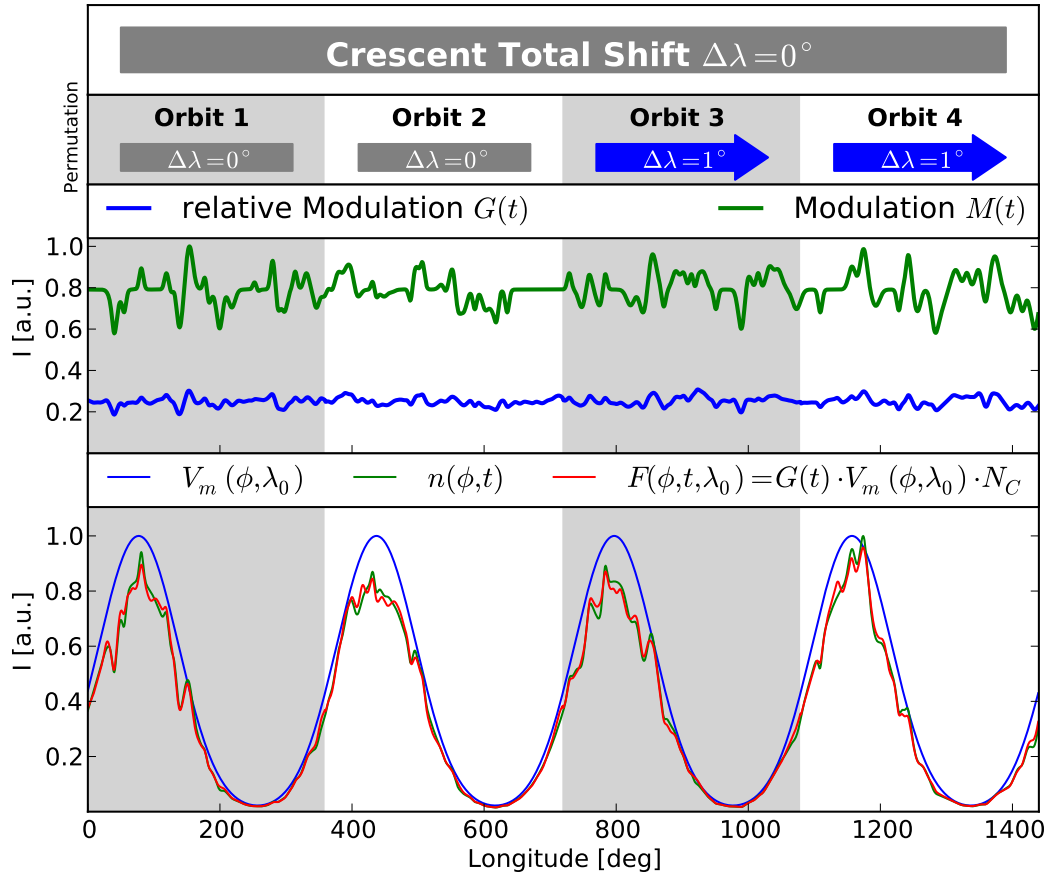


Figure 4.3.: A representation of the proposed analysis method performed on an artificial data set. The underlying model  $V_m(\phi, \lambda_0)$  is a simple representation of the interstellar crescent that is based on a cold pickup ion model originally derived by *Vasyliunas and Siscoe* [1976] (blue line, bottom panel). For a purely stochastic modulation  $M(t)$  we randomly injected 100 Gaussians of positive or negative intensity over the given longitudinal range (green line, central panel). The artificial data set  $D(\phi, t)$  is then derived by a longitudinal-wise multiplication of the underlying model  $V_m(\phi, \lambda_0)$  and the modulation  $M(t)$ ,  $D(\phi, t) = V_m(\phi, \lambda_0) \cdot M(t)$  (green line, bottom panel). With the artificial data set we can derive the relative modulation parameter  $G(t)$  (blue line, central panel) and the resulting fit function  $F(\phi, t, \lambda_0)$  (red line, bottom panel) is then used to derive the most likely longitudinal position of the crescent, which is shown in the top panel as an absolute offset with respect to the original crescent location. The second panel from the top shows the absolute offset for each orbit separately.

We can further apply different modulation types to our artificial data set and study how our analysis method performs under varying conditions. Fig. 4.3 shows such a study on the longitudinal signature of the interstellar crescent for an exemplary modulation parameter  $M(t)$  (green curve, center panel). In order to quantify the overall performance of the proposed analysis method we generated 1500 artificial data sets, as described in Fig. 4.3, for four different types of modulations and compared our method (described by equation 4 and 6 in *Dreus et al.* [2012]) with a simple fit of the expected model  $V_m(\phi, \lambda_0)$  to the artificial data sets. The results are shown in Fig. 4.4. The different modulation

parameters  $M(t)$  are

- top-left panel: Injection of 100 Gaussians of randomly chosen intensity, location, and width onto a constant function
- top-right panel: Injection of 200 Gaussians of randomly chosen intensity, location, and width onto a constant function
- bottom-left panel: Injection of 100 Gaussians of randomly chosen intensity, location, and width onto a constant function that has 100 randomly distributed data gaps.
- bottom-right panel: Injection of 100 Gaussians of randomly chosen intensity, location, and width onto the instrumental efficiency decay.

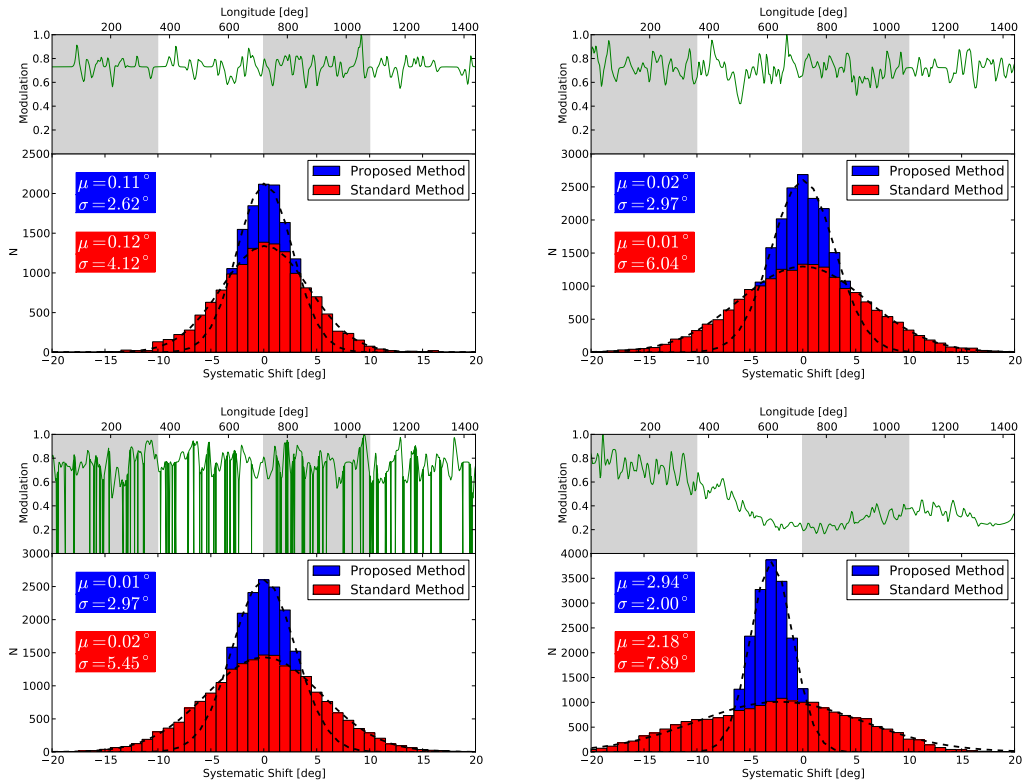


Figure 4.4.: Four different types of modulation are used to compare the proposed method described with a standard method ( $G(t)=1$ ). In each figure the top panel shows the modulation  $M(t)$ . The bottom panels show histograms of the longitudinal position of the crescent as an absolute offset with respect to the original crescent location. The histograms contain the results of the proposed method (blue) and standard method (red) performed on 1500 artificial data sets (based on  $M(t)$ ) and each possible orbit combination.  $\mu$  and  $\sigma$  are the averages and standard deviations of the shown distributions and can be used as an indicator for the overall performance of both methods. While both methods seem to be able to reproduce the original crescent location for the average of 1500 different artificial data sets, our proposed method shows considerably smaller standard deviations and is therefore more precise.

### 4.3.2. Systematic Influences

In this chapter we discuss two relevant systematic influences that may introduce a bias to our measurement of the inflow direction of the interstellar medium. The most influential bias is aging of the instrument, which causes a slowly decaying detection efficiency over time. The decrease of the detection efficiency is mainly caused by aging of the Micro Channel Plates (MCPs), which are responsible for the amplification of the electron signal used for the time-of-flight measurement. If the amplification is not sufficient, the probability to trigger a valid time-of-flight signal decreases along with the overall detection efficiency. To some degree it is possible to counteract the aging effect by increasing the voltage applied to the MCPs as was done several times throughout the mission. This procedure, however, not only increases the overall detection efficiency but causes the detection efficiency to be a complicated function in time. Therefore, it is crucial to derive the time-dependent detection efficiency in-flight in order to give a profound estimate of its influence on the measurement of the inflow direction of the interstellar medium. The second systematic bias involves influences by STEREO A's eccentric orbit around the Sun and is discussed at the end of this chapter.

#### Efficiency Decay

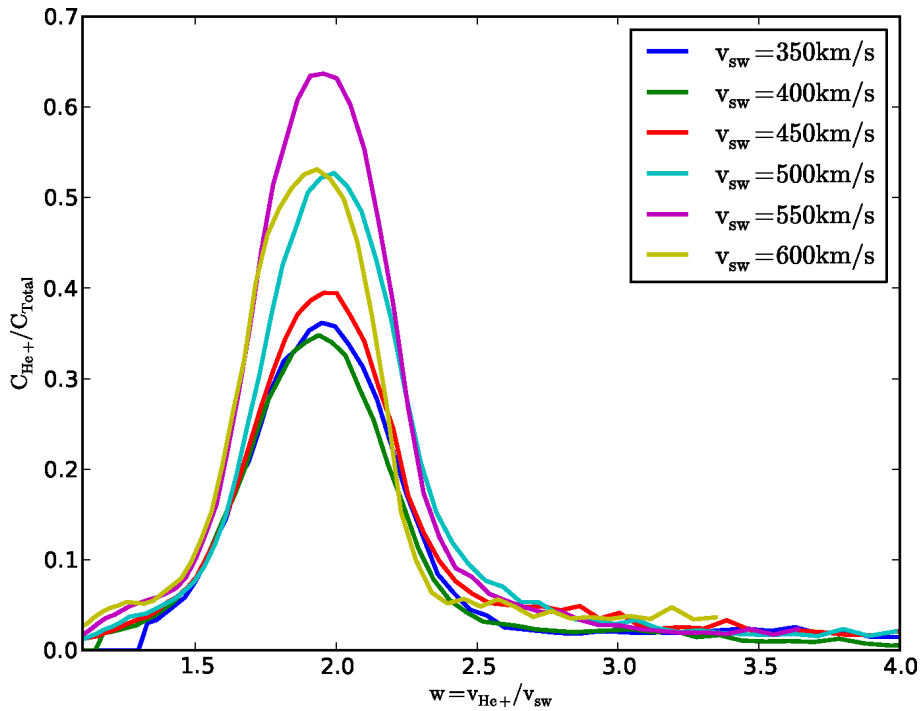


Figure 4.5.: All available data between February, 2007 and January, 2010 was accumulated to derive the ratio of the  $\text{He}^+$  box rate  $C_{\text{He}^+}$  (DCR & TCR) to total counts  $C_{\text{Total}}$  for different solar wind speeds  $v_{sw}$ . The ratio is plotted against the relative  $\text{He}^+$  velocity  $v_{\text{He}^+}$  with respect to  $v_{sw}$ .  $C_{\text{He}^+}/C_{\text{Total}}$  shows a maximum at around  $w \sim 2$  which, depending on  $v_{sw}$ , translates into different instrumental energy-per-charge steps.

In order to quantify influences of instrumental aging on our measurements of the inflow



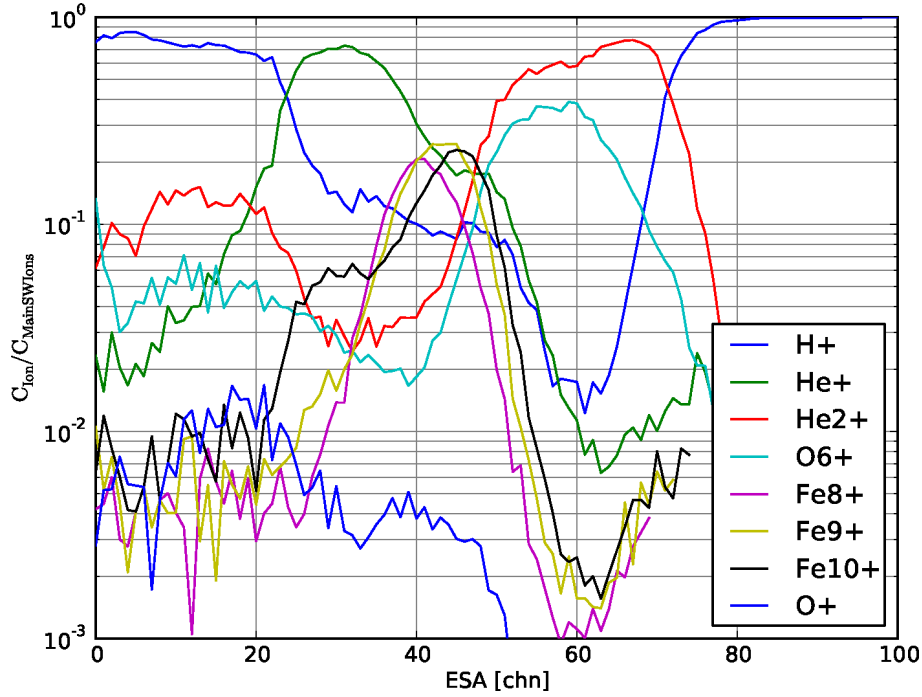


Figure 4.6.: The ratio of different solar wind and pickup ion box rates  $C_{\text{Ion}}$  with respect to  $\sum C_{\text{Ion}} = C_{\text{MainSWIons}}$  is plotted against instrumental energy-per-charge steps. Only data with  $v_{sw} \sim 500$  km/s has been used for this figure.  $\text{H}^+$ ,  $\text{He}^+$ ,  $\text{He}^{2+}$ , as well as  $\text{Fe}^{8+}$  and  $\text{Fe}^{9+}$  to some extent, have an energy-per-charge range where the respective ion dominates with respect to  $C_{\text{MainSWIons}}$ . Heavy pickup ions (labeled  $\text{O}^+$ ) account at most for  $\sim 2\%$  of the accumulated box rates. Due to PLASTIC's priority scheme and Main- to Small-channel switch the ratios not necessarily reflect the actual solar wind composition.

direction of the interstellar medium, we follow an approach of *Klecker* [2009] that uses housekeeping data of PLASTIC to estimate the  $\text{He}^+$  efficiency on a daily basis. The total instrumental detection efficiency can be approximated by

$$\epsilon_{\text{Total}} = \epsilon_{\text{Start}} \times \epsilon_{\text{Stop}} \times \epsilon_{\text{Valid}}, \quad (4.1)$$

where  $\epsilon_{\text{Start}}$  and  $\epsilon_{\text{Stop}}$  are the probabilities for particles to trigger a time-of-flight start- and stop-signal and  $\epsilon_{\text{Valid}}$  the probability for particles to trigger a valid event, e.g. events for which  $\tau_{\text{start}} < \tau_{\text{end}}$ . This approximation can now be used to derive  $\epsilon_{\text{Total}}$  by replacing the expressions of  $\epsilon_{\text{Start}}$ ,  $\epsilon_{\text{Stop}}$ ,  $\epsilon_{\text{Valid}}$  with suited approximations in form of ratios of the corresponding housekeeping rates

$$\epsilon_{\text{Total}}(E/q) = \text{SFO}/\text{RA} \times \text{SFR0}/\text{SFO} \times \text{VALID}/\text{SFR0} \quad (4.2)$$

$$= \text{VALID}/\text{RA}(E/q). \quad (4.3)$$

Here  $\text{SFO}$  denotes the  $\tau$ -start rate,  $\text{SFR0}$  the  $\tau$ -stop rate,  $\text{VALID}$  the  $\tau$ -valid rate, and  $\text{RA}$  the total rate registered by PLASTIC's restive anode. Here it is important to note, that  $\text{RA}$  is assumed to measure with 100% efficiency, i.e. all particles that enter the time-of-flight chamber are counted by  $\text{RA}$ . The next step is to derive from  $\epsilon_{\text{Total}}$  the detection efficiency

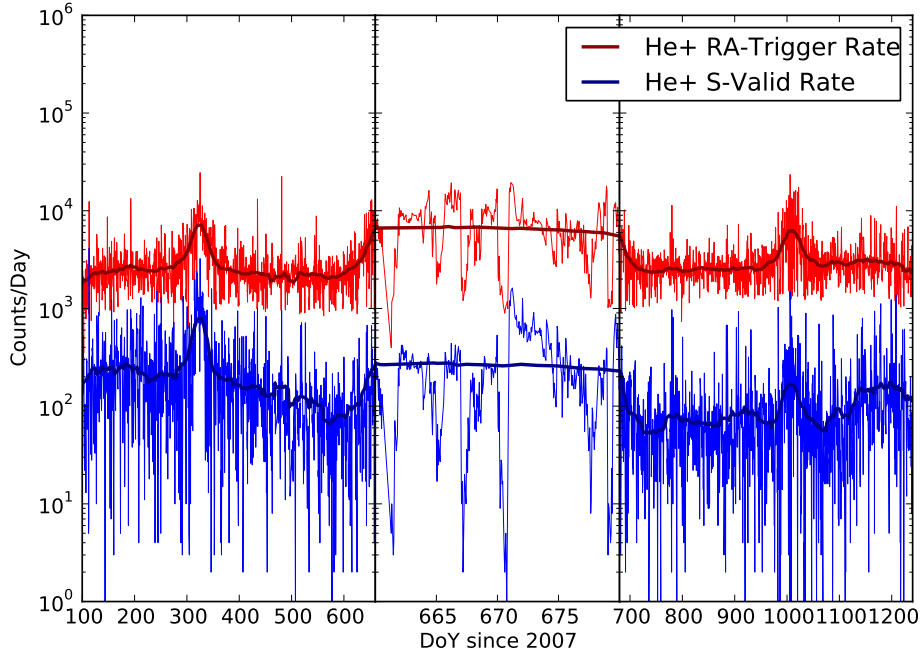


Figure 4.7.: Shown is the RA (red) and VALID rate (blue) at ESA steps where  $v_{\text{He}^+} \sim 2 \cdot v_{\text{sw}}$ , i.e. the energy-per-charge range, where  $\text{He}^+$  is the most abundant of all solar wind and pickup ions. The thick solid lines are 27-day sliding averages of the respective rates. Note that the center panel shows a magnified view of the period between DoY 660 and 680.

of  $\text{He}^+$ . Both VALID and RA are available for each instrumental energy-per-charge step separately within a time resolution of 5 minutes. By choosing only instrumental energy-per-charge steps in equation 4.3, where  $\text{He}^+$  is the dominant species with respect to the solar wind composition, we can achieve a basic species classification, that allows us to derive  $\epsilon_{\text{He}^+}$ . Fig. 4.5 shows the ratio of  $\text{He}^+$  counts  $C_{\text{He}^+}$  to total counts  $C_{\text{Total}}$  (taken from PHA data) as a function  $w = v_{\text{He}^+}/v_{\text{sw}}$  for different solar wind velocities. At instrumental energy-per-charge steps where  $\text{He}^+$  has a velocity of  $w \sim 2.0$ , at least 30% of all incident events are attributed to  $\text{He}^+$ . The remaining events are mostly attributed to instrumental noise and to some extent also solar wind  $\text{H}^+$ . In Fig. 4.6 we show the ratio of  $C_{\text{ion}}$  with respect to  $\sum C_{\text{Ion}}$  for  $\text{H}^+$ ,  $\text{He}^+$ ,  $\text{He}^{2+}$ ,  $\text{O}^{6+}$ ,  $\text{Fe}^{8+}$ ,  $\text{Fe}^{9+}$ ,  $\text{Fe}^{10+}$ , and  $\text{O}^+$  as a function of the instrumental energy-per-charge step at a constant solar wind velocity of  $v_{\text{sw}} \sim 500\text{km/s}$ . It is evident that a species classification solely based on the  $E/q$  information is only suitable for a fraction of ions, i.e. ions which clearly dominate a certain  $E/q$  range like  $\text{H}^+$ ,  $\text{He}^+$ , and  $\text{He}^{2+}$ . For heavy pickup ions, e.g.  $\text{O}^+$ , it is impossible to find an energy-per-charge range, where the respective ion dominates. Consequently, this approach is unsuitable to derive the time dependent detection efficiency of heavy pickup ions. However, as was discussed in *Drews et al. [2012]*  $\epsilon_{\text{He}^+}$  may be used as an approximation for the time dependent detection efficiency of heavy pickup ions as they are not as strongly affected by aging of the MCPs.

Finally, Fig. 4.7 shows the  $\text{He}^+$  VALID and RA rate as a function of time, which are used to infer the time dependent detection efficiency function  $\epsilon_{\text{He}^+}$  shown in Fig. 4.8. Although  $\epsilon_{\text{He}^+}$  shows a relatively continuous decline with time during the first 500 days,

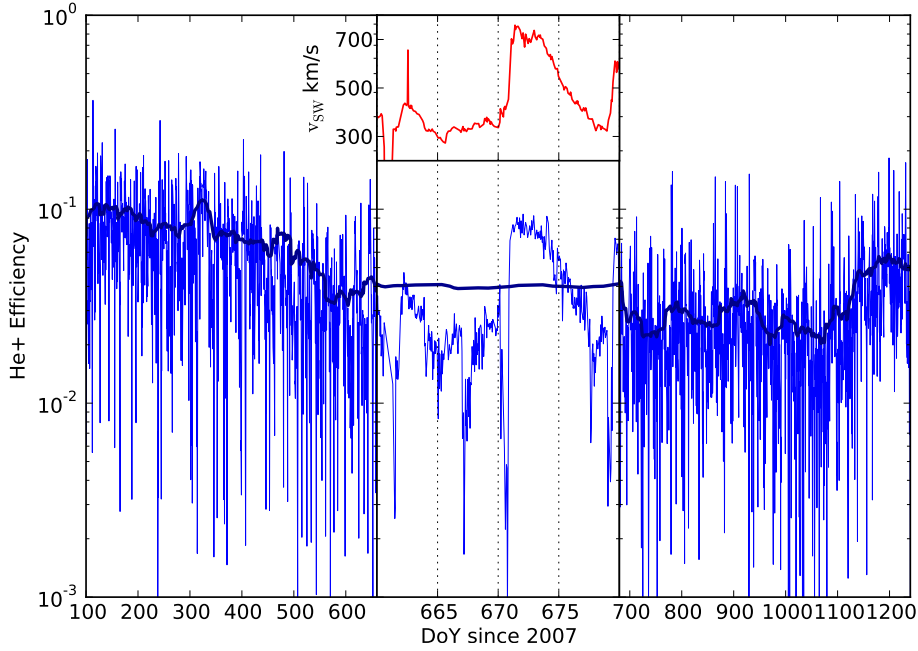


Figure 4.8.: The  $\text{He}^+$  efficiency  $\epsilon_{\text{He}^+}$  versus day since 2007 is shown. The thick blue lines denotes a 27-day sliding average of the data. The center panel shows a magnified view of  $\epsilon_{\text{He}^+}$  in a period between DoY 660 and 680 together with the solar wind speed (top panel). It appears that  $\epsilon_{\text{He}^+}$  follows the same trend as  $v_{sw}$ .

it is obvious that the  $\text{He}^+$  efficiency function is superposed by many small- as well as large-scale variations. The latter, i.e. increase at Doy  $\sim 500, 800, 900$ , and  $1100$ , are caused by increases of the instrumental MCP bias voltage, which leads to a quick increase of  $\epsilon_{\text{He}^+}$  that is then slowly declining to its original value. The aforementioned small scale variations are introduced by the concurrent solar wind velocity. During high speed solar wind, particles have a higher energy and therefore higher probability to trigger a  $\tau$ -start and  $\tau$ -stop signal. As a result, the shape of  $\epsilon_{\text{He}^+}$  closely follows that of  $v_{sw}$  as illustrated in the center panel of Fig. 4.8. In order to estimate the systematic influence of  $\epsilon_{\text{He}^+}$  on our results for the inflow direction of the interstellar medium, we follow the approach described in Fig. 4.3 and used the 27-day sliding average of  $\epsilon_{\text{He}^+}$  (see Fig. 4.8) as our modulation parameter  $m(t)$ . This allows us to determine the systematic bias on the longitudinal position of the crescent and focusing cone (see Fig. 4.9, left and right panel respectively). We further repeated this analysis for a smoothed  $\text{He}^+$  efficiency function (approximated by a polynomial), which is shown in Fig. 4.10. In either case, influences on the longitudinal position of the focusing cone are  $\sim -0.3^\circ$ . The determined crescent location is shifted by  $\sim -1.7^\circ$  for the 27-day average and  $\sim -2.8^\circ$  for the smoothed  $\text{He}^+$  efficiency function with respect to the underlying model. We note that our values for the systematic influences on the longitudinal position of the focusing and crescent for the 27-day averaged  $\text{He}^+$  efficiency decay slightly differ from the values given in *Drewns et al.* [2012] ( $\Delta\lambda_{\text{Cone}} = 1^\circ$ ,  $\Delta\lambda_{\text{Crescent}} = -1^\circ$ ). In *Drewns et al.* [2012]  $\epsilon_{\text{He}^+}$  was determined on a daily basis, while in this study we determined  $\epsilon_{\text{He}^+}$  with one hour time resolution, which allowed us to determine the respective  $E/q$  ranges at a given solar wind speed in which  $\text{He}^+$  dominates more precisely.

### 4.3. SUPPLEMENTARY REMARKS

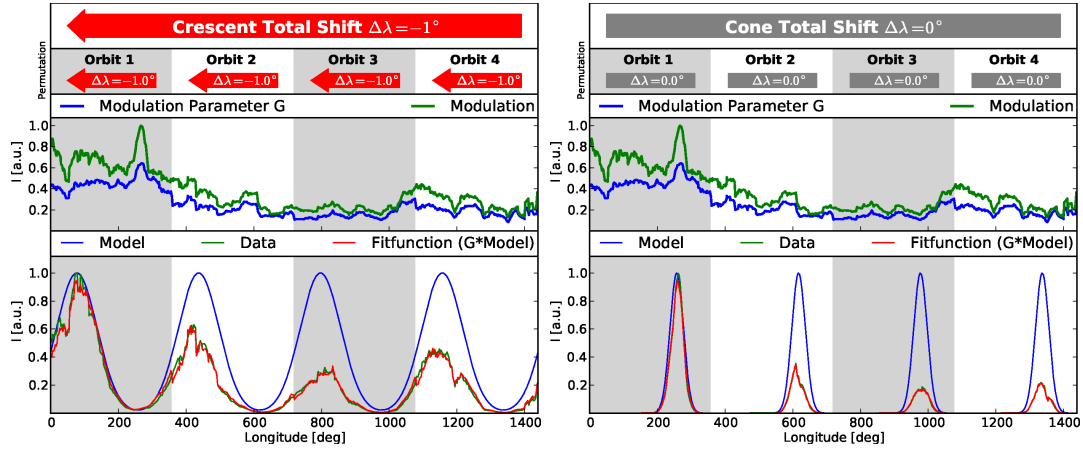


Figure 4.9.: The systematic shift of the crescent and cone position (left and right figure respectively) induced by the  $\text{He}^+$  efficiency decay (see Fig. 4.8) is shown. The most likely systematic shift is derived by an average of all possible orbit combination in accordance with our results for the most likely inflow direction (see chapter 4 Fig. 5) and yields  $\Delta\lambda_{\text{Cone}} = -0.3^\circ \pm 1.4^\circ$  and  $\Delta\lambda_{\text{Crescent}} = -1.7^\circ \pm 6.1^\circ$ . Here only the combination of four orbits is shown. The remaining orbit combinations can be found in appendix A.

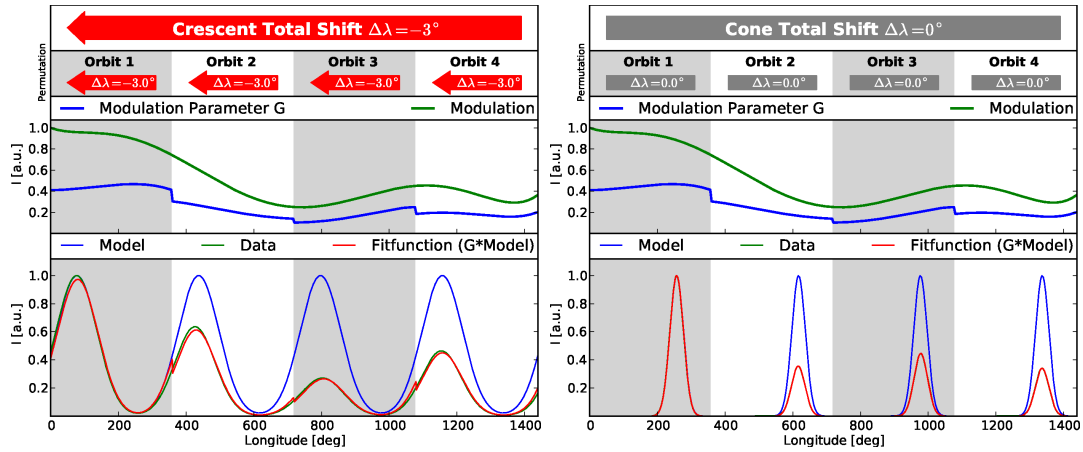


Figure 4.10.: The systematic shift of the crescent and cone position (left and right figure respectively) induced by a smoothed  $\text{He}^+$  efficiency decay is shown. The most likely systematic shift is derived by an average of all possible orbit combination in accordance with our results for the most likely inflow direction (see chapter 4 Fig. 5) and yields  $\Delta\lambda_{\text{Cone}} = -0.3^\circ \pm 0.5^\circ$  and  $\Delta\lambda_{\text{Crescent}} = -2.8^\circ \pm 2.4^\circ$ . Here only the combination of four orbits is shown.

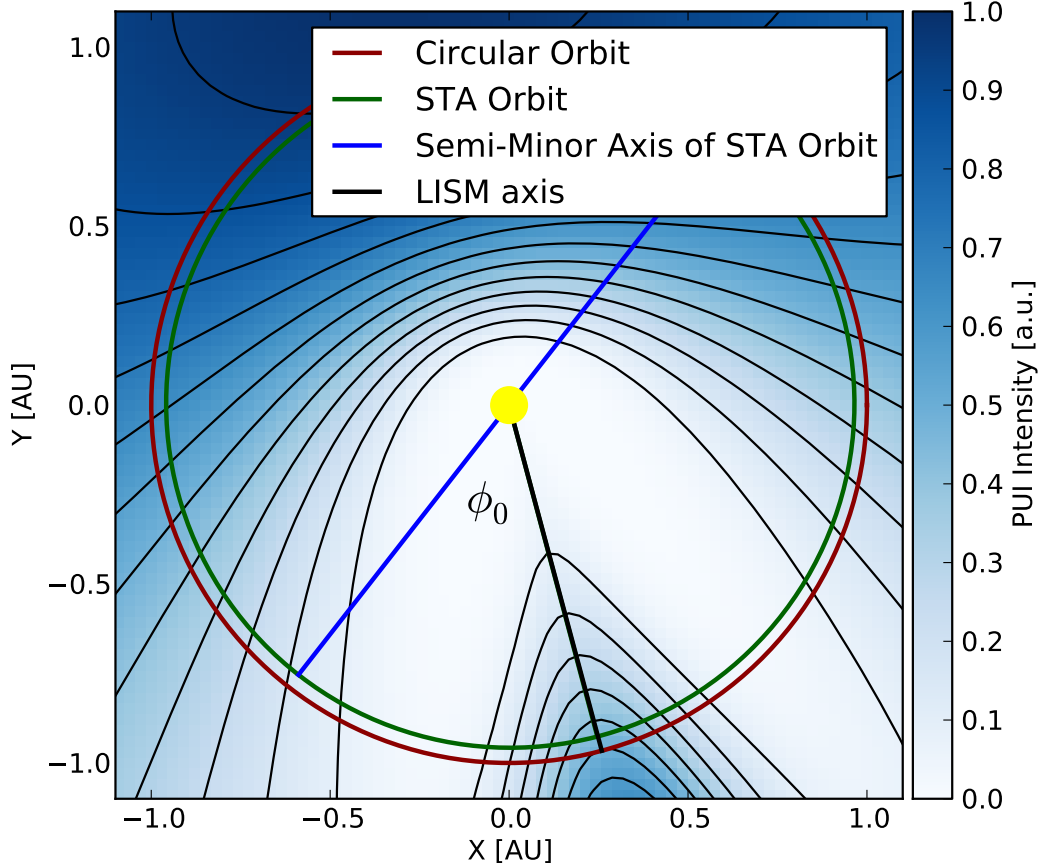
**Orbit Eccentricity**


Figure 4.11.: Orbit of STEREO A (green) compared to a circular orbit (red) around the Sun. The color coded contour in the background shows the expected  $O^+$  density (in arbitrary units) within a  $2 \times 2$  AU area centered around the Sun. The model used here is based on the cold pickup ion model by *Vasyliunas and Siscoe* [1976]. The crescent and focusing cone are aligned along the inflow axis of the local interstellar medium (black line), which in this model is set to  $\lambda_{\text{ISM}} = 75^\circ$ . The orbit of STEREO A is slightly eccentric, which causes a relative distance variation from the Sun of  $\sim 1\%$ . Furthermore, the semi-minor axis (blue line) of STEREO A's orbit is not aligned with the LISM axis, which introduces a measurable systematic bias to our measurement of  $\lambda_{\text{ISM}}$ .

In order to estimate the systematic influence of the eccentricity of STEREO A's orbit on our measurement of  $\lambda_{\text{ISM}}$ , we calculated the expected longitudinal distribution of  $O^+$ ,  $Ne^+$ , and  $He^+$  (derived from a cold pickup ion model [*Vasyliunas and Siscoe*, 1976]) as seen from STEREO A. In this model, the interstellar medium is coming from an ecliptic longitude of  $\lambda_{\text{ISM}} = 75^\circ$ . The eccentric orbit of STEREO A is shown in Fig. 4.11 together with the cold  $O^+$  pickup ion model as a color coded contour in the background. The combination of the orbit's eccentricity and the fact that the semi-minor axis of STEREO A's orbit is not aligned with the axis of the inflowing interstellar medium, causes the maxima of the focusing cone and crescent to be shifted with respect to  $\lambda_{\text{ISM}}$ .

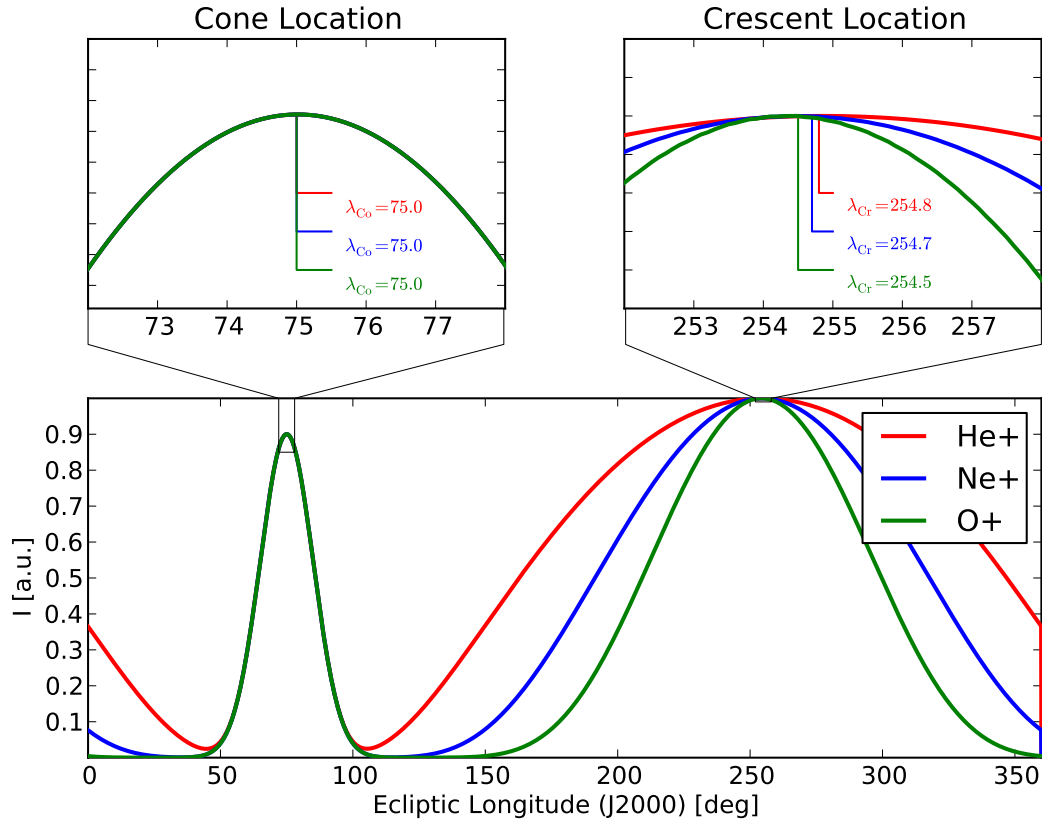


Figure 4.12.: Expected longitudinal distribution of  $O^+$  (green),  $Ne^+$  (blue), and  $He^+$  (red) as seen from STEREO A (bottom panel). The top left and right panel show a magnified view of the focusing cone and crescent passage respectively. Due to STEREO's eccentric orbit both signatures appear to be slightly asymmetric as seen from PLASTIC, which introduces a measurable systematic bias to our measurement of  $\Delta\lambda_{He,Crescent} = -0.2^\circ$ ,  $\Delta\lambda_{O,Crescent} = -0.5^\circ$ ,  $\Delta\lambda_{Ne,Crescent} = -0.3^\circ$ . Effects on the location of the focusing cone, however, are due to its small width negligible.

The corresponding longitudinal distribution for  $He^+$ ,  $O^+$ , and  $Ne^+$  as seen from STEREO A are shown in Fig. 4.12. Because the focusing cone only spreads over a few degrees we can not resolve any systematic influence from the eccentricity of STEREO A's orbit. The crescent location on the other hand is indeed influenced by the eccentricity due its wider spread over almost 180 degrees. The systematic influences also scale with the ionization potential of the former interstellar neutral and is stronger for particles with lower ionizations potentials such as oxygen. By finding the location of the maxima of the crescent and focusing cone and comparing them with the original inflow direction  $\lambda_{ISM}$  of the underlying model, we estimate the systematic influence of the eccentricity to be  $\Delta\lambda_{He,Crescent} = -0.2^\circ$ ,  $\Delta\lambda_{O,Crescent} = -0.5^\circ$ ,  $\Delta\lambda_{Ne,Crescent} = -0.3^\circ$ . Effects on the location of the focusing cone, however, are due to its small width negligible. To incorporate this effect, values for the crescent location have been corrected towards higher ecliptic longitudes throughout our publication in section 4.2.

# 5. Pitch-Angle Distributions of Pickup Ions

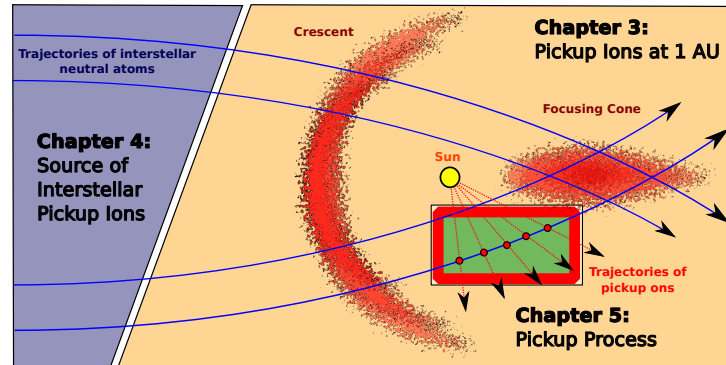


Figure 5.1.: This chapter discusses the kinetic properties of interstellar pickup ions directly after their ionization (green shaded area).

## 5.1. Introduction

### Chapter Overview

This chapter covers our third publication "Interstellar  $\text{He}^+$  Ring-Beam Distributions: Observations and Implications", which has been accepted for publication in Geophysical Research Letters in March 2013 [Drews *et al.*, 2013]. The paper was supervised by Dr. Lars Berger and Prof. Robert Wimmer-Schweingruber, who were involved in all scientific discussions and added greatly to the overall quality of the publication. The 1<sup>st</sup> author, Christian Drews, contributed  $\sim 85\%$  of the performed study. In section 5.2 the current draft of the publication is presented. Section 5.3 contains supplementary material covering a detailed description of the Virtual Detector - a tool that is used to predict the expected three dimensional count rate-spectra as seen by PLASTIC from any given model-based velocity distribution function.

### Abstract of Publication

We report systematic measurements of the distribution of the incident angle of interstellar pickup  $\text{He}^+$  ions as observed by STEREO/PLASTIC. We have organized these observations according to the concurrent angle between the Interplanetary Magnetic Field (IMF),  $\vec{B}$ , and bulk solar wind velocity,  $v_{\text{sw}}^{\vec{}}$ . Our measurements show clear evidence of a relatively local injection of pickup ions into the solar wind, which are then seen as a ring distribution perpendicular to  $\vec{B}$ . Changes of the spectral slope and flux of interstellar  $\text{He}^+$  during radial IMF configurations, as observed by e.g. Ulysses/SWICS, CELIAS/CTOF, AMPTE/SULEICA, have been continuously attributed to ineffective scattering across  $90^\circ$

pitch-angle. Our observation of the instantaneous pitch-angle distribution of interstellar  $\text{He}^+$  suggest that these changes are instead a result of locally injected pickup ions that simply escape detection for IMF configurations in which PLASTIC, as well as SWICS, CTOF, SULEICA, are not sensitive to the measurement of the locally injected pickup ions ring.

## 5.2. Publication



# Interstellar He<sup>+</sup> Ring-Beam Distributions: Observations and Implications

Christian Drews<sup>1</sup>, Lars Berger<sup>1</sup>, Robert F. Wimmer-Schweingruber<sup>1</sup>, Antoinette B. Galvin<sup>2</sup>

**Abstract.** We report systematic measurements of the distribution of the incident angle of interstellar pickup He<sup>+</sup> ions as observed by STEREO/PLASTIC. We have organized these observations according to the angle spanned by the Interplanetary Magnetic Field (IMF),  $\vec{B}$ , and the bulk solar wind velocity,  $v_{sw}^{\vec{}}$ . Our measurements show clear evidence of a relatively local injection of He<sup>+</sup> pickup ions into the solar wind, which are then seen as a ring distribution perpendicular to  $\vec{B}$ . Changes of the spectral shape and a reduced flux of interstellar He<sup>+</sup> during radial IMF configuration, as observed by e.g. Uylsses/SWICS, CELIAS/CTOF, AMPTE/SULEICA, have generally been attributed to inefficient scattering across 90° pitch-angle. Our observations of the pitch-angle distribution of interstellar He<sup>+</sup> suggest that these changes are instead a result of locally injected pickup ions that escape detection for IMF configuration in which the Solar Wind Sector of PLASTIC, as well as SWICS, CTOF, and SULEICA, are not sensitive to the measurement of the locally injected pickup ion ring.

## 1. Introduction

Interstellar pickup ions are created when inflowing interstellar neutral atoms get ionized by solar UV radiation, charge exchange with solar wind protons, or, more rarely, electron impact. Once ionized, they feel the electromagnetic force due to the Interplanetary Magnetic Field (IMF), which is frozen into the magnetized solar wind. This leads to a gyro orbit motion around the ion's guiding-center. In the following discussion, we neglect the small influence of the velocity of interstellar neutrals ( $v_{ISM} \sim 25$  km/s), that would slightly alter the observed speed  $v_P$  of pickup ions after their injection. Their initial velocity,  $v_P$ , after the injection process depends on the magnetic field orientation and follows  $v_P = \cos(B_\phi) \cos(B_\theta) v_{sw}$ , where  $B_\phi$  and  $B_\theta$  are the in-ecliptic and out-of-ecliptic magnetic field angles with respect to  $v_{sw}^{\vec{}}$ , the predominant solar wind velocity vector. This means that during radial magnetic field configurations ( $B_\phi, B_\theta=0$ ) pickup ions have, in a close-to resting frame of reference (e.g., an Earth-orbiting observer), a velocity of  $v_P = 0$  and can not be detected (e.g. [Gloeckler et al., 1995], [Isenberg, 1997]). In Fig. 2 an illustration of the initial ring-beam distributions of freshly ionized helium for three non-radial magnetic field orientations is shown (arrows, red:

$B_\phi = 45^\circ$ , blue:  $B_\phi = 67^\circ$ , black:  $B_\phi = 90^\circ$ ). Directly after their ionization, pickup ions are moving on gyro orbits perpendicular to  $\vec{B}$ , which in Fig. 2 are shown as thick dashed lines in velocity space with respect to the solar wind bulk. Note, that only the projection onto the ecliptic plain of the ring-beam distributions is shown, which in three dimensions would be a two dimensional ring perpendicular to  $\vec{B}$  with a radius of  $v_P$ . Due to PLASTIC's limited angular acceptance in the ecliptic plane (grey shaded area in Fig. 2) the initial ring-beam distribution can only be observed during magnetic field orientations where  $67^\circ < |B_\phi| < 113^\circ$ .

After the injection, the pickup ion population radially diverges with the solar wind and appears to cool adiabatically with a cooling index of  $\gamma = 1.35 \pm 0.2$  similar to an expanding ideal gas (e.g. [Saul et al., 2009], [Vasyliunas & Siscoe, 1976]). However, the nature of this deceleration is not yet understood and still under debate. Vasyliunas & Siscoe [1976] also assumed that the initial anisotropic ring-beam distribution is quickly scattered into an almost isotropic shell distribution in the solar wind frame. Recent studies by e.g. Gloeckler et al. [1995] and Möbius et al. [1998] have found that this assumption may not be exact, as the overall observed pickup flux depends on the magnetic field direction as well as the power in magnetic wave fluctuations [Saul et al., 2007]. A "Hemispheric Model" proposed by Isenberg [1997] and a "Two-Stream Model" proposed by Möbius et al. [1998], that both introduced the assumption of ineffective scattering of interstellar pickup ions across 90° pitch-angle, allowed to explain most of the found dependencies of the pickup ion flux and velocity distribution function on the magnetic field configuration. They also found that pickup ions are generally not immediately isotropized and can have mean free paths as large as 1 AU.

In order to provide observational evidence for these models, a direct measurement of the velocity vector  $v_P^{\vec{}}$  of interstellar pickup ions is required [Saul et al., 2007]. To our knowledge, the only study able to support these models with observations of  $v_P^{\vec{}}$  is by Oka et al. [2002]. Using data from the plasma and magnetic field experiments aboard GEOTAIL they were able to show that the velocity distribution function of interstellar He<sup>+</sup> pickup ions sometimes resembles the form of a torus, which in the literature is often referred to as "ring-beam distribution". They also found that the occurrence rate of this torus-shape velocity distribution function is linked to the magnetic field direction and turbulence levels similar to what was observed in [Saul et al., 2007] for the pickup ion flux. Unfortunately, their observations lack the required angular resolution and collection power to resolve the relation between  $v_P^{\vec{}}$  and the IMF  $\vec{B}$  and thus could not provide conclusive evidence for the aforementioned pickup ion models. Other instruments were also unable to provide the required measurements of  $v_P^{\vec{}}$  with sufficient collection power (ACE) or angular resolution (CTOF, which also lacks a co-located IMF measurement).

Here we report observations of the instantaneous pitch-angle distribution of He<sup>+</sup> during intermediate cases of quasi-perpendicular and -parallel IMF configurations with respect

<sup>1</sup>Institute for Experimental and Applied Physics, Christian-Albrechts-University Kiel, Germany

<sup>2</sup>Space Science Center & Department of Physics, University of New Hampshire, New Hampshire

to  $v_{\text{sw}}^-$ . This has allowed us to fill the aforementioned gap and to reveal for the first time the relation between  $v_{\vec{p}}$  and  $\vec{B}$ . Our result questions the prevalent assumption that ineffective scattering across 90° pitch-angle leads to the changes of the flux and spectral shape of interstellar He<sup>+</sup> during quasi-radial IMF orientations as was observed by Isenberg [1997], Saul et al. [2007], and Möbius et al. [1998].

## 2. Instrumentation and Data Acquisition

In this study we report on observations of He<sup>+</sup> pickup ions with the PLASMA and SupraThermal Ion Composition (PLASTIC) instrument [Galvin et al., 2008] aboard the Solar TErrestrial Observatory Ahead (STEREO A) during varying alignments of the IMF vector  $\vec{B}$ . PLASTIC is a time-of-flight mass spectrometer and combines measurements of the particle's energy  $E$ , time-of-flight  $\tau$ , and energy-per-charge  $E/q$  to determine its mass  $m_{\text{ion}}$ , charge  $q_{\text{ion}}$ , and velocity  $v_{\text{ion}}$ . Our following analysis is performed with the Solar Wind Section (SWS) of PLASTIC, which is centered around the line connecting the Sun and the spacecraft. In azimuthal direction it utilizes a resistive anode to distinguish between 32 different incident angles of particles in form of 32 angular bins that are linear spaced in the range of  $\alpha_{\text{acc}} = \pm 22.5^\circ$  with a width of  $1.4^\circ$  each. In polar direction an electrostatic deflection system is used to determine the out-of-ecliptic incident angle of particles, which again are binned into 32, so-called, deflection steps that are linear spaced in the range  $\beta_{\text{acc}} = \pm 20.0^\circ$  with a width of  $1.3^\circ$  each. In total, the SWS of PLASTIC covers  $\sim \pi/2$  steradians and is able to resolve angular features  $> 1.3^\circ$  - a key feature for the following analysis.

Following the approach of Drews et al. [2012] we use Pulse Height Analysis data to create a consolidated He<sup>+</sup> count rate that contains for each incident He<sup>+</sup> measurement information on its in- and out-of-ecliptic incident angle ( $\alpha, \beta$ ), its velocity  $v_{\text{ion}}$ , the averaged solar wind speed  $v_{\text{sw}}$ , and the averaged IMF direction ( $B_\phi, B_\theta$ ) within 5 minutes intervals. With  $v_{\text{ion}}$  and  $v_{\text{sw}}$  we can derive the dimensionless quantity  $w = v_{\text{ion}}/v_{\text{sw}}$ , which denotes the total velocity of He<sup>+</sup> with respect to  $v_{\text{sw}}$  in a resting frame of reference (see Fig. 2). However, with respect to the solar wind bulk velocity pickup ions are initially injected onto a spherical shell with  $r = v_{\text{sw}}$  (black circle, Fig. 2) at  $w = 0$  where they are forced into a gyro motion around  $\vec{B}$  resulting in the characteristic pickup ion ring distributions (thick dashed lines, Fig. 2). The relative velocity of pickup ions with respect to the outward flowing solar wind package  $w_{\text{sw}}$  is then given by

$$w_{\text{sw}} = \sqrt{w^2 - 2 \cdot w \cdot \cos(\alpha) \cos(\beta) + 1}, \quad (1)$$

as illustrated in Fig. 2. Here  $\alpha$  denotes the in-ecliptic and  $\beta$  the out-of-ecliptic incident angle of the ion.

We obtained the average in- and out-of-ecliptic IMF angles  $B_\phi$  and  $B_\theta$  with 1 minute time resolution ( $B_\phi$  is defined in Fig. 2,  $-90^\circ < B_\theta < 90^\circ$  is measured from the ecliptic plane) from the Magnetometer of the In-situ Measurements of Particles and CME Transients (IMPACT) instrument suite [Acuña et al., 2008] aboard STEREO A. We performed our analysis on the quiet solar wind observed between March 2007 and December 2009. In order to derive He<sup>+</sup>  $w$ -spectra as a function of the in-ecliptic magnetic field angle  $B_\phi$ , we constrain our He<sup>+</sup> rate, to time periods where, within a 30 minute time frame, the standard deviation of the averaged interplanetary magnetic field was smaller than  $10^\circ$ , i.e.  $\Delta B_\phi, \Delta B_\theta < 10^\circ$ . Furthermore, we only consider time periods from now on, where  $-10^\circ < B_\theta < 10^\circ$ , i.e. time periods where the solar magnetic field vector is confined to the ecliptic plane. This leaves us with  $1.6 \cdot 10^6$  He<sup>+</sup>

events that are distributed among  $4 \cdot 10^4$  unique 5 minutes intervals.

The derived He<sup>+</sup>  $w$ -spectra as a function of the in-ecliptic magnetic field angle  $B_\phi$  are shown in Fig. 3, left panel. Because  $B_\phi$  is non-uniformly distributed over time, the data is normalized to the maximum of each concurrent  $B_{\phi, \text{Bin}}$  with a width of  $4^\circ$ . It appears that during periods where  $67^\circ < |B_\phi| < 113^\circ$ , changes of the IMF orientation are accompanied by changes of the observed  $w$ -spectra. During quasi-perpendicular orientations of the IMF, the He<sup>+</sup>  $w$ -spectra show a relatively steep distribution function with a cut-off at  $w \geq 2.0$ , which transitions into a continuous decay with a cut-off at  $w < 2.0$ . Outside  $67^\circ < |B_\phi| < 113^\circ$ , i.e. during quasi-parallel orientations of the IMF, the He<sup>+</sup>  $w$ -spectra seem to be flatter and not to change with a changing IMF orientation. The shape of the  $w$ -spectra is also illustrated in Fig. 1, where three He<sup>+</sup> count rate  $w$ -spectra are shown for the three different IMF orientation sketched in Fig. 2.

In analogy to the He<sup>+</sup>  $w$ -spectra we create distributions of the in-ecliptic incident angle of He<sup>+</sup>  $\alpha$  for  $1.9 < w < 2.2$  (This  $w$ -constrain reduces our statistics further to  $3.5 \cdot 10^5$  counts distributed among  $3.6 \cdot 10^4$  unique time intervals). We have binned the He<sup>+</sup>  $w$ -spectra at  $1.9 < w < 2.2$  into a 2-d  $B_\phi - \alpha$  grid with bin widths of  $B_{\phi, \text{Bin}} = 4^\circ$  and  $\alpha_{\text{Bin}} = 2.8^\circ$ , which is shown in Fig. 4, left panel. We needed to correct for an instrumental effect, as the distributions of in-ecliptic incident angles as seen from PLASTIC already show a strong anisotropy due to a non-linear efficiency function of the underlying position detection by the resistive anode. To correct this effect and derive the real distribution of He<sup>+</sup> incident angles, we assume that the He<sup>+</sup> velocity distribution is fully isotropic during radial magnetic field configurations as was proposed by Isenberg [1997] and Möbius et al. [1998]. Under these conditions the out-of-ecliptic incident angles  $\beta$ , which do not show any efficiency drift, are believed to show the same distribution as  $\alpha$ . We used these periods to correct the non-linear efficiency drift of  $\alpha$  and to derive the distribution of the in-ecliptic incident angles of He<sup>+</sup> as a function of  $B_\phi$ , which are shown in the left panel of Fig. 4. Similar to the observed He<sup>+</sup>  $w$ -spectra, the distributions of incident angles seem to be a clear function of  $B_\phi$  during periods where  $67^\circ < |B_\phi| < 113^\circ$ , i.e. changing linearly with  $B_\phi$  between the two outermost bins at  $\alpha = \pm 22.5^\circ$ . Outside these periods the distributions of incident angles seem to be centered around  $\alpha = 0^\circ$  and show no dependency on  $B_\phi$ .

## 3. Data Interpretation

The observed  $w$ -spectra of He<sup>+</sup> during periods of a relatively constant magnetic field direction show a clear dependency on the in-ecliptic magnetic field angle  $B_\phi$  (see Fig. 3, left panel). The typical  $w$ -cut-off during a perpendicular alignment of  $\vec{B}$  with respect to  $v_{\text{sw}}^-$  lies at  $w \approx 2.1$ . During configurations with  $\vec{B}$  parallel to  $v_{\text{sw}}^-$  the observed  $w$ -spectra show a significantly smoother decay towards the cut-off as was independently observed by Gloeckler et al. [1995], Möbius et al. [1998], and Saul et al. [2007]. Without consideration of the Eigen-velocity  $v_{\text{ISM}}$  of interstellar neutrals or additional particle acceleration, the injection process sketched in Fig. 2 would produce a sharp cutoff at  $w = 2$ , which drops to  $w = 1.84$  at in-ecliptic magnetic field angles of  $|B_\phi| = 67^\circ, 113^\circ$  (see Eq. 1). Outside the range of  $67^\circ < |B_\phi| < 113^\circ$  PLASTIC is not able to observe the in-situ injection of pickup ions and is only susceptible to the pickup ion component that has undergone pitch-angle scattering by magnetic fluctuations (see Fig. 2). However, in

periods where  $67^\circ < |B_\phi| < 113^\circ$  one expects the in-situ incident angles of He<sup>+</sup> to be a function of  $B_\phi$ , i.e. changing linearly between  $\alpha = -22.5^\circ$  at  $|B_\phi| = 67^\circ$  to  $\alpha = 22.5^\circ$  at  $|B_\phi| = 113^\circ$  as a result of the direct observation of the interstellar pickup ion ring.

To filter for freshly ionized He<sup>+</sup> we used data in a  $w$ -range of  $1.9 < w < 2.2$ . The reason to use such a broad  $w$ -range is, that several effects, e.g. acceleration processes in the heliosphere or a non-zero injection speed of interstellar neutrals, can add a significant uncertainty to the expected velocity of interstellar pickup ions and thus make it rather difficult to give a precise prediction for the velocity of freshly ionized pickup ions with respect to the bulk solar wind. However, it is suffice to say that He<sup>+</sup> ions in this  $w$ -range most likely represent particles that have not undergone significant cooling, i.e. particles that have almost exclusively been freshly ionized, with only small contributions of the cooled pickup ion population.

Fig. 4 (left panel) shows the observed in-ecliptic angles of incidence of freshly ionized He<sup>+</sup>, which behave as one would expect from Fig. 2. For  $B_\phi = (67^\circ, -113^\circ)$  the distribution of  $\alpha$  shows a strong anisotropy up to the outermost edge of the instrument's aperture at  $\alpha = -22.5^\circ$  and changes linearly with  $B_\phi$  up to  $\alpha = 22.5^\circ$  for  $B_\phi = (113^\circ, -67^\circ)$ . We interpret these observations as a direct measurement of a freshly injected pickup ion ring that traverses the instrument's aperture in a narrow angular range perpendicular to  $B_\phi$  as illustrated in Fig. 2 by the thick dashed lines. For all other magnetic field orientations the distributions of He<sup>+</sup>'s in-ecliptic incident angles seem to be centered around  $\alpha = 0^\circ$  and are, as we will show in a moment, consistent with an isotropic pickup ion shell distribution.

To verify our results we use a highly simplified model to reproduce the observed dependencies of  $w$  and  $\alpha$  on the magnetic field direction,  $B_\phi$ , as seen in the left panels of Fig. 3 and Fig. 4. For that we start with an isotropic He<sup>+</sup> velocity distribution function  $\Psi(w_{sw})$  adapted from Vasyliunas & Siscoe [1976] in the upwind region of the Sun. To satisfy observations reported in this paper (Fig. 1) and those made by the Suprathermal Energy Ionic Charge Analyzer [Möbius et al., 1998], who observed during a radial IMF orientation a relatively continuous decay of the He<sup>+</sup>  $w$ -spectra towards  $w \approx 2$ , we further deplete  $\Psi(w_w)$  at  $w_{sw} \leq 2$  using

$$\Psi(w_{sw})_D = \Psi(w_{sw}) \cdot E(w_{sw}, 0, 0.5),$$

where  $E(x, x_0, \sigma) = \exp(0.5 \cdot ((x - x_0)/\sigma)^2)$ . This models an isotropic interstellar shell-like pickup ion velocity distribution function, which has already been cooled to lower  $w$ . In a second step, we superpose on this shell distribution a freshly injected pickup ion ring distribution

$$\Psi(w_{sw}, B_\phi)_P = \Psi(w_{sw}) \cdot E_a(w_{sw}, 1, 0.1) \quad (2)$$

$$\cdot E_b(\cos(\pi - B_\phi), 0, 0.1), \quad (3)$$

to obtain a general representation of a He<sup>+</sup> velocity distribution, which includes a freshly injected pickup ion ring at  $w = 2$  (as observed in Fig. 1 and accomplished through  $E_a$ ), which is localized in a narrow angular range perpendicular to  $B_\phi$  (accomplished through  $E_b$ ) as illustrated in Fig. 2. The final model for the He<sup>+</sup> velocity distribution function is then

$$f(w_{sw}, B_\phi) = \Psi(w_{sw})_D + \Psi(w_{sw}, B_\phi)_P, \quad (4)$$

which is shown in Fig. 5 for  $B_\phi \perp v_{sw}$ . We note, that it is not our intention to give an explanation but rather an impression of the form of the He<sup>+</sup> distribution function. Our parameters for the model are therefore mainly deduced from

our observation of the pickup ion ring shown in Fig. 1 instead of being physically motivated. However, our model may be used as a first reference point for further studies on the distribution function of interstellar pickup ions.

In order to derive the expected  $w$ -spectra and  $\alpha$ -distribution as seen from PLASTIC we need to convolve  $f(w_{sw}, B_\phi)$  with the respective instrument response function. This allows us to derive the expected counts per second for each instrumental incident angle  $(\alpha, \beta)$  and energy-per-charge step  $i$

$$C(v_{ion}^i, \alpha, \beta) = f(w_{sw}, B_\phi) \cdot V_P^{i, \alpha, \beta} \cdot V_S^{i, \alpha, \beta}, \quad (5)$$

where  $C(v_{ion}^i, \alpha, \beta)$  is the expected count rate,  $V_P^{i, \alpha, \beta}$  the velocity space volume (grey dots in Fig. 5) and  $V_S^{i, \alpha, \beta}$  the position space volume, which are defined as

$$V_P^{i, \alpha, \beta} = (v_{ion}^i)^2 \sin(\beta) \Delta v_i \Delta \beta \Delta \alpha$$

$$V_S^{i, \alpha, \beta} = v_{ion}^i A_{act}^\alpha.$$

Here  $A_{act}$  denotes the active area of the Solar Wind Section, while  $V_P$  and  $V_S$  span the volume in phase space that PLASTIC can observe.

With equations 4 and 5 we can now determine the expected  $w$ -spectra and  $\alpha$ -distribution from the velocity distribution function shown in Fig. 5 as a function of the in-ecliptic magnetic field angle  $B_\phi$ . We show these model distributions in the right hand panels of Fig. 3 and Fig. 4 as a direct comparison to our observations, which are shown in the left hand panels of Fig. 3 and Fig. 4. For the expected  $w$ -spectra in Fig. 3 we had to use instrumental logarithmically spaced  $w$ -bins contrary to our observations, where we could use linear spaced  $w$ -bins due to the mixture of many solar wind velocities.

Although equation 5 is a simplified version of the instrumental response function, we can already qualitatively reproduce our observation from Fig. 3, left panel. More importantly, our model for the He<sup>+</sup> velocity distribution function with a pickup ion injection ring perpendicular to  $\vec{B}$  can clearly reproduce our observations shown in Fig. 4, left panel.

## 4. Conclusion

Interstellar pickup ions, which are believed to be injected as a ring-like velocity distributions into the bulk solar wind, are exposed to fluctuations of the IMF and thus undergo pitch angle scattering. It is generally assumed that this process can be very efficient on short time scales, and thus velocity distributions of pickup ions were believed to be fully isotropic in nature [Vasyliunas & Siscoe, 1976]. However, unambiguous evidence for this assumption has yet to be found. Indeed observations of reduced one dimensional  $w$ -spectra for quasi-parallel and -perpendicular IMF orientations revealed a significant difference in flux and spectral shape of interstellar He<sup>+</sup> pickup ions, which e.g. Saul et al. [2007], Möbius et al. [1998], and Isenberg [1997] attributed to ineffective scattering across 90 pitch-angle.

Our analysis of the in-situ pitch-angle distribution of He<sup>+</sup> with PLASTIC aboard STEREO A revealed a highly isotropic population of cooled interstellar pickup ions. Superposed onto this population, we found an almost scatter-free pickup ion population that follows a strict gyro motion perpendicular to  $\vec{B}$ , which we interpret to be a direct imprint of the injection of freshly ionized interstellar helium into the bulk solar wind. Thus, we could show that interstellar pickup are not fully isotropic and instead show distinct anisotropies resulting from the pickup process.

The locally injected interstellar He<sup>+</sup> pickup ion ring exhibits a significantly different behaviour than the isotropic component in terms of pitch-angle and  $w$ -distribution and strictly follows the concurrent orientation of the IMF. However, observation of this population can only be made during IMF orientation, where PLASTIC is sensitive to a freshly injected pickup ring, i.e.  $67^\circ < |B_\phi| < 113^\circ$ . During these periods we observed a highly anisotropic distribution of He<sup>+</sup> incident angles that were accompanied by distinct changes of the observed shape of He<sup>+</sup>  $w$ -spectra with  $B_\phi$ . As sketched in Fig. 2 and shown in Fig. 1, this naturally causes the He<sup>+</sup>  $w$ -spectra to be a function of the instrumental magnetic angle  $\alpha$ , as described in Eq. 1). A highly simplified model of the He<sup>+</sup> velocity distribution that includes a freshly injected pickup ion ring superposed onto a cooled, isotropic pickup ion model (based on theoretical work from Vasyliunas & Siscoe [1976]), was able to reproduce our observations strikingly well (see Fig. 4 and Fig. 3). In view of our current findings, independent observations made by Ulysses/SWICS [Gloeckler et al., 1995], CELIAS/CTOF [Saul et al., 2007], and AMPTE/SULEICA [Möbius et al., 1998] of a signifi-

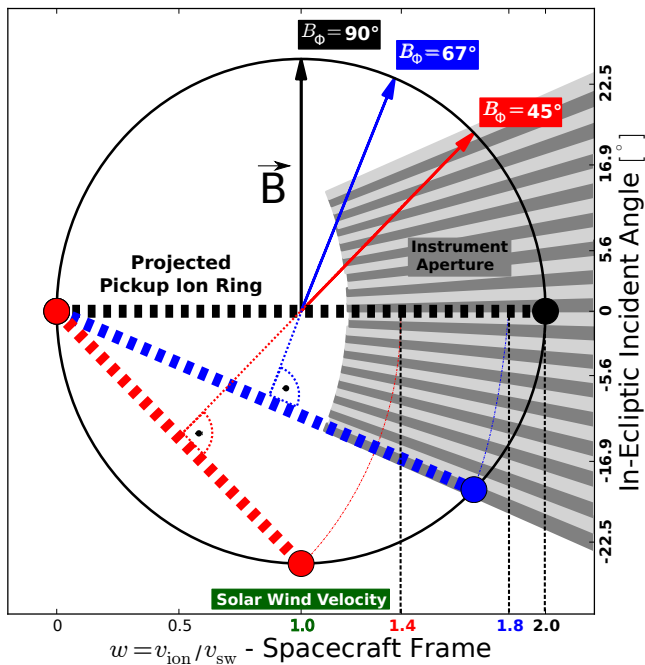


**Figure 2.** Illustration of pickup ion ring-beam distributions in phase space (the x-axis points in the direction of the moving solar wind at  $v_z = 0$  km/s, i.e. in the ecliptic plane). Using the simplification that  $v_{\text{ISM}} = 0$  km/s, freshly ionized interstellar pickup ions start to gyrate perpendicular to  $\vec{B}$  with a maximum velocity of twice the solar wind velocity. The resulting velocity distribution function is often referred to as ring-beam distribution (thick dashed lines) and can be described to be a result of a two dimensional cut at  $v_p = 0$  km/s perpendicular to  $\vec{B}$  through a spherical shell (black outer circle) with a radius of  $r = v_{\text{sw}}$ . Due to the ion's perpendicular motion around the solar magnetic field vector  $\vec{B}$  and PLASTIC's limited angular acceptance, observations of freshly ionized pickup ions are confined to in-ecliptic magnetic field angles between  $67^\circ < |B_\phi| < 113^\circ$ , i.e. ranges in which the resulting ring-beam distribution is covered by the instrument's aperture (grey shaded area).

cantly reduced flux and much smoother decay of the observed interstellar pickup ion  $w$ -spectra can not be solely explained by ineffective scattering across 90 pitch-angle. In fact, our observations strongly suggests that these observations are the result of a relatively scatter-free pickup ion ring that, during many IMF orientations, escapes detection. However, a relatively smooth decay towards  $w = 2$  of the isotropic He<sup>+</sup>  $w$ -spectra, as evidenced by the aforementioned observations and this publication, is necessary in our simplified model to fully reproduce our observations.

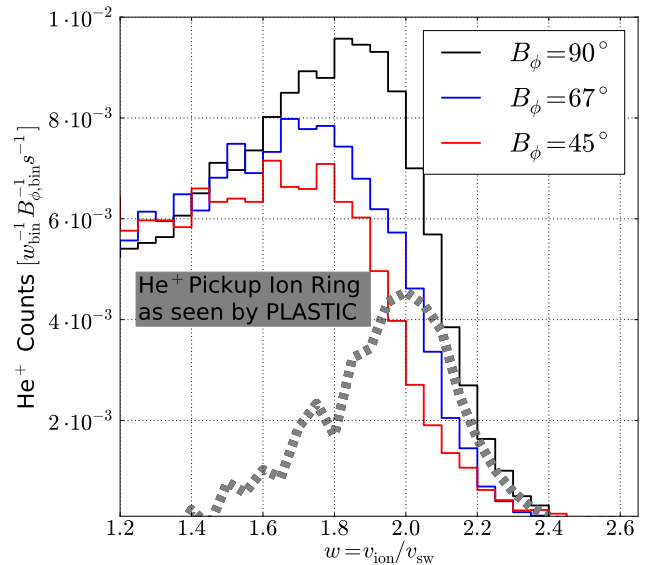


**Figure 1.** Averaged He<sup>+</sup> count rate  $w$ -spectra for three different IMF orientations as shown in Fig. 2 (black, blue, red lines). The dashed grey line shows the absolute difference of the He<sup>+</sup>  $w$ -spectrum between periods where PLASTIC is sensitive to the measurement of a He<sup>+</sup> pickup ion ring (black) and not (red).

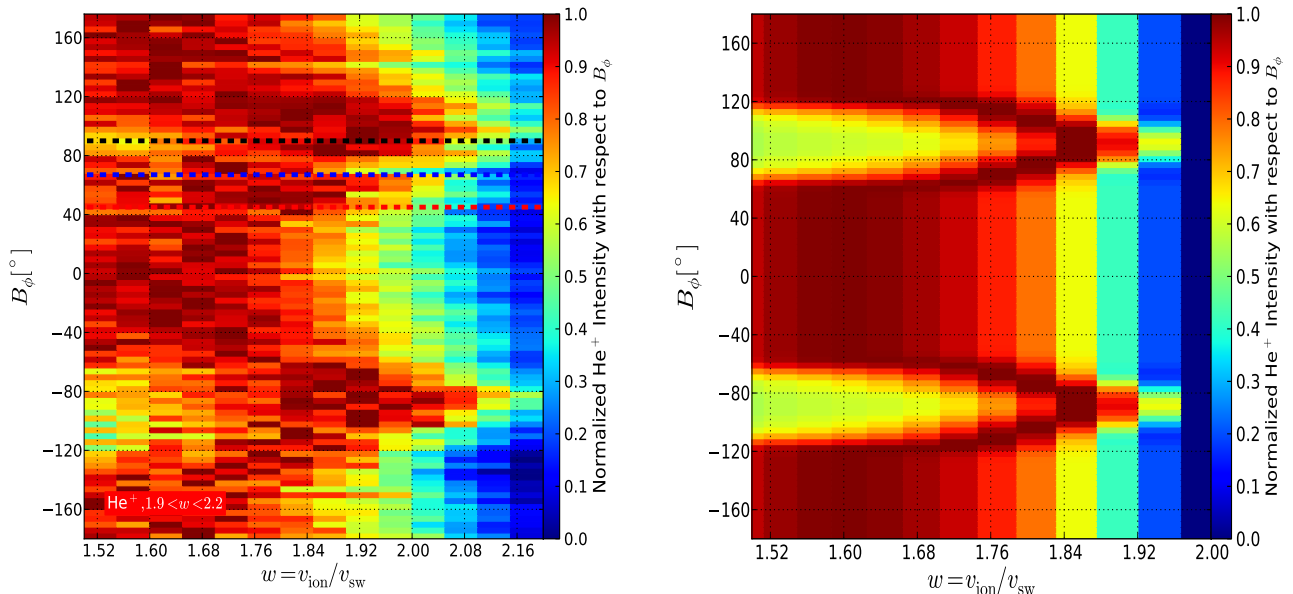


**Figure 3.** Left panel: He<sup>+</sup> $w$ -spectra (x-axis) measured as a function of the in-ecliptic magnetic field angle  $B_\phi$  (y-axis) between March 2007 and December 2009 with STEREO/PLASTIC. The intensity of the He<sup>+</sup> $w$ -spectra ( $\Delta w_{\text{bin}} = 0.04$ ) is normalized to the maximum of each  $B_{\phi,\text{bin}}$  ( $\Delta B_{\phi,\text{bin}} = 4^\circ$ ). The black, blue, and red dashed lines represent IMF configuration as sketched in Fig. 2. Right panel: modeled He<sup>+</sup> $w$ -spectra (x-axis) as a function of the in-ecliptic magnetic field angle  $B_\phi$  (y-axis).

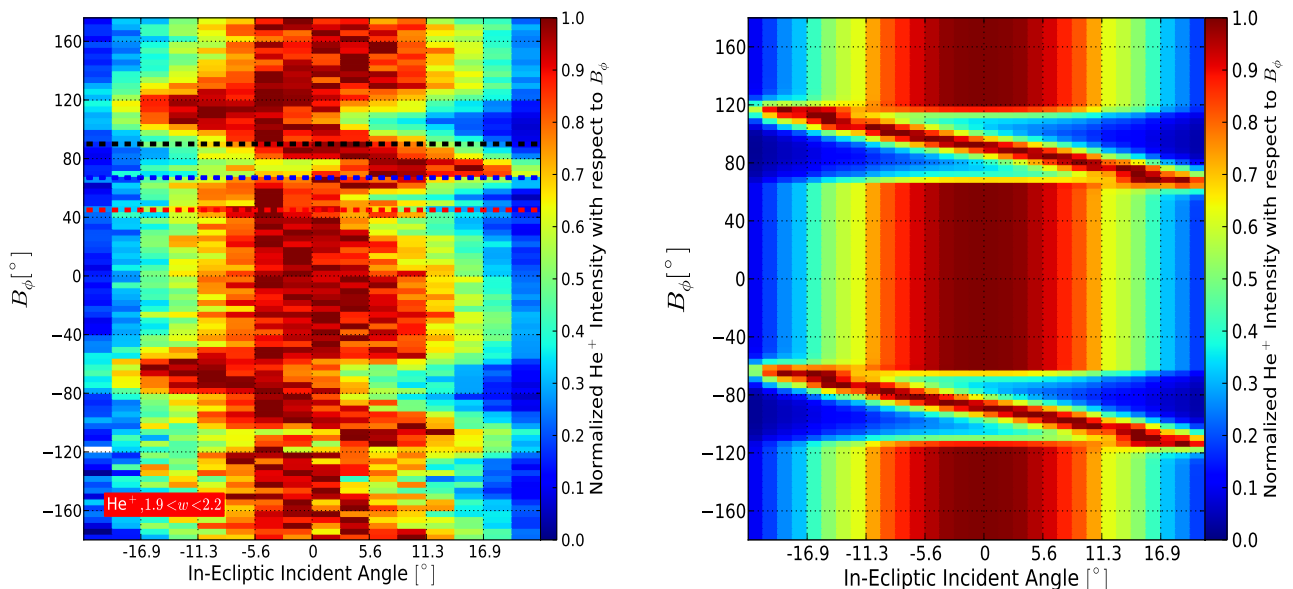


**Figure 4.** Left Panel: Distributions of the angle of incidence,  $\alpha$ , of interstellar He<sup>+</sup> ions measured as a function of  $B_\phi$  in the  $w$ -range  $1.9 < w < 2.2$  with STEREO/PLASTIC. The x-axis shows the incident angle  $\alpha$  and the y-axis the in-ecliptic magnetic field angle  $B_\phi$ . The angular distribution is normalized to the maximum of each  $B_{\phi,\text{Bin}}$ . The black, blue, and red dashed lines represent magnetic field configuration as sketched in Fig. 2. Right panel: modeled distribution of the angle of incidence of interstellar He<sup>+</sup> as a function of the in-ecliptic magnetic field angle  $B_\phi$  (y-axis).

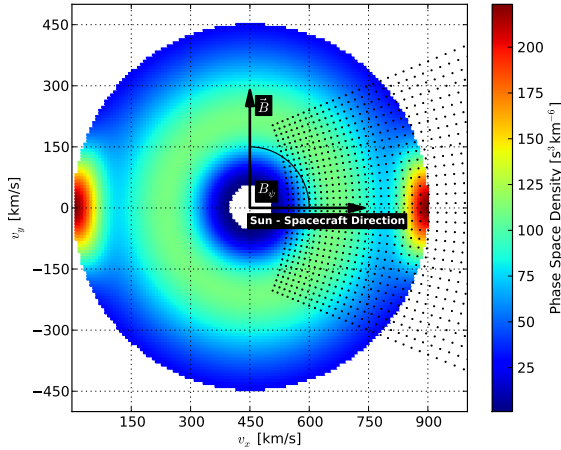


**Figure 5.** A 2-d cut of the model He<sup>+</sup> phase space density in the  $(v_x, v_y)$  plane at  $v_z = 0$  km/s for the situation in which  $\vec{B} \perp v_{sw}$  and  $v_{sw} = 450$  km/s. It shows an isotropic pickup ion shell distribution (inner green ring at  $\sim 250$  km/s) superposed with a freshly injected pickup ion ring perpendicular to  $\vec{B}$  at  $w_{sw} = 1$ . The grey dots in each panel represent the location of phase space covered by the PLASTIC instrument. This model, but for all possible orientations of  $\vec{B}$ , is used for the simulations shown in the right hand panels of Fig. 4 and Fig. 3 for varying IMF orientations.

**Acknowledgments.** This work was supported by the German Science Foundation (Deutsche Forschungsgemeinschaft) under grant Wi-2139/7-1.

## References

- Acuña, M. H., Curtis, D., Scheifele, J. L., et al. 2008, 136, 203
- Drews, C., Berger, L., Wimmer-Schweingruber, R. F., et al. 2012, *Journal of Geophysical Research (Space Physics)*, 117, 9106, doi:10.1029/2012JA017746
- Isenberg, P. A. 1997, *J. Geophys. Res.*, , 102, 4719
- Galvin, A. B., L. M. Kistler, M. A. Popecki, C. J. Farrugia, K. D. C. Simunac, L. Ellis, E. Möbius, M. A. Lee, M. Boehm, J. Carroll, A. Crawshaw, M. Conti, P. Demaine, S. Ellis, J. A. Gaidos, J. Googins, M. Granoff, A. Gustafson, D. Heirtzler, B. King, U. Knauss, J. Levasseur, S. Longworth, K. Singer, S. Turco, P. Vachon, M. Vosbury, M. Widholm, L. M. Blush, R. Karrer, P. Bochsler, H. Daoudi, A. Etter, J. Fischer, J. Jost, A. Opitz, M. Sigrist, P. Wurz, B. Klecker, M. Ertl, E. Seidenschwang, R. F. Wimmer-Schweingruber, M. Koeten, B. Thompson, and D. Steinfeld (2008) , *Space Sci. Rev.*, 136, 437–486, doi:10.1007/s11214-007-9296-x.
- Gloeckler, G., Schwadron, N. A., Fisk, L. A., & Geiss, J. 1995, *Geophys. Res. Lett.*, , 22, 2665
- Möbius, E., Rucinski, D., Lee, M. A., & Isenberg, P. A. 1998, *J. Geophys. Res.*, , 103, 257
- Oka, M., Terasawa, T., Noda, H., Saito, Y., & Mukai, T. 2002, *Geophys. Res. Lett.*, , 29, 1612
- Saul, L., Möbius, E., Isenberg, P., & Bochsler, P. 2007, *Astrophys. J.*, , 655, 672
- Saul, L., Wurz, P., & Kallenbach, R. 2009, *Astrophys. J.*, , 703, 325
- Vasyliunas, V. M., & Siscoe, G. L. 1976, *J. Geophys. Res.*, , 81, 1247
- Lars Berger, Institut für experimentelle und angewandte Physik, Christian-Albrechts-Universität Kiel, Leibnizstr. 11, 24118 Kiel, Germany (berger@physik.uni-kiel.de)
- Christian Drews, Institut für experimentelle und angewandte Physik, Christian-Albrechts-Universität Kiel, Leibnizstr. 11, 24118 Kiel, Germany (drews@physik.uni-kiel.de)
- Antoinette B. Galvin, Space Science Center and Department of Physics, University of New Hampshire, Morse Hall, 8 College Road, NH 03824 Durham, New Hampshire, USA (toni.galvin@unh.edu)
- Robert F. Wimmer-Schweingruber, Institut für experimentelle und angewandte Physik, Christian-Albrechts-Universität Kiel, Leibnizstr. 11, 24118 Kiel, Germany (wimmer@physik.uni-kiel.de)

### 5.3. Supplementary Remarks

#### 5.3.1. Virtual Detector

The Virtual Detector is used to transform any model-based velocity distribution function  $f(\mathbf{v})$  into a three dimensional count rate spectrum as seen by PLASTIC. For each combination of energy-per-charge steps  $i$ , Position bins  $j$ , and Deflection steps  $k$  PLASTIC covers different volumes  $V_P^{i,j,k}$  in velocity space. These volumes (see right panel in Fig. 5.2) have a width in  $v_r$ -direction coming from the uncertainty  $\Delta(E/q)$  of the  $E/q$  measurement, a width in  $\alpha$ -direction coming from the azimuthal opening angle  $\Delta(\alpha)$ , and a width in  $\beta$ -direction coming from the polar acceptance  $\Delta(\beta)$ . Integrating a velocity distribution function  $f(\mathbf{v})$  over the respective coordinates of  $V_P^{i,j,k}$  yields the density  $n_{i,j,k}$  of the respective energy-per-charge, Position, and Deflection step.

$$n_{i,j,k} = \int_{V_P^{i,j,k}} f(\mathbf{v}) dV \quad (5.1)$$

$$= \int_{\Delta(E/q_i)} \int_{\Delta(\alpha_j)} \int_{\Delta(\beta_k)} f(\mathbf{v}) v_r^2 \sin(\alpha) dv_r d\alpha d\beta \quad (5.2)$$

$$\approx f(\mathbf{v}) \cdot V_P^{i,j,k} \quad (5.3)$$

The third step can be done if you assume that  $f(\mathbf{v})$  changes only little over  $V_P^{i,j,k}$ . This may be true for the SWS, but not necessarily for the WAP, where we have broader polar and azimuthal acceptances. Although the integration is implemented in the Virtual Detector, we use Eq. (5.3) to derive the density  $n_{i,j,k}$  for our publication in section 5.2. This simply saves us some computation time, which increases with  $N^3$ , whereas  $N$  is the number of integration steps in  $v_r, \alpha, \beta$  direction.

In order to derive the expected counts  $C_{i,j,k}$  for each energy-per-charge, Position, and Deflection step as seen from PLASTIC, we have to multiply the density  $n_{i,j,k}$  with the respective area in position space  $V_S^{i,j,k}$  that is covered by the instrument.

$$C_{i,j,k} = f(\mathbf{v}) \cdot V_P^{i,j,k} \cdot V_S^{i,j,k} \quad (5.4)$$

Furthermore, we need to consider several instrumental response functions that are included in our response parameter  $R^{i,j,k}$ .

$$\boxed{C_{i,j,k} = f(\mathbf{v}) \cdot V_P^{i,j,k} \cdot V_S^{i,j,k} \cdot R^{i,j,k}} \quad (5.5)$$

In the following a more detailed description of  $f(v_x, v_y, v_z)$ ,  $V_P^{i,j,k}$ ,  $V_S^{i,j,k}$ , and  $R^{i,j,k}$  is given.

#### Velocity Distribution Function $f(v_x, v_y, v_z)$

In order to use Eq. 5.5, the first thing to do is to determine the velocity distribution function at a location in phase space corresponding to energy-per-charge step  $i$ , Position

### 5.3. SUPPLEMENTARY REMARKS

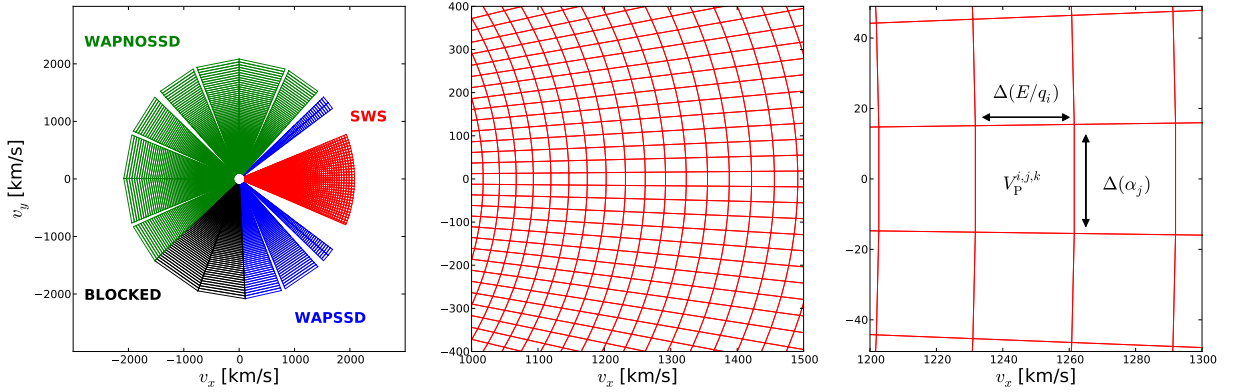


Figure 5.2.: Left figure: Representation of the phase space volumes  $V_P^{i,j,k}$  spanned by PLASTIC in the  $v_x$ - $v_y$  plane. The red grid denotes the phase space volumes covered by the Solar Wind Section, the blue grid by the Wide Angle Partition SSD, the green grid by the Wide Angle Partition NOSSD, and the black grid volumes that are physically blocked by support structures of the instrument. Center figure: magnified view of the phase space covered by the Solar Wind Section. Right figure: Magnified view of a distinct phase space volume  $V_P^{i,j,k}$  for energy-per-charge step  $i$ , Position bin  $j$  and Deflection Step  $k$ .

bin  $j$  and Deflection step  $k$ . For that we need the coordinates  $v_x, v_y, v_z$  of the respective phase space volume.

$$\begin{aligned}
 v_r &= \text{velocity}(E/q_i, m, q) \\
 \alpha &= \alpha_j \\
 \beta &= \beta_k \\
 &| \text{ transform into cartesian coordinates} | \\
 &\rightarrow v_{x,y,z}^{i,j,k}
 \end{aligned}$$

Here,  $m$  and  $q$  is the mass and charge state of the investigated ion,  $\text{velocity}(E/q_i, m, q)$  is a function to determine the velocity (in radial direction) of a given ion from the energy-per-charge step  $i$ , and  $\alpha_j$  and  $\beta_k$  are the incident angles of Position bin  $j$  and Deflection step  $k$  respectively. Note that  $\beta_k$  and  $\alpha_j$  are the centered angular positions around the respective angular range of the given bins. For example: Deflection step 31 goes from  $20^\circ$  to  $18^\circ$ , therefore  $\beta_{31}$  will be  $19^\circ$ . In order to implement the aberration coming from the spacecraft velocity  $v_{SC}$ , we also have to shift the velocity distribution function in phase space. In the current coordinate system, where the  $x$ -direction is pointing from the sun towards the spacecraft, the velocity vector of STEREO is perpendicular to  $x$  in the  $y$ -direction (assuming a circular orbit of STEREO A and B). Thus, we have to add an offset of  $v_{SC,y}$  to  $f(v_x, v_y, v_z)$ .

$$f(v_x, v_y, v_z)_{SC} = f(v_x, v_y + v_{SC,y}, v_z)$$



### Velocity Space Volume $V_P^{i,j,k}$

The velocity space volume  $V_P^{i,j,k}$  determines the amount of the velocity distribution function  $f(v_x, v_y, v_z)$  covered by the respective combination of energy-per-charge steps  $i$ , Position bins  $j$  and Deflection steps  $k$ . The location  $(v_x, v_y, v_z)$  that was derived in section 5.3.1 determines which part of  $f(v_x, v_y, v_z)$  is covered. To determine  $V_P^{i,j,k}$  we have to calculate the volume element that is spanned by the uncertainty in velocity  $\Delta(v_i)$ , polar acceptance  $\Delta(\beta_k)$  and azimuthal opening angle  $\Delta(\alpha_j)$ . Keep in mind, that  $\beta_k$  is measured from the  $v_z$ -direction to the  $v_x - v_y$  plane. Thus, Fig. 5.2 shows a representation of PLASTIC in phase space at  $\beta_k = \pi/2$ .

$$V_P^{i,j,k} = v_i^2 \sin(\beta_k) \Delta(v_i) \Delta(\alpha_j) \Delta(\beta_k) \quad (5.6)$$

The parameters  $\Delta(v_i)$ ,  $\Delta(\alpha_j)$ ,  $\Delta(\beta_k)$  will be discussed at the end of this chapter.

### Position Space Volume $V_S^{i,j,k}$

Particles will enter the instrument through an area  $A_{act}^j$  with a velocity of  $v_{ion}^i$  during a time period  $\tau_k$ . In other words, they come from a volume  $V_S^{i,j,k}$  in space. In order to derive the expected count rates  $C_{i,j,k}$  as seen by PLASTIC we have to multiply the density  $n_{i,j,k}$  (coming from the integration of  $f(v_x, v_y, v_z)$  over the respective velocity space volume  $V_P^{i,j,k}$ ) with the respective space volume  $V_S^{i,j,k}$ .

$$V_S^{i,j,k} = v_{ion}^i A_{act}^j \tau \quad (5.7)$$

The parameters  $v_{ion}^i$ ,  $A_{act}^j$ ,  $\tau$  will be discussed at the end of this chapter.

### Response Parameter $R^{i,j,k}$

With the Virtual Detector we would now be able to derive the expected counts for each combination of energy-per-charge steps  $i$ , Position bins  $j$  and Deflection steps  $k$  assuming that PLASTIC works with 100% efficiency. But this is not the case so we have to consider several additional parameters.

- **Single Efficiency  $\gamma_{i,ion}$**   
This is the overall probability that an ion with a velocity given by the energy-per-charge step  $i$  is detected.
- **Azimuthal Response  $\mu_j$**   
This parameter accounts for the azimuthal response, thus it depends on the position bin  $j$ .
- **TCR efficiency  $\delta_{i,ion}$**   
This is the probability that an ion with a velocity given by the energy-per-charge step  $i$  deposits its energy in the SSD.

### 5.3. SUPPLEMENTARY REMARKS

---

- Measurement time  $t_k$   
Currently the Virtual Detector yields the expected counts for one measurement cycle ( $\approx 1$  min). To derive the expected counts in longer time periods one has to multiply  $C_{i,j,k}$  with the measurement time expressed in minutes.
- Small channel switch  $h_i$   
This would be a factor that accounts for the small channel switch. The small channel switch will basically alter the active area  $A_{\text{act}}^j$  and polar angle acceptance  $\Delta\beta_k$ .

This results in a response parameter

$$R^{i,j,k} = \gamma_{i,\text{ion}} \mu_j \delta_{i,\text{ion}} t_k h_i. \quad (5.8)$$

The single efficiency and small channel switch are not yet included in  $R^{i,j,k}$ . As a consequence, the Virtual Detector overestimates the expected count rates as seen by PLASTIC. This, however, has a negligible effect on our study of interstellar pickup ions. The channel switch is triggered at an energy-per-charge step that is clearly below the characteristic energy-per-charge of interstellar  $\text{He}^+$  and the single efficiency changes only little in the higher energy regime that is typical for pickup ions.

#### Instrumental Parameters

- $\Delta(E/q)$ : Uncertainty in energy-per-charge  
 $\Delta(E/q) = 6.3\%$  FWHM
- $\Delta v_j$ : Resulting uncertainty in ion velocity  
 $\Delta v_i = \text{velocity}(E/q \cdot 1.03) - \text{velocity}(E/q \cdot 0.97)$
- $\Delta\alpha_j$ : Opening angle in azimuthal direction  
This parameter strongly depends on the different instrument sections (SWS, WAPSSD, WAPNOSSD). For each position bin in the SWS  $\Delta\alpha_j = 45^\circ/32 = 1.40625^\circ$ .
- $\Delta\beta_k$ : Opening angle in polar direction  
This parameter strongly depends on the different instrument sections (SWS, WAPSSD, WAPNOSSD). For each deflection step in the SWS  $\Delta\beta_k = 2.0$  (Main channel).
- $A_{\text{act}}^j$ : Active area of Position bin j.  
This parameter strongly depends on the different instrument sections (SWS, WAPSSD, WAPNOSSD). For the SWS  $A_{\text{act}}^{\text{SWS}} = 0.89 \text{ cm}^2$  resulting in an active area per Position bin of  $A_{\text{act}}^j = 0.89/32$ . Note, that  $A_{\text{act}}$  does not depend on the deflection steps, because they are not active at the same time (contrary to the position bins).
- $\tau$ : Collection time during one Deflection step.  
 $\tau = 12.8\text{ms}$ , which results in a total collection time per energy-per-charge cycle of  $\approx 1$  min.

## 6. Conclusions & Outlook

In this thesis three different aspects of interstellar pickup ions have been explored. In our first publication "Observations of interstellar neon in the helium focusing cone" [Dreus *et al.*, 2010] we examined the distribution of interstellar pickup ions at 1 AU with STEREO/PLASTIC. For that we have utilized a maximum likelihood estimator based on Poissonian statistics that is able to deal with the low fluxes expected for heavy pickup ions at 1 AU. Furthermore, we have developed a method to counteract the modulation of heavy pickup ion fluxes with the prevalent solar wind speed, by which we were able to derive unbiased time series with a 27-day resolution of inner-source as well as interstellar pickup ions at 1 AU. As a results we could confirm for the first time the formation of the focusing cone for interstellar neon, whose survival probability as neutrals is only slightly higher than that of helium. By studying properties of the neon focusing cone such as its width, intensity, and geometry, one can theoretically infer the temperature, density, and velocity of vector of neon inside the LISM. However, the natural modulation of interstellar pickup ions with the solar wind as well as several instrumental difficulties with STEREO/PLASTIC makes finding parameters of the LISM a challenging problem.

In our second publication "Inflow direction of interstellar neutrals deduced from pickup ions measurements at 1 AU" [Dreus *et al.*, 2012] we addressed the aforementioned problem by using a statistical approach to infer the inflow direction of the LISM with respect to the heliosphere. Comparing our analysis to a "standard" approach, which typically does not consider pickup ion modulations by the solar wind, we could show that for parameter studies of the LISM it is absolutely crucial to incorporate the influence on pickup ion fluxes by solar wind modulations. We also observed for the first time the interstellar crescent, i.e. an overabundance of interstellar  $\text{He}^+$ ,  $\text{O}^+$ , and  $\text{Ne}^+$  on the upwind side of the Sun, and could successfully adapt its geometry for our study. We determined the average inflow direction to be in the range  $\lambda_{\text{ISM}} = 78.4^\circ \pm 1.3^\circ$ , which is a significant deviation from previous values for the inflow direction of the interstellar medium given since 2004 (see Fig. 6.1). Our values for  $\lambda_{\text{ISM}}$ , however, are in very good agreement with values determined by the IBEX mission, which is capable of measuring interstellar neutrals directly and is therefore not influenced by solar wind modulations. In order to present a "well-defined" value for  $\lambda_{\text{ISM}}$  we also studied two relevant systematic biases, i.e. the orbit eccentricity and instrumental aging, on our results for the inflow direction of the interstellar medium.

In our third publication "Interstellar  $\text{He}^+$  Ring-Beam Distributions: Observations and Implications" [Dreus *et al.*, 2013] we examined the kinetic behaviour of interstellar  $\text{He}^+$  on short time scales. An analysis of the initial pitch-angle distribution of  $\text{He}^+$  revealed an almost isotropic velocity distribution function unaffected by the prevalent interplanetary magnetic field orientation. However,  $\text{He}^+$  also exhibits a highly anisotropic component that strictly follows a gyro motion perpendicular to  $\mathbf{B}$  and is superposed onto the isotropic background. We interpreted this component to be an imprint of freshly ionized interstellar helium atoms directly after the injection into the solar wind and argued that independent

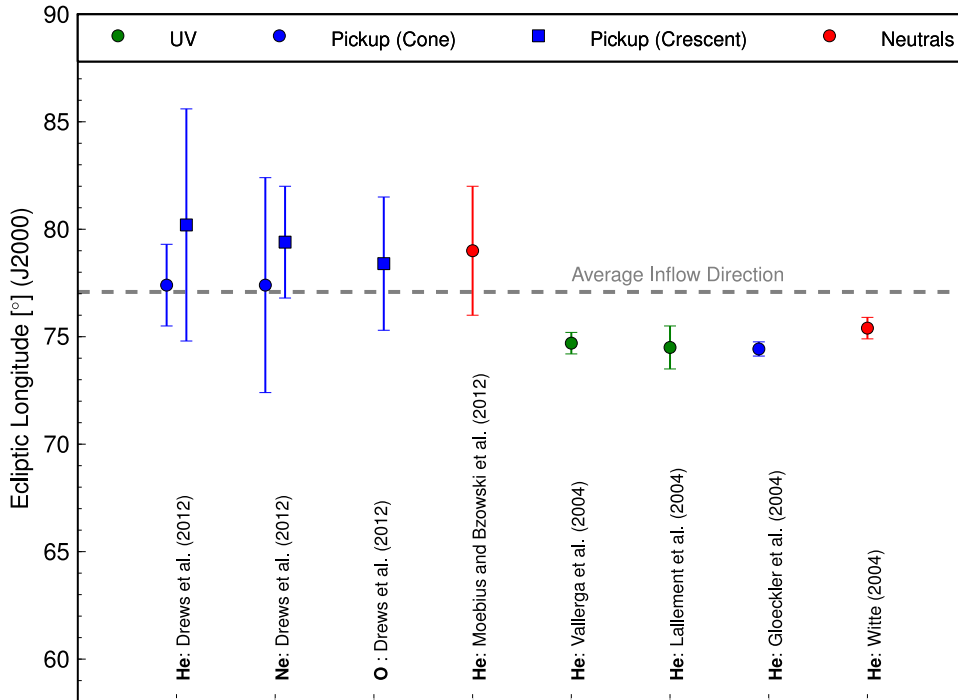


Figure 6.1.: Inflow direction of the local interstellar medium deduced from interstellar pickup ion (blue), ultra-violet radiation (green), and interstellar neutral measurements (red). The pickup ion category is further divided into focusing cone (circles) and crescent measurements (squares).

observations of a reduced flux during certain magnetic field configuration can be solely explained by this anisotropic  $\text{He}^+$  component instead of being a result of inefficient pitch-angle across  $90^\circ$ . Our findings also illustrate the importance of the prevalent orientation of the interplanetary magnetic field for pickup ion velocity distribution functions and therefore questions many of the existing interstellar pickup ions models.

Although we explored three different aspects of interstellar pickup ions in this thesis and by that were able to make several new discoveries like the observation of the neon focusing cone, finding a refined value for the inflow direction of the LISM, and observing the anisotropy of interstellar pickup ion velocity distribution functions, we only scratched the surface of what can be achieved on pickup ions with STEREO/PLASTIC. Especially inner-source pickup ions, which have mainly been observed and studied with the SWICS instrument on-board the Ulysses spacecraft over the last years, have not yet been studied with PLASTIC. Therefore, we have started an investigation on inner-source pickup ions with PLASTIC (supported by Deutsche Forschungsgemeinschaft under grant Wi-2139/7-1), which will address the question how the source region of inner-source pickup ions is formed. For that we need to study the spectra and composition of inner-source pickup ions, which also requires a careful consideration of instrumental effects in a similar fashion to our study in *Drews et al.* [2012]. In contrast to the measurements by Ulysses, we will be able to give values, which have been averaged over the entire heliospheric longitude range, as well as possible variations in composition. We also expect to derive a much improved characterization of inner-source pickup ions by their spatial

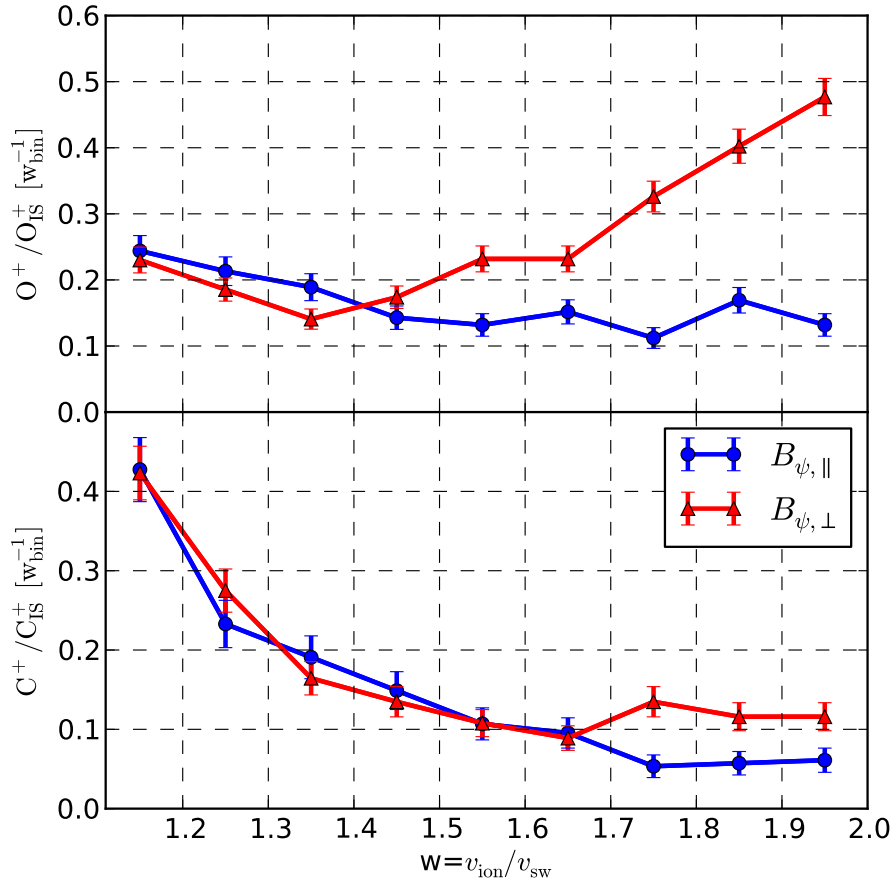


Figure 6.2.: Oxygen (top panel) and carbon (bottom panel)  $w$ -spectra during parallel (blue) and perpendicular (red) configurations of the interplanetary magnetic field. The data was collected with the Solar Wind Section of PLASTIC over a period of 1500 days.

and temporal resolution at a hitherto unachievable high resolution with PLASTIC. An example of our ongoing study on inner-source pickup ion  $w$ -spectra is shown in Fig. 6.2. Here we compare the  $w$ -spectra of oxygen (top panel) and carbon (bottom panel) during perpendicular (red) and parallel (blue) configuration of the interplanetary magnetic field with respect to the outflowing solar wind. Similar to our study in *Dreus et al.* [2013] the initial ring-beam distribution of interstellar oxygen that stems from the gyro motion of freshly ionized interstellar oxygen is clearly visible for  $w > \sim 1.5$  (although in form of a reduced one dimensional spectrum compared to the helium ring-beam distribution shown in *Dreus et al.* [2013]). Remarkably, Fig. 6.2 also shows a carbon ring-beam distribution that, despite being less clear compared to its oxygen counterpart, is still statistical significant. Because interstellar carbon is likely too uncommon to produce such a signature, this observation raises the question whether carbon pickup ions can solely be attributed to a source region close to the Sun as is commonly believed.

Furthermore, it is already planned to extend our investigation presented in *Dreus et al.*

---

[2010] and *Drews et al.* [2012] in several ways. Figure 5 in *Drews et al.* [2010] shows that we might be able to give a limit of the isotopic abundance ratio of interstellar  $^{20}\text{Ne}/^{22}\text{Ne}$ . "The definitive value of this ratio is - to our best knowledge - unknown. Some samples of it pose an interesting puzzle. Measurements of galactic cosmic rays show a value, which is reduced by a factor of about 5 relative to the solar wind value (e.g. [*Binns et al.*, 2001], [*Wimmer-Schweingruber*, 2002]). This value has been corrected for propagation effects and is supposed to reflect the galactic average Ne-isotopic composition. In other word, the most precise galactic cosmic ray measurements available indicate that there is roughly five times more  $^{22}\text{Ne}$  compared to  $^{20}\text{Ne}$  in the galaxy than in the ISM from which the Sun formed some 4.57 billion years ago. Using a solar value for this ratio, we can expect roughly 2  $^{22}\text{Ne}^+$  events per week based on the  $\sim 4$  counts per day of  $^{20}\text{Ne}^+$  (compare Fig. 3 in *Drews et al.* [2010]). Therefore, given STEREO's mission duration so far, we will be able to give a value, which is primarily determined by systematic uncertainties and not counting statistics. Thus the key difficulty in this investigation will be the determination of the systematic uncertainties" [*Wimmer-Schweingruber and Drews*, 2012].

We also plan for the future a more detailed study of the neon focusing cone and interstellar crescent, i.e. studying the shape of these structures. We already studied their longitudinal location and by that were able to derive the inflow direction of the local interstellar medium [*Drews et al.*, 2012]. The shape of these structures, however, is mainly determined by the temperature and flow speed of the interstellar medium and thus could help to infer differences in the flow velocity and temperature of these species. Such a study also needs to address the important influence of the interplanetary magnetic field on pickup ion velocity distribution function by a proper pickup ion model (compare *Drews et al.* [2013]). The work presented in this thesis is likely the only study to date that can provide the necessary information on the heliospheric distribution of interstellar pickup ions at 1 AU as well as their three dimensional velocity distribution function that is required for a proper pickup ion model.

# A. Systematic Influences by Efficiency Decay

## Decay

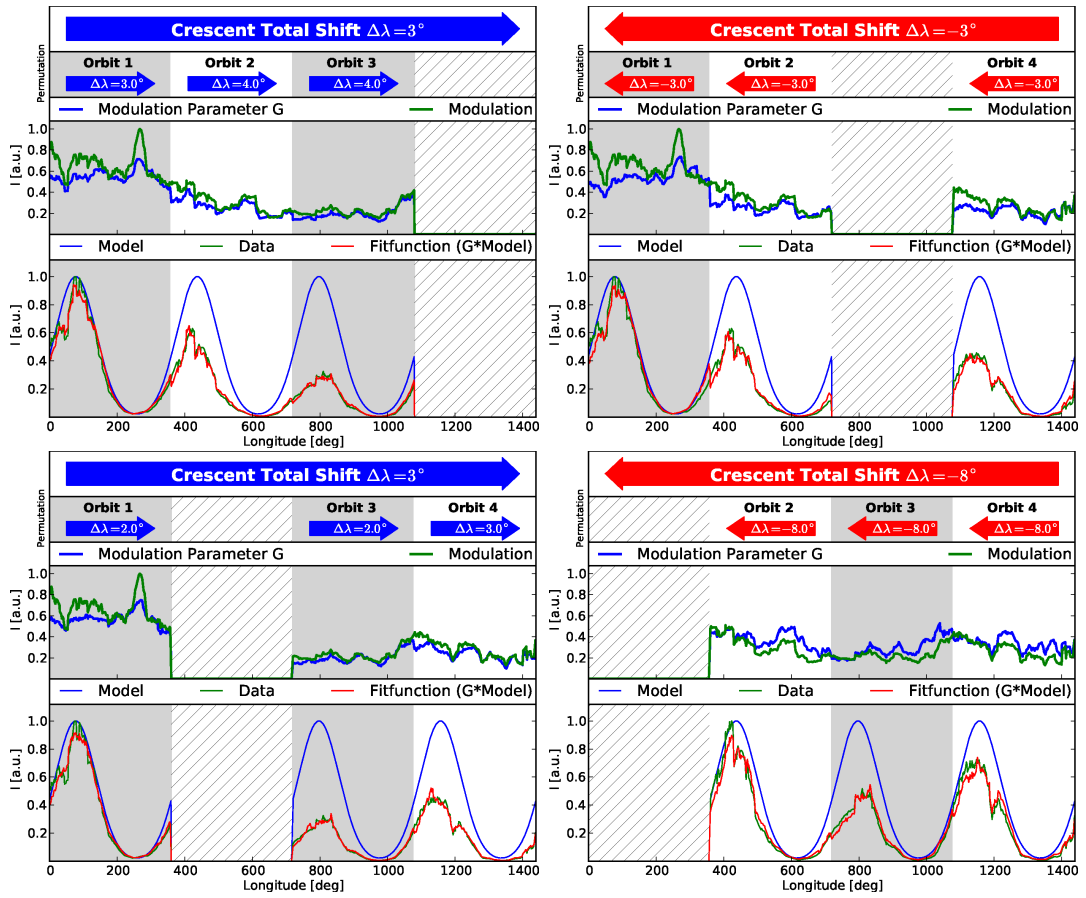


Figure A.1.: The systematic shift of the crescent location induced by the  $\text{He}^+$  efficiency decay is shown for all possible combination of 3 orbits.

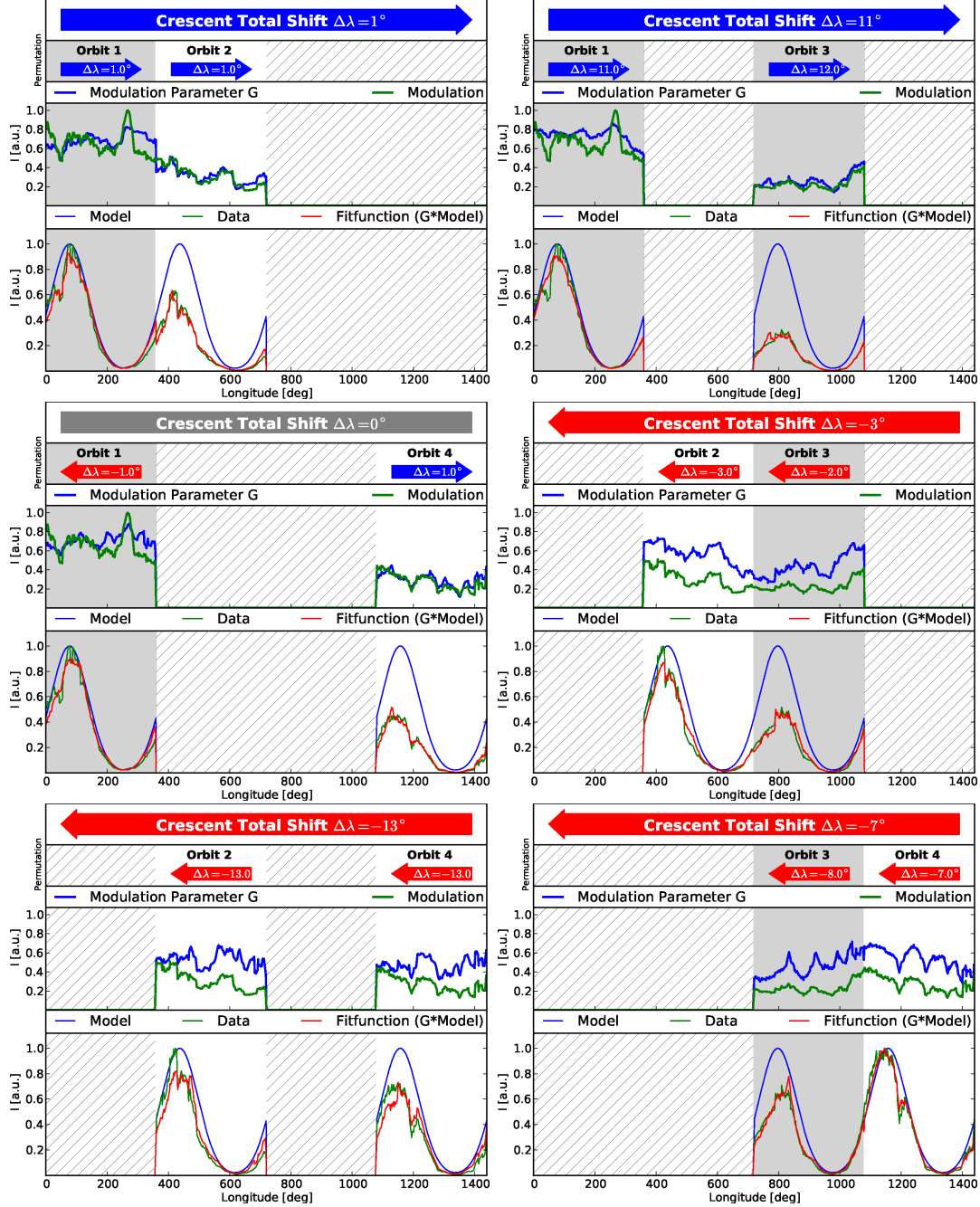


Figure A.2.: The systematic shift of the crescent location induced by the  $\text{He}^+$  efficiency decay is shown for all possible combination of 2 orbits.



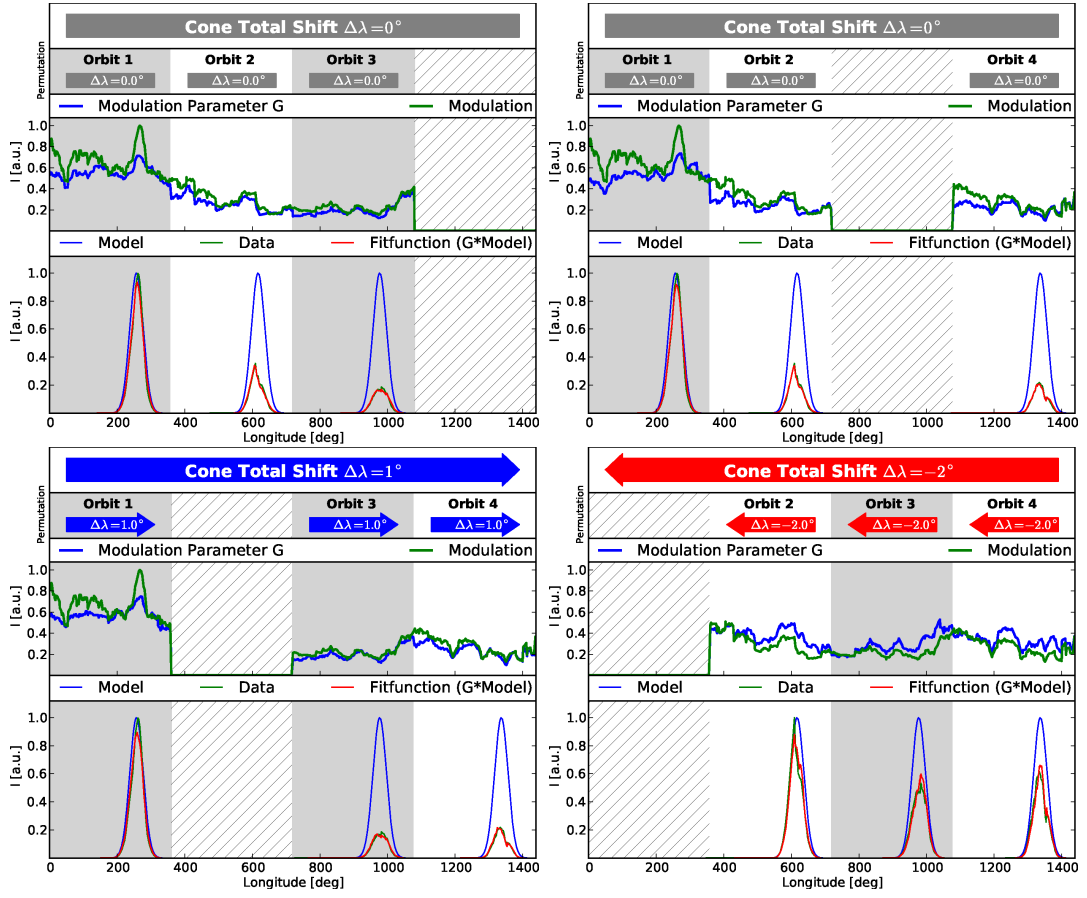


Figure A.3.: The systematic shift of the cone location induced by the  $\text{He}^+$  efficiency decay is shown for all possible combination of 3 orbits.

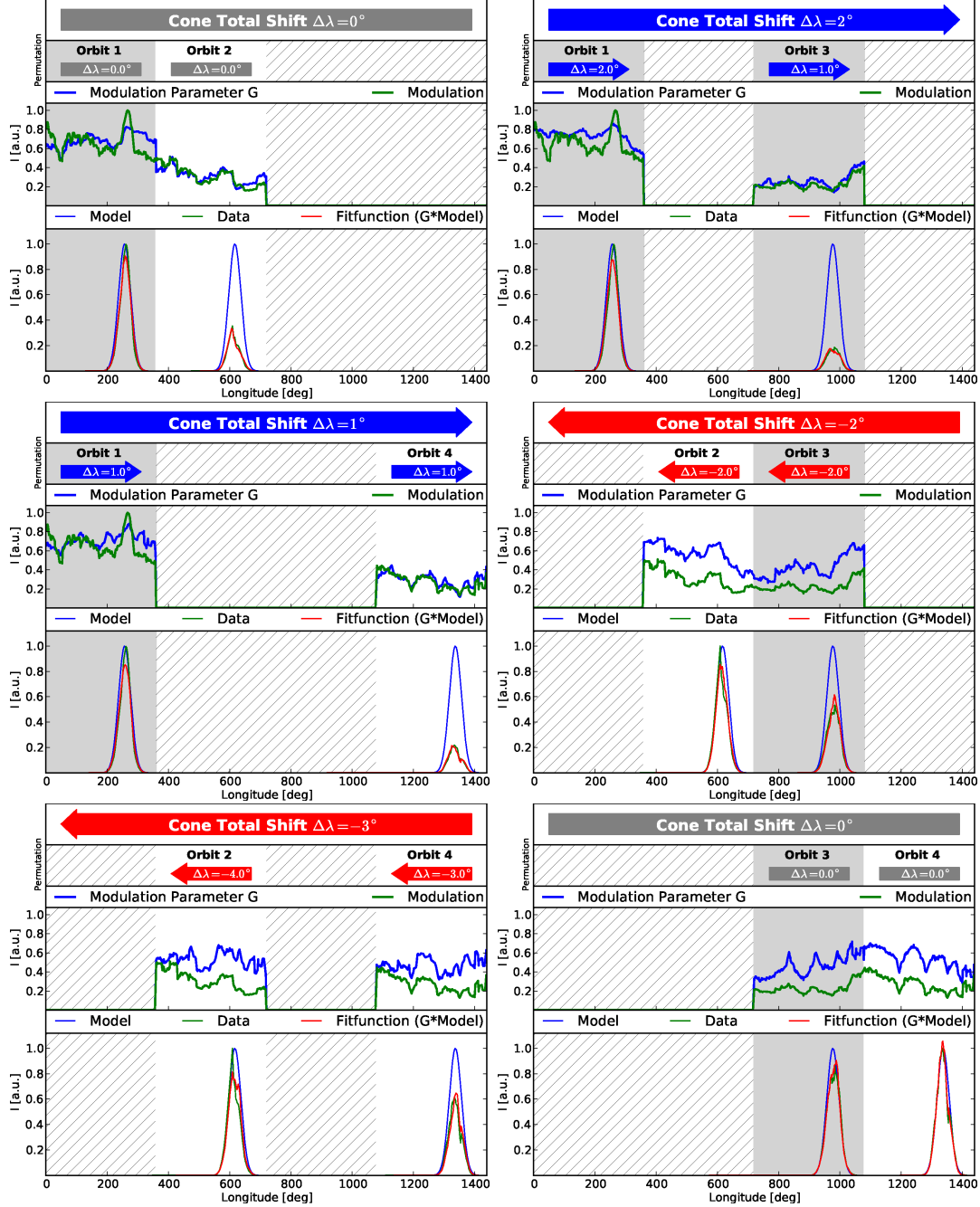


Figure A.4.: The systematic shift of the cone location induced by the  $\text{He}^+$  efficiency decay is shown for all possible combination of 2 orbits.

## Bibliography

- Allegrini, F., The PLASTIC Sensor on STEREO: Design of the Entrance System/energy Analyzer and Numerical Simulations of Solar Wind Measurements, Ph.d. thesis, Universität Bern, 2007.
- Allegrini, F., N. Schwadron, D. McComas, G. Gloeckler, and J. Geiss, Stability of the inner source pickup ions over the solar cycle, *Journal of Geophysical Research*, 110(A5), A05,105, 2005.
- Biersack, J., J. Ziegler, and M. Ziegler, *SRIM - The Stopping and Range of Ions in Matter*, James Ziegler, 2008.
- Binns, W. R., et al., GCR neon isotopic abundances: Comparison with wolf-rayet star models and meteoritic abundances, in *AIP Conference Proceedings*, vol. 598, pp. 257–262, AIP, doi:10.1063/1.1434008, 2001.
- Blush, L., et al., Development and calibration of major components for the STEREO/-PLASTIC (plasma and suprathermal ion composition) instrument, *Advances in Space Research*, 36(8), 1544–1556, doi:10.1016/j.asr.2005.07.028, 2005.
- Bochsler, P., et al., Estimation of the Neon/Oxygen Abundance Ratio At the Heliospheric Termination Shock and in the Local Interstellar Medium From Ixex Observations, *The Astrophysical Journal Supplement Series*, 198(2), 13, doi:10.1088/0067-0049/198/2/13, 2012.
- Bzowski, M., and M. Królikowska, Are the sungrazing comets the inner source of pickup ions and energetic neutral atoms?, *Astronomy & Astrophysics*, 435, 723–732, doi:10.1051/0004-6361, 2004.
- Cummings, A., and E. Stone, Composition of anomalous cosmic rays and other heliospheric ions, *The Astrophysical Journal*, 578, 194–210, 2002.
- Drews, C., Flux of Suprathermal Ions measured by Pick-Up Ions at 1 AU, Diploma thesis, Christian-Albrechts-Universität Kiel, 2009.
- Drews, C., L. Berger, R. F. Wimmer-Schweingruber, A. B. Galvin, B. Klecker, and E. Möbius, Observations of interstellar neon in the helium focusing cone, *Journal of Geophysical Research*, 115(A10), 1–9, doi:10.1029/2010JA015585, 2010.
- Drews, C., L. Berger, R. F. Wimmer-schweingruber, A. B. Galvin, B. Klecker, and M. Eberhard, Inflow Direction of Interstellar Neutrals deduced from Pickup Ion Measurements at 1 AU, *Journal of Geophysical Research*, pp. 1–38, 2012.
- Drews, C., L. Berger, R. F. Wimmer-Schweingruber, and B. Galvin, Interstellar He + Ring-Beam Distributions: Observations and Implications, *Geophysical Research Letters*, *accepted*, 2013.

- Fahr, H., On the influence of neutral interstellar matter on the upper atmosphere, *Astrophysics and Space Science*, 1968.
- Fahr, H. J., Influence of interstellar matter on the density of atmospheric hydrogen., *Annales de Géophysique*, 1969.
- Frisch, P. C., The Galactic Environment of the Sun, *American Scientist*, p. 52, 2000.
- Frisch, P. C., S. Redfield, and J. D. Slavin, The Interstellar Medium Surrounding the Sun, *Annual Review of Astronomy and Astrophysics*, 49(1), 237–279, doi:10.1146/annurev-astro-081710-102613, 2011.
- Galvin, A. B., et al., The Plasma and Suprathermal Ion Composition (PLASTIC) Investigation on the STEREO Observatories, *Space Science Reviews*, 136(1-4), 437–486, doi:10.1007/s11214-007-9296-x, 2008.
- Geiss, J., G. Gloeckler, L. A. Fisk, and R. V. Steiger, C + pickup ions in the heliosphere and their origin, *Journal of Geophysical Research*, 100(A12), 373–377, 1995.
- Geiss, J., G. Gloeckler, and R. Steiger, Origin of C+ ions in the heliosphere, *Space Science Reviews*, 78(1-2), 43–52, 1996.
- Gloeckler, G., L. Fisk, and J. Geiss, Elemental composition of the inner source pickup ions, *Journal of Geophysical Research*, 105(A4), 7459–7463, 2000.
- Gloeckler, G., E. Möbius, J. Geiss, M. Bzowski, S. Chalov, H. Fahr, D. R. McMullin, H. Noda, and M. Oka, Coordinated observation of local interstellar helium in the Heliosphere - Observations of the helium focusing cone with pickup ions, *Astronomy*, 854, 845–854, doi:10.1051/0004-6361, 2004.
- Kaiser, M., T. Kucera, and J. Davila, The STEREO mission: An Introduction, *Space Science Reviews*, 136(1-4), 5–16, 2008.
- Kallenbach, R., J. Geiss, and G. Gloeckler, Pick-up Ion Measurements in the Heliosphere A Review, *Astrophysics and Space Science*, 274, 97–114, 2000.
- Klecker, B., Pickup helium observations with STEREO PLASTIC A & B, *STEREO SWG 19 Proceeding*, pp. 1–24, 2009.
- Köten, M., An improved efficiency model for ACE/SWICS - Determination of the carbon isotopic ratio  $^{13}\text{C}/^{12}\text{C}$  in the solar wind from ACE/SWICS measurements, Ph.d. thesis, Christian-Albrechts-Universität, Kiel, 2009.
- Mann, I., and A. Czechowski, Dust Destruction and Ion Formation in the Inner Solar System, *The Astrophysical Journal*, 621(1), L73–L76, doi:10.1086/429129, 2005.
- McComas, D. J., et al., IBEX - Interstellar Boundary Explorer, *Space Science Reviews*, 146(1-4), 11–33, doi:10.1007/s11214-009-9499-4, 2009.
- Möbius, E., D. Ruscinski, M. A. Lee, and P. A. Isenberg, Decreases in the antisunward flux of interstellar pickup He+ associated with radial interplanetary magnetic field, *Journal of Geophysical Research*, 103, 257–265, 1998.

- Möbius, E., et al., Interstellar Gas Flow Parameters Derived From Interstellar Boundary Explorer-Lo Observations in 2009 and 2010: Analytical Analysis, *The Astrophysical Journal Supplement Series*, 198(2), 11, doi:10.1088/0067-0049/198/2/11, 2012.
- Prölls, G., *Physik des erdnahen Weltraums*, 2. Aufl. ed., 528 pp., Springer, 2004.
- Russell, C. T. (Ed.), *The STEREO Mission*, Springer New York, New York, NY, doi: 10.1007/978-0-387-09649-0, 2008.
- Saul, L., Observational evidence of pitch angle isotropization by IMF waves, *Geophysical Research Letters*, 31(5), L05,811, doi:10.1029/2003GL019014, 2004a.
- Saul, L., Variations of Pickup Ion Distributions and Their Relation to Interplanetary Conditions and Waves, *AIP Conference Proceedings*, 719(2004), 207–212, doi: 10.1063/1.1809519, 2004b.
- Saul, L., and P. Isenberg, On pitch-angle scattering rates of interstellar pickup ions as determined by in situ measurement of velocity distributions, *The Astrophysical Journal*, 655, 672–677, 2007.
- Schwadron, N. A. N., J. Geiss, L. A. L. Fisk, G. Gloeckler, T. H. Zurbuchen, and R. von Steiger, Inner source distributions: Theoretical interpretation, implications, and evidence for inner source protons, *Journal of Geophysical Research*, 105(A4), 7465, doi: 10.1029/1999JA000225, 2000.
- Vasyliunas, V. M., and G. L. Siscoe, On the Flux and the Energy Spectrum of Interstellar Ions in the Solar System, *Journal of Geophysical Research*, 81(7), 1247, 1976.
- von Steiger, R., T. H. Zurbuchen, and D. J. McComas, Oxygen flux in the solar wind: Ulysses observations, *Geophysical Research Letters*, 37(22), doi:10.1029/2010GL045389, 2010.
- Wimmer-Schweingruber, R., and P. Bochsler, On the origin of inner-source pickup ions, *Geophysical Research Letters*, 30(2), 2–5, doi:10.1029/2002GL015218, 2003.
- Wimmer-Schweingruber, R. F., The Composition of the Solar Wind, *Adv. Space Res.*, 30(I), 23–32, 2002.
- Wimmer-Schweingruber, R. F., and C. Drews, Pickup Ions in the Heliosphere, *Deutsche Forschungsgemeinschaft*, (unpublished), project proposal, 2012.

## Danksagung

Ich danke Prof. Dr. R.F. Wimmer-Schweingruber für die Vergabe des Themas und die sehr gute Betreuung der Dissertation.

Dr. Lars Berger danke ich für die hervorragende wissenschaftliche Betreuung, das kritische Hinterfragen vieler Forschungsergebnisse und die Zusammenarbeit bei vielen kleinen als auch grossen Projekten dieser Arbeit.

Der gesamten Arbeitsgruppe "Extraterrestrik" möchte ich danken für das entspannte Arbeitsklima und die reichlichen Diskussion im Rahmen der Dissertation. Hierbei möchte ich mich vor allem bedanken bei Dipl.-Phys. Christoph Terasa für das Korrekturlesen dieser Arbeit und die zahllosen Diskussion über Gott und die Welt, Dipl.-Phys Thies Peleikis für das Korrekturlesen der Arbeit und Eve-Talk, D(e)r. Jan Köhler für das Korrekturlesen der Arbeit und schnelle Hilfe wenn der Computer mal wieder streikt und Dr. Christian Hamann für das Korrekturlesen der Arbeit. Ich danke ausserdem der Kochgruppe "Extraterrestrik" für die geniale Alternative zur Mensa und Dipl.-Phys. Viktor Hrkac ohne den ich wohl niemals mit dem Physik Studium angefangen hätte.

Des weiteren bedanke ich mich bei der Deutschen Forschungsgemeinschaft, die einen Teil dieser Arbeit im Rahmen des Projektes Wi-2139/7-2 gefördert haben.

Für die moralische Unterstützung während der Promotion bedanke ich mich ganz herzlich bei meiner Familie, Gert, Veronika und Steffi und bei meiner Lebensgefährtin Birgit ... insbesondere dafür dass sie mich die Promotionszeit über ausgehalten haben.

## Eidesstattliche Versicherung

Hiermit versichere ich an Eides Statt, dass die vorliegende Arbeit abgesehen vom Rat meiner akademischen Lehrer ohne fremde Hilfe und lediglich unter Verwendung der angegebenen Literatur sowie den bekannten Nachschlagewerken der Naturwissenschaften angefertigt habe, und sie nach Inhalt und Form meine eigene ist. Diese Arbeit ist unter Einhaltung guter wissenschaftlicher Praxis entstanden. Ich versichere, dass diese Arbeit weder ganz noch teilweise an anderer Stelle zur Prüfung vorlag. Frühere Promotionsversuche wurden von mir nicht vorgenommen.

Desweiteren erkläre ich hiermit, dass die in Kapitel 3.2 und 4.2 vorgestellten Ergebnisse bereits im *Journal of Geophysical Research* in der hier vorgestellten Form (siehe [Drews et al., 2010] bzw. [Drews et al., 2012]) veröffentlicht wurden. Die in Kapitel 5.2 vorgestellten Ergebnisse (siehe [Drews et al., 2013]) werden vorraussichtlich in *Geophysical Research Letters* in der hier vorgestellten Form veröffentlicht werden.

Kiel, den \_\_\_\_\_